

OPTOGENETIC INTERROGATION AND MANIPULATION OF
VASCULAR BLOOD FLOW IN CORTEX

by

Farid Atry

A Dissertation Submitted in
Partial Fulfillment of the
Requirements for the Degree of

DOCTOR OF PHILOSOPHY

in

ENGINEERING

at

The University of Wisconsin–Milwaukee

December 2017

ABSTRACT

OPTOGENETIC INTERROGATION AND MANIPULATION OF VASCULAR BLOOD FLOW IN CORTEX

by

Farid Atry

The University of Wisconsin–Milwaukee, 2017
Under the Supervision of Professor Ramin Pashaie

Understanding blood flow regulatory mechanisms that correlate the regional blood flow with the level of local neuronal activity in brain is an ongoing research. Discerning different aspects of this coupling is of substantial importance in interpretation of functional imaging results, such as functional magnetic resonance imaging (fMRI), that rely on hemodynamic recordings to detect and image brain neuronal activity. Moreover, this understanding can provide insight into blood flow disorders under different pathophysiological conditions and possible treatments for such disorders.

The blood regulatory mechanisms can be studied at two different; however, complementary levels: at the cellular level or at the vascular level. To fully understand the regulatory mechanisms in brain, it is essential to discern details of the coupling mechanism in each level. While, the cellular pathways of the coupling mechanism has been studied extensively in the past few decades, our understanding of the vascular response to brain activity is fairly basic. The main objective of this dissertation is to develop proper methods and instrumentation to interrogate regional cortical vasodynamics in response to local brain stimulation.

For this purpose we offer the design of a custom-made OCT scanner and the necessary lens mechanisms to integrate the OCT system, fluorescence imaging, and optogenetic stimulation technologies in a single system. The design uses off-the-shelf components for a cost-effective

design. The modular design of the device allows scientists to modify it in accordance with their research needs. With this multi-modal system we are able to monitor blood flow, blood velocity, and lumen diameter of pial vessels, simultaneously. Additionally, the system design provides the possibility of generating arbitrary spatial stimulation light pattern on brain. These abilities enables researchers to capture more diverse datasets and, eventually, obtain a more comprehensive picture of the vasodynamics in the brain.

Along with the device we also proposed new biological experiments that are tailored to investigate the spatio-temporal properties of the vascular response to optical neurostimulation of the excitatory neurons. We demonstrate the ability of the proposed methods to investigate the effect of length and amplitude of stimulation on the temporal pattern of response in the blood flow, blood velocity, and diameter of the pial vessels. Moreover, we offer systemic approaches to investigate the spatial characteristics of the response in a vascular network. In these methods we apply arbitrary spatial patterns of optical stimulation to the cortex of transgenic mice and monitor the attributes of surrounding vessels. With this flexibility we were able to image the brain region that is influenced by a pial artery.

After characterizing the spatio-temporal properties of the vascular blood flow response to optical neuro-modulation, we demonstrate the design and application of an optogenetic-based closed-loop controller mechanism in the brain. This controller, uses a proportionalintegralderivative (PID) compensator to engineer temporal optogenetic stimulation light pulses and maintain the flow of blood at various user defined levels in a set of selected arteries. Upon tuning the gain values of the PID controller we obtained a near to critically-damped response in the blood flow of selected arterial vessels.

© Copyright by Farid Atry, 2017
All Rights Reserved

To my Wife and Daughter

TABLE OF CONTENTS

1	Overview	1
1.1	Optogenetics	1
1.2	Hemodynamic Recording	4
2	Optical Coherence Tomography	6
2.1	Introduction	6
2.2	Theory of spectral-domain OCT image formation	8
2.2.1	Axial resolution	10
2.2.2	Imaging depth	11
2.3	Design Considerations	13
2.3.1	Light source	13
2.3.2	Sample arm	14
2.3.3	Beam combination	23
2.3.4	Reference arm	24
2.3.5	Spectrometer arm	24
2.3.6	Fibers, Coupler, and Circulator	30
2.4	Functional spectral-domain OCT	31
2.4.1	Measuring Blood Velocity	31
2.4.2	Angiography	35
3	Optogenetic SD-OCT system	37
3.1	Introduction	37
3.2	Light Source	37
3.3	Sample arm	38
3.3.1	Scan-lens and tube-lens mechanisms	39
3.3.2	Beam combination	44
3.3.3	Reference arm	45
3.3.4	Spectrometer	47
3.3.5	Fiber-based components	48
3.4	Experimental Results	49
3.4.1	Sample Preparation.	51
3.4.2	Point Spread Function Measurement	51
3.4.3	Axial resolution measurements	54
3.4.4	Intensity change across the field of view	55
3.4.5	Fluorescence imaging	56
3.5	Practical considerations	58
3.6	Software	64
3.6.1	Structural SD-OCT processing	64
3.6.2	Velocimetry	67
3.6.3	Angiography	69
3.7	Conclusion	73

4	Wide field brain stimulation	79
4.1	Introduction	79
4.2	System Design	81
	4.2.1 Velocity Measurement	83
	4.2.2 Angiography	85
4.3	Experiments	86
4.4	Results	88
4.5	Conclusion	93
5	Spatio-temporal characteristics of cortical vasodynamics	95
5.1	Introduction	95
5.2	Results	97
5.3	Online Methods	105
5.4	Supplementary Materials	111
5.5	Discussion	121
6	Discussion & Future Directions	141
6.1	Introduction	141
6.2	System design	142
6.3	Analysis of results	143
6.4	Future directions	144
	Bibliography	146
	Curriculum Vitae	167

LIST OF FIGURES

2.1	A fiber-coupled spectral-domain OCT scanner. It uses a low-coherence light source to illuminate sample (path 3) and reference arms (path 1). In the sample arm a set of galvanometric mirrors raster scan a sample. Light that is collected back from reference and sample arms recombine to form interference patterns which are detected by a spectrometer (path 3).	12
3.1	The schematic of a scan-lens and a tube-lens in an OCT optical path. A galvanometric mirror is located at the focal of the scan-lens and the scan/tube lens mechanism projects the OCT beam on the back-focal-plane of the objective lens. A dichroic mirror is added to separate the OCT beam and an auxiliary beam. An auxiliary light beam can be used for other imaging modalities or optogenetic stimulation applications. f_S , f_T , and f_O are respectively the focal lengths of the scan-lens, tube-lens and objective.	40
3.2	Optical aberrations when two CaF2 lenses (LB5284, Thorlabs, NJ, USA) are used as scan and tube lenses in combination with an 18mm focal length objective lens. (A) Field curvature and astigmatic aberrations. (B) Ray aberration as a function of pupil coordinate.(C) Chromatic focal shift. (D) Wavefront RMS vs scan angle.	41
3.3	Optical aberrations when two achromatic doublet lenses (AC254-050-C, Thorlabs, NJ, USA) are used as scan and tube lenses in combination with a paraxial objective with an 18mm focal length objective lens. (A) Field curvature and astigmatic aberrations. (B) Ray aberration as a function of pupil coordinate.(C) Chromatic focal shift. (D) Wavefront RMS vs scan angle.	42
3.4	The schematic of the lens mechanism based on four element scan/tube lens. The effective focal length of the lens compound is $\sim 66mm$	43
3.5	Optical aberrations when two semi Plössl compound lenses (AC254-125-C+AC254-150-C, Thorlabs, NJ, USA) are used as scan and tube lenses in combination with an 18mm focal length objective lens. (A) Field curvature and astigmatic aberrations. (B) Ray aberration as a function of pupil coordinate.(C) Chromatic focal shift. (D) Wavefront RMS vs scan angle.	44
3.6	Sample arm. This image demonstrates the design of the sample arm that is mounted on a typical microscope stand. This system uses two identical semi Plössl lenses as scan and tube lenses. The cross section shows the optics including galvanometric mirrors, scan and tube lens mechanisms and the infrared dichroic mirror. 1-OCT collimator, 2-custom mounts, 3-commercial microscope stand, 4-scan head, 5-OCT beam, 6-scan lens, 7-lens tube, 8-tube lens, 9-dichroic mirror, 10-visible port, 11-objective lens, 12-galvanometric mirrors.	45

3.7	Fluorescence imaging path. a) the schematic and b) the solid work design of the fluorescence imaging path. The fluorescence imaging path uses two semi Plössl lenses to image the back focal plane of the objective to the entrance pupil of an imaging lens. There is an adjustable iris in this path to adjust the aperture diameter of the imaging system. This is helpful to reduce the aberration in the optical path and improve the imaging resolution. 1-Fluorescence camera (Exi Aqua, Qimaging, BC, Canada), 2-adjustable iris (SM1D12CZ, Thorlabs, NJ, USA), 3-imaging lens (AC254-040-A, Thorlabs, NJ, USA), 4-semi Plössl lens (AC254-100-A + AC254-250-A), 5-Visible light dichroic mirror (FF440-520-Di01, Semrock Inc., NY, USA), 6-semi Plössl lens (AC254-075-A + AC254-200-A), 7-Long-pass infrared dichroic (FF875-Di01, Semrock Inc., NY, USA)	46
3.8	Multi-modal scanner setup. The system incorporates the visible and OCT imaging mechanisms to allow for OCT data acquisition simultaneous with optogenetic stimulation or fluorescence imaging. Port 1 is the stimulation/excitation beam path.	47
3.9	(a) The solidwork design of the reference arm. 1- fiber connector, 2-scan lens, 3-tube lens, 4-dispersion compensator for the objective. 5- a gold mirror installed on a kinematic mount with adjustable angles. 6-translational stage to precisely control the position of the reference mirror. (b) The solidwork design of spectrometer arm. The grating has an optimal incident angle of 48.6° , diffracted angle of 48.6° . It is mounted on rotatory mounts to adjust the angles of the grating with respect to the OCT beam and the lens mechanism. 1-fiber connection, 2-Grating installed on rotatory mounts. 3-Plössl lens, 4-line CCD camera. (c) the reference and spectrometer arms are installed on an optical bread board to facilitate transportation. There is a movable mirror mount (1) in the reference arm that can change the beam path to match different objective lenses in the sample arm. The reference and spectrometer arms are encircled with the orange and green outlines, respectively.	49
3.10	A schematic of the spectrometer. The grating diffracts the broadband collimated beam. The lens system acts as a scan lens and focuses the diffracted light beams on the focal plane array of a line scan camera. The focal length of the lens mechanism is designed such that the desired spectrum ($1200nm$ to $1400nm$) is covering the extent of the detector array. Optical aberrations in this scan lens system is low which reduces the sensitivity roll-off of the OCT images.	50
3.11	A typical lateral PSF measured for semi Plössl relay lens system. A 2D Gaussian function is fitted to the PSF to measure the FWHM along the fast and slow scan mirror axes. Cross-sectional profile of the PSF and the fitted Gaussian function are plotted for each of the fast and slow axis directions.	53

3.12	FWHM of the PSF of the OCT system in the transversal plane at different positions along the fast mirror axis (A) and the slow mirror axis (B). FWHM of the lateral PSF of the OCT system with the semi Plössl lens mechanism remains below $8\mu m$ for positions up to $2mm$ away from the center of field of view. For the single achromatic doublet lens at the $1mm$ distance from the optical axis FWHM exceeds $8\mu m$	54
3.13	Top: A 2D cross-sectional image taken when two achromatic doublets were used as the scan-lens and tube-lens. To be able to see out of focus particles a logarithmic scaling is used which compresses the dynamic range of the image intensity. The out of focus nano-shell gold particles have much smaller intensity and the corresponding PSF is spread over a larger area compared to the particles in the focal of the objective lens. The field curvature is considerable and at the sides of the image the focal approaches toward the surface. Typical lateral PSF measurements at $1mm$ from the center of FOV are shown at the lower panel. Due to astigmatism PSF's are not similar above and below the focal surface. The arrows are just for illustrative purposes and are not showing the exact location of PSF measurements since they were obtained from a different recording.	55
3.14	the lateral point spread function of the proposed OCT system at different depths. These measurements are conducted when the focal plane of the OCT was placed $350\mu m$ below the surface of a 3D phantom with embedded gold nanoshells. At regions above the focal plane we observed a ring ring surrounding the central spot in the lateral PSF.	56
3.15	Axial resolution of the implemented SD-OCT system.	57
3.16	Variation in the OCT images across the field of view. The maximum diffraction limited field of view for this objective is $\sim 4.7mm$ in diameter. When we approach this limit the intensity drops.	58
3.17	A sample fluorescence image captured by the device. The animal was a Thy1::ChR2/H134R-YFP mouse with yellow fluorescence protein expressed in excitatory neurons. The image shows the morphology of the vessels under a thin layer of skull (thickness of $\sim 100\mu m$).	59
3.18	A sample result of calcium imaging. Stimulation pulses at $50\mu A$, $100\mu A$, and $150\mu A$ were delivered to the brain of a GCaMP6f mouse. The stimulation duration was $600ms$ with a pulse frequency of $150Hz$. a) The change in the fluorescence intensity is color coded and superimposed on the original images. The stimulation location is shown by an asterisk. b) the intensity line profile across the line marked in panel (a). The line profile is obtained by averaging 3 frames starting at time $t = 200ms$. c) the intensity temporal profile at the site of stimulation. The error bars show the standard deviation across at least 5 recordings at each current level.	60
3.19	Fixed pattern noise (FPN) and fixed background cover the cross-sectional OCT image of an orange pulp. Using background removal we can improve quality of OCT images.	66

3.20	Comparison between the velocity profiles obtained by the proposed method and phase-resolved method. There are some vessels in the top image that can not be detected with the phase-resolved method.	75
3.21	Cross-sectional structural and angiographic images of a mouse brain.	76
3.22	A cross-sectional angiogram of a mouse cortex before (left) and after (right) deshadowing. Deshadowing can remove the shadows created by large vessels while keeping most of the capillaries intact. The contrast of the angiogram also has significantly improved after applying the deshadowing.	77
3.23	Examples of maximum intensity projection of the OCT angiography data for human finger nail bed (a) and rat brain (b) after local contrast enhancement.	77
3.24	A example of contrast enhancement on MIP OCT angiograms. (a) the MIP image in a mouse brain prior to histogram equalization. (b) the same MIP in (a) after applying histogram equalization. There are dark areas in the images which are produced by platinum ECoG devices. The platinum ECoG that was placed on the brain surface in this animal blocked the OCT beam and created dark regions in the images.	78
4.1	Schematic of the SD-OCT system used in the optogenetic stimulation study. The beams of a broadband infrared superluminescence diode (SLD) and a red aiming laser are coupled in the sample and reference arms using a variable fiber coupler. The red laser beam is employed for visual targeting only and is not used for the imaging purposes. Using the variable coupler, we adjust the percentage of the optical power which is coupled in each arm of the interferometer. For optical stimulation of the brain tissue, a cold mirror is integrated in the sample arm which reflects the beam of a blue laser toward the objective lens. The blue laser is controlled by a computer and generates $15Hz$ light pulses when the laser is activated.	82
4.2	Dilation of cerebral vessels during optogenetic stimulation in a ChR2 mouse. (A) the bright field image taken with a CCD camera of a ChR2 mouse. (B) Maximum intensity projection of 3D angiogram of (A). A1 shows the MCA and A2 is one of its branches. The red color specifies the difference between the angiogram taken before and the angiogram recorded during the optogenetic stimulation. The intensity of the red color is proportional to the percent change in pixel intensity from before to during stimulation. (C) and (D) provide a closer view of the angiograms before and during the stimulation, respectively. The images show noticeable increase in the vessel diameter.	84
4.3	Fluctuation in the blood velocity and blood flow in a ChR2 mouse in response to optical neuro stimulation. (A) blood flow and velocity change in A1 and A2 in response to optical stimulation. The vertical lines specify the beginning and end of stimulation period. Blood velocity and flow are normalized to the baseline value (average of the corresponding data during the first 4 seconds of recording). (B) an example of flow and velocity response for control animal.	85

4.4	Hemodynamic response of transgenic mice compared with the control animals. (A) shows the velocity profile for A1 and A2, before (left), during (middle) and 22 second after (right) stimulation. To remove fluctuations the profiles were averaged over four seconds for each of the profiles. (B) shows fractional change in flow and velocity for control and ChR2 mice after 10 second of stimulation. (C) Quantitative comparison of fractional change in the vessel diameter after stimulation for three control and two ChR2 mice.	88
5.1	Simultaneous optogenetic stimulation and optical coherence angiography and velocimetry: (a) Schematic of the optical setup which integrates spectral-domain OCT, fluorescence imaging, and optogenetic stimulation. L: lens, ML: movable lens, SL: scan lens, TL: tube lens, OL: objective lens, FP: focal plane, GM: galvanometric mirror, FC: fiber coupler, SLD: superluminescent diodes, D: dichroic mirror, CCD: charge-coupled device, RM: reference mirror. (b) A typical fluorescence image captured from the cortical tissue of a Thy1-YFP+ transgenic mouse. (c) The maximum intensity projection of a 3D OCT angiogram obtained from a region of interest marked in the fluorescent image of panel (b). OCT angiograms are used to measure vessel diameters. (d) The maximum intensity projection of 3D Doppler-OCT measurement. (e) Snapshots of the Doppler velocity profile of a sample artery captured within a single heart cycle. By locating a bounding box which encapsulates the vessel cross-section and adding the value of all pixels inside the set, we obtain an axial blood flow index for the vessel at each time slot. (f) Examples of vessel diameter (top), blood velocity (middle), and blood flow (bottom) measurements from a typical cortical artery performed via OCT imaging. Diameter measurement time-traces are noisy since the lateral resolution of OCT angiography ($\sim 5\mu m$) is comparable to the percentage of the observed changes in vessel diameters. Heart pulsation directly affects all OCT angiography and Doppler measurements. The heart pulsation contamination was eliminated by the use of a moving average (MA) filter (black curve) or an extended Kalman filter (red curve).	97

- 5.2 Stimulation configurations: (a) The light distribution profile ($\lambda = 450nm$, $I = 5.7mW$) estimated by using Monte Carlo simulations for three different beam diameters of $266\mu m$, $461\mu m$, and $800\mu m$. The colorcode represents the photon density and the dark line represents the isoline at $1mW/mm^2$. (b) Effect of light intensity on the volume of activation (VoA). (c) Effect of the beam diameter on the VoA. (d) The fluorescent image captured from the cortical tissue showing the vasculature network. Areas of stimulation with different spot sizes are marked by different colors. (e) Effect of stimulation intensity on the blood flow response (BFR), for illumination diameters of $266\mu m$, $461\mu m$, and $800\mu m$ (from top to bottom, respectively). The gray line indicates the duration of stimulation (4 seconds). (f) The relationship between the stimulation light intensity and the average percentile change in the blood flow from stimulation onset to 20sec afterward ($n = 1$ vessel). (g) The relationship between the simulated VoA and the in-vivo BFR measurements ($n = 1$ vessel). (h) The fusion of fluorescent image and the OCT angiogram shows the vasculature network. The blue circle marks the area under illumination ($I = 5.7mW$, duration varied from 1sec to 12sec). The arrows indicate the vessel cross-sections to be monitored by the OCT. (i) The blood flow (top) and blood velocity (bottom) responses in the target vessels. Blood flow at the measurement sites 1 and 2 increases after the stimulation onset, but not at site 3. Longer stimulus duration causes stronger and lasting responses at sites 1 and 2. (j) The normalized BFR at site 2. Longer stimulations translate to enduring responses which take more time before returning to the baseline. The dashed line marks 20% threshold. (k) BFR duration as a function of the stimulation duration ($n = 1$ vessel). 126
- 5.3 Vascular receptive fields. (a) The vascular network in the animal under test (top) and the 25 stimulation locations (bottom) in a form of a 5 by 5 matrix. Diameters of the circles are $461\mu m$ to represent the actual beam diameter on the tissue surface. The red lines mark the vessel cross-sections that are being imaged as monitoring sites. (b) The color coded receptive field (RF) of the arterial blood flow for the 4 selected vessel cross-sections. The dark red color shows strong increase, green color represents zero response, and blue color represents decrease in the blood flow in each vessel. The RF for the vessel 2 was $734\mu m$ long and $539\mu m$ wide. (c) The RFs for blood flow, blood velocity, and vessel diameter measured at $t = 5$ seconds. The curves show the time traces of blood flow, blood velocity, and vessel diameter percentile change for all the selected vessels when the stimulation was located on vessel 2 (marked by an asterisk). No significant blood flow increase in vessel 1 was observed; however, simultaneous dilation of the vessel caused some drop in its blood velocity. 127

- 5.4 Simultaneous multi-site stimulation. Stimulation sites in each panel are marked by blue circles. (a) Fusion of the fluorescence and angiographic images of the vascular network in the animal under test. The vessels of interest (a parent and its daughter branches) are highlighted by the red color. In this experiment, the stimulation is applied only to site 1. (b) Time traces of blood flow in the selected vessels. BFRs in all three vessels were responsive at different levels to photostimulation of site 1. The gray line shows the period that the stimulation was applied. Each recording was repeated at least four times and the results were averaged. The solid line is the average across trials and the shaded area represents the standard deviation. (c) In this experiment, the stimulation was delivered only to site 2. (d) Time traces of blood flow in selected vessels following the stimulation of site 2. BFRs in all three vessels were responsive at different levels to photostimulation of site 2. (e) We simultaneously stimulated sites 1 and 2 at half of the power used in last two experiments of panels (a) and (c). (f) The time traces of blood flow in all selected vessels for simultaneous stimulation test. (g) A summary of the amount of BFR (blood flow averaged over 60 seconds) under different stimulation scenarios ($n = 3$ vessels). The error bars represent the standard deviation across trials. 128
- 5.5 Optogenetic-based closed-loop control of blood flow. (a) Block-diagram of the closed-loop controller. The system uses OCT to measure the difference between the user defined target for blood flow and the actual value measured in the vessel(s) of interest. The difference is fed to a PID compensator to adjust the pulse width of photostimulation. (b) Smoothed blood flow (top) and optogenetic pulse width (bottom) during a control epoch (330sec). Data collection contains 30sec of baseline recording followed by 240sec of control period and 60sec (or 90sec) of post stimulation recording. The target blood flow level is shown by a red solid line in the top plot. (c) Vascular network in the animal under test. The area of illumination is marked by the blue circle. The arrow points to the vessel cross section under study. (d) Maintaining blood flow at different set points. Each experiment was repeated three times when the variables of the PID controller were adjusted at $KP = 3.1$, $KD = 25$, and $KI = 1.5 \times 10^{-3}$. The first row shows the traces of BFR for three experiments each targeting a different set point on same artery. The solid line represents the average of trials. The inset magnifies 30sec duration of each test to substantiate the correlation between the flow (gray line) and the stimulation pulse width (blue line) for a typical trial. The second row displays the time trace of the pulse width in each test. The last row shows the distribution of blood flow during the last 120sec of control session. The center mark is the median, the whiskers are the maximum and minimum, and the box edges are the 25th and 75th percentiles of the data. 129

- S1 The effect of wide-field photostimulation on cortical vasculature. (a) OCT generated angiogram demonstrates a wide spread vessel dilation in response to optogenetic stimulation. The induced change in each vessel diameter is marked by the surrounding red color around that vessel. (b) Discrete angiograms of a few selected vessels before and after stimulation highlight observed changes. (c) Maximum intensity projection (MIP) of 3D Doppler OCT measurements before stimulation. (d) MIP of 3D Doppler OCT measurements after stimulation. (e) Percentile change in blood flow in response to 10sec of stimulation in vessels marked in panel (a). Each graph was obtained by averaging at least eight trials. The shaded areas show standard deviations. (f) Percentile change in blood velocity for vessels shown in panel (e). (g) Change in the velocity profile in response to optogenetic stimulation. Top: the maximum velocity projection of the vessel profile over time. The horizontal axis represents time while the vertical axis is the lateral position across the vessel. The pixel intensity is the maximum velocity along the depth in that location. The solid black line shows the duration of stimulation. Middle: three cross-sectional velocity profiles of the vessels 4sec before, 6sec after, and 36sec after the stimulus onset. Each curve is obtained by averaging the measured Doppler profiles for 4sec. Bottom: the maximum value projection curves of three cross-sections. Results show the velocity increase at the center of vessels as well as the change in velocity profiles. (h) Summary of the percentile changes in blood flow, blood velocity, and vessel diameter for five transgenic and three wild-type animals in response to optical neurostimulation. 130
- S2 Velocity, diameter, and flow receptive fields. (a) velocity receptive fields of four vessels under study. The response in blood velocity is stronger when we stimulate the area closer to the territory of a vessel. The maximum velocity increase (31%) was observed was in vessel 4. (b) Diameter receptive fields. Unlike blood velocity, we observed that the map of vessel dilation does not necessarily collocate with the territory of the vessels. Basically, we observed that the maximum dilation for vessel 1 and 4 happens when we stimulate the territory of vessel 2. Stimulating the territory of these vessels did not evoke a noticeable dilation. This can be justified by the endothelial signaling hypothesis (144). (Since the lateral resolution of our OCT is $\sim 5\mu m$, accurate measurements of sub-micron changes in vessel diameters was quite challenging.) (c) Flow receptive fields. Vessel 2 shows the largest flow response (54% increase). Similar to velocity receptive fields The maximum response happens when the light illumination is on the vessel and the response drops quickly as we move away from the vessel. Despite this similarity, we observed some differences between the two receptive fields. For example, in vessel 1 and 2, we see that the shape of the receptive fields are different for blood flow and velocity. Another example, is the vessel 4. This vessel shows the largest increase in its blood velocity, while the largest increase in the blood flow is observed in vessel 2. The difference between the receptive fields of blood flow and velocity is potentially due to the dilation in these vessels. (d) Estimated flow receptive fields when we combined the diameter and the velocity fields to estimate the flow response. The estimated flow was calculated by $(\hat{F}_{RF} = (1 + D_{RF})^2(1 + V_{RF}) - 1$, where V_{RF} and D_{RF} are the velocity and diameter receptive fields, and \hat{F}_{RF} is the estimated flow receptive field. The estimated flow receptive field matches the flow measurements in panel (c). 131

- S3 Tuning the PID gain values when the target value set at 15%. $KP = 3.1$ resulted in fast response and low oscillations in the blood flow. Larger values of KP led to large flow overshoots. Flow fluctuations decreased at $KD = 25$ and increased when KD was set to 50. The steady state error was significantly reduced for $KI = 1.5 \times 10^{-3}$. At $KI = 7.5 \times 10^{-3}$, the steady state error reduced further and no large fluctuation in the blood flow was observed. Larger KI values (35×10^{-3}) caused some oscillations in blood flow. The last column in this panel shows the distribution of the blood flow during the last 2 minutes of each control session. Longer whiskers oscillations correspond to stronger fluctuations in the blood flow. 132
- S4 Blood flow and its spectrum. (top) A typical blood flow trace measured by the OCT scanner. The inset shows a magnified portion of the signal in which the heart pulsation and its harmonics are visible. (bottom) Spectrum of the blood flow signal. The red circles represent the main frequency and the first 4 harmonics of the signal. The frequency components beyond the 5th harmonic are weak and can be ignored. 133
- S5 Light distribution in tissue. (a) Estimation of light distribution in tissue by the use of Monte Carlo simulations. We assumed uniform illumination on spot sizes of diameters $266\mu m$, $461\mu m$, and $800\mu m$ on the tissue surface. Results show noticeable differences between light distributions associated with different spot sizes. Changing the size of illumination spot from $266\mu m$ to $800\mu m$ (almost 3 times increase in diameter) does not cause a considerable change in the lateral extent of the volume of Activation (VoA). Therefore, using a small spot does not lead to localization of stimulation. However, using a small spot has the advantage of slightly deepening the volume of stimulation. (b) Effect of light power on the VoA. We estimated the VoA by measuring the tissue volume that is receiving irradiance of $1mW/mm^2$ or larger. Different spot sizes are represented by different colors. We observed linear relationship between the VoA and the light intensity. Under the assumptions of uniform distribution of ChR2 channels and constant density of neurons in the volume of stimulation in the cortex, this result suggests that the evoked blood flow response is mostly depends on the light intensity. (c) Effect of the beam diameter on VoA. We see a negligibly small difference between the volumes of stimulation under different illumination sizes when light intensity is kept constant. (d) Effect of irradiance on VoA. This curve shows the VoA with respect to the beam diameter when the irradiance was set to $\approx 12mW/mm^2$. We observe a non-linear relationship between the increase in the beam diameter and VoA. (e) Isolines of irradiance $1mW/mm^2$ for different illumination intensities when the illumination diameter is set to $266\mu m$. The axial and lateral extent of VoA grows as intensity increases. (f) Isolines of irradiance $1mW/mm^2$ for different illumination spot sizes at illumination power $5.7mW$. The isolines show that the smaller spot size can result in slightly deeper stimulation profile compared to large spot sizes at the expense of large irradiance on the surface. (g) Isolines of irradiance $1mW/mm^2$ when the irradiance was fixed at $\approx 12mW/mm^2$. When the irradiance is constant, at a safe level to avoid causing any damage to the tissue, a large spot size results in deeper stimulation profile. 134

S6	<p>(a) A fluorescence image captured with the optical setup shows the spread of the vasculature network. The area of photostimulation using different spot sizes ($266\mu m$, $461\mu m$, and $800\mu m$) is demonstrated by different colors. The center of stimulation was located about $0.5mm$ away from the target arteriole. (b) The effect of stimulation intensity on the blood flow response for the illumination diameters: $266\mu m$ (top), $461\mu m$ (middle), and $800\mu m$ (bottom). For all spot sizes, increasing the power of photostimulation led to increase in the amplitude of the blood flow response. (c) Effect of the area of illumination on the blood flow response. Each subfigure shows traces of blood flow response to stimulation of different spot sizes ($266\mu m$, $461\mu m$, and $800\mu m$ in diameter). For each subfigure, the stimulation power was kept constant. The subfigures from top to bottom show the response traces for the illumination power of $0.67mW$, $2mW$, $4mW$, and $5.7mW$, respectively. We observed no noticeable differences between the shape and the maximum amplitude of the BFR with the exception for the $4mw$ power and $461\mu m$ spot size. (d) Effect of stimulation intensity on blood velocity response. In general, increasing the intensity leads to some increase in the amplitude of the blood velocity response. However, this is not the case in all traces. For example, for the illumination diameter $800\mu m$, we see that increasing the power from $4mW$ to $5.7mW$ resulted in some decrease in the amplitude of the evoked blood velocity. When comparing the velocity response to the corresponding flow response, we notice that the blood flow and blood velocity do not follow the same pattern. For $5.7mW$ power, the amplitude of evoked blood flow response is noticeably larger than the one in $4mW$, suggesting that the vessel dilation causes the difference between flow and velocity responses. (e) Effect of the size of the illumination area on blood velocity. We observed no consistent difference between the shape and maximum amplitude of the blood velocity responses as we changed the spot size. (f) Relationship between the intensity of stimulation and the evoked response. We can see the amount of blood flow response as a function of the incident power. Results for different illumination sizes are shown with different colors. We observe a quasi-linear relationship between the illumination power and the evoked response. The amount of response here is calculated by averaging the percentile change in the blood flow from the stimulation onset to 10 seconds afterward. (g) The relationship between the beam diameter and the evoked response at constant illumination intensity. We can see the amount of evoked response remains almost constant as we change the spot size. This suggests that the area of illumination is not the determining factor in flow response as long as the power is kept constant. The quasi-linear relation between the stimulation power and hemodynamics response is comparable to the observations of (149) in macaques, and (150) in rats.</p>	135
S7	<p>Time-lapse images of the receptive fields. (a) Time-lapse images of flow receptive fields demonstrate the bi-phasic flow response. The fast and slow peaks occur at $t \sim 5s$ and $t \sim 18s$. Stimulation at the top-right portion of field of view (FOV) results some reduction in the blood flow of vessel 1 around $t \sim 5s$ which gradually returns to the baseline at $t > 15s$. (b) Time-lapse images of velocity receptive fields. A noticeable reduction in the velocity of vessel 1 occurs in synchrony with the drop in its blood flow when stimulating the top-right region of the FOV. (c) Time-lapse images of diameter receptive fields shows dilation in vessels 1 and 2 that are linked both in time and space.</p>	136

S8	Flow may drop without noticeable change in the vessel diameter. (a) Flow, velocity and diameter receptive fields at $t = 5$ seconds. (b) Flow, velocity, and diameter time traces for vessels 1 to 4 (left to right) when stimulating the location marked by the asterisk in panel (a). Optical coherence angiography detected no reduction in the diameter of vessel 1 but there was some drop ($\sim 10\%$) in its flow and velocity.	137
S9	Superposition of receptive fields of daughter vessels 1 and 2 provide an estimate of the receptive field of their parent vessel (vessel 3). The mean square error between the measured and the estimated receptive fields for the parent vessel was 2.7%.	138
S10	By fitting a Gaussian curve to the receptive field of vessel 2, we estimated the lateral extend of the receptive field to measure the standard deviation of $\sigma_x = 538\mu m$	139
S11	Comparison between the Kalman and moving average pulsation removal filters used in the closed-loop brain control tests. (a) Maintaining blood flow at three different levels when removing pulsations of cardiac cycle by a Kalman filter. Each experiment was repeated three times to ensure repeatability. (b) The box plot of the percentile blood flow change for the last two minutes of each control trial. The center line shows the median, the whiskers are the maximum and minimum, and the box edges are the 25th and 75th percentiles of the data. (c) The same figures as (a) but for the case when we used length-locked moving average algorithm to remove the heart pulsation. (d) The box plots of the data for the last two minutes of control sessions.	140

LIST OF TABLES

4.1	Fractional changes of hemodynamic signals in control and transgenic animals, (Wilcoxon test double sided p-values: $p_{\Delta F}, p_{\Delta V}, p_{\Delta D} < 0.036$).	92
S1	Initial values and variances of the Kalman filter variables. Values for B , Ω_c , Ω_r , A_c , and A_r are obtained by analyzing the baseline period as explained in the text.	118

ACKNOWLEDGEMENTS

I would like to thank my mentor and research advisor, Prof. Ramin Pashaie. Your creativity, dedication, and optimism was always a key factor in finding solutions for research challenges that I faced during my PhD studies. I enjoyed the working dynamics in your lab where you were always welcoming discussions in all stages of my research. Thank you for giving me the opportunity to be among those people that work for you.

Rex, Seth, Alana, and Israel your support during my PhD studies was influential in every single page of my dissertation. Seth and Alana you made the first platform of our imaging setup possible. Rex, you were the one that worked with me side-by-side to move the project to this point. Without your contributions this dissertation would have been much shorter. Thank you for your great ideas and amazing software and hardware that was always beyond expectations. I want to thank you, Mehdi for your support and your willing to help from the very first day of my PhD studies.

I would like to express my sincere gratitude to my thesis committee members: Professor Armstrong, Professor DeYoe, Professor Helmstetter, and Professor Law for their insightful and important comments.

I am very grateful to my family who encouraged me to continue my studies and made everything possible for me. You were my first teachers and my first mentors.

Dr. Williams, thank you for the opportunity to work with you and your dedicated and hardworking lab members. Sarah, Jane, Aaron, Jared, and Joey without you it was not possible to move forward in this path. Your help had no limits. I am always thankful for that. Thom, I was lucky to work with you for a few months before you move to Washington. It was a short period of collaboration between us but I forever appreciate your insightful discussions and your help with this project even to the very last minutes that you were in Madison.

Nothing could replace constant support of my best friend and my wife Reyhane. You were always next to me during my graduate studies. I find my self extremely lucky to share so many things with you and to have your amazing and unconditional support. Without you many things would have not been possible for me. Thank you for everything!

Chapter 1

Overview

1.1 Optogenetics

Optogenetics (1) provides a new mechanics for direct neuro-modulation. In this method with the help of molecular genetics technology, specific cell-types of interest targeted to express light-gated ion channels or light-sensitive ion pumps. After expression of these light-sensitive proteins the cell activity can be manipulated by exposure to the proper wavelength of light. Two of main microbial light-sensitive proteins *Chlamydomonas reinhardtii* Channelrhodopsin-2 (ChR2) (2) and *Natronomonas pharaonis* halorhodopsin (NpHR) (3) are able to provide high sensitivity and fast temporal response to light (4) and are used to study the brain circuits (5) and (6). ChR2 is a cation channel and allows Na^+ ions into the cell when exposed to blue light (maximum sensitivity at $\sim 450nm$) and therefore increases the activity of the targeted cell. On the other hand NpHR is a chloride anion pump and increases the population of Cl^- ions inside the cell (which suppresses the cell activity) when exposed to yellow light (maximum sensitivity at $\sim 580nm$) (7).

The optical neurostimulation has several advantages over the traditional electrical stimulation methods:

- Cell-type specificity: Genetic technology allows to express light-sensitive opsins in specific cell-types therefore light can produce stimulation in those cell-types without directly affecting other cells-types. In electrical stimulation all cell populations within the extent of stimulation are affected.
- Bidirectional control of the neural activity: NpHR provides the tool to directly re-

duce the neural activity using yellow light. In the electrode-based stimulation, it is not feasible to directly inhibit neural activity. Indirect inhibition with the electrical stimulation is usually performed by stimulating the regulatory/inhibitory neurons.

- Less invasive: In electrode-based stimulations, it is recommended that electrodes to touch the surface of the brain or even be implanted inside the brain which makes it difficult for chronic studies. Using optogenetics, it is possible to deliver light even through a thin layer of bone, and as a result performing long-term studies would be easier since the method can be less invasive.

The benefits of optical neurostimulation over the traditional electrical stimulation methods have made this method quite versatile. In 2009, Ayling *et al.* (8) have used optogenetic stimulation to map the motor cortex of ChR2 positive mouse and compared their results with the electrical stimulation. In their experiments, they have observed that both stimulations (electrical and optical) produced similar results and the latency between the stimulation and muscle excitation (10-20ms) was almost the same in both experiments. Optogenetics has also been used to study the brain hemodynamics and to understanding blood oxygenation level-dependent (BOLD) signal in functional MRI (fMRI) (9), (10), (11), (12). In (10) the temporal linearity of the BOLD signal has been studied in mice by employing optogenetic stimulation. They also recorded evoked spikes in local field potential (LFP) induced by optical neural stimulation, and suggested that elevation in the BOLD signal is the result of local increase in the level of neural activity.

When using optogenetics to study the brain, one should notice that optical neurostimulation inherently is different than sensory or electrical stimulation. For example, stimulating forepaw produces a specific time-chain of reactions in the brain which is not necessarily the same as the chain of reactions produced in optogenetic stimulation. Additionally, depending on the light delivery mechanism, the intensity of stimulation is higher in neurons closer to the light source. Therefore, there might be differences in hemodynamic and electrophysiological responses evoked by either of these stimulations. Such differences were reported by

Scott and Morphy (13) when they observed in ChR2 mice blockade of ionotropic glutamate receptors in cortex reduced the hemodynamic response to the forepaw stimulation while the hemodynamic response to optical stimulation remains strong. In their study, they used optical intrinsic signal imaging (OISI) (14) to monitor changes in the oxygenation state of hemoglobin/blood volume and laser speckle contrast imaging to inspect the blood flow after optical or sensory stimulation. Moreover, they were able to extract the spatial extent of hemodynamic response following optical and sensory stimulations. According to their observations, optical neurostimulation produced IOS response which was more local compared with the sensory stimulation; however, the blood flow response had similar spread in both stimulations.

Later in 2014 Vazquez *et al.* (15) investigated the point spread functions (PSF) of hemodynamic response to the photo and sensory stimulations and the difference between the responses elicited by different types of stimulation. They estimated a Full Width Half-Maximum (FWHM) of about $1283\mu m$ for the OISI response to the photostimulation (1mW of blue light pulsed for 4 sec at 5Hz). The FWHM of the OISI response caused by sensory stimulation was estimated to be $1506\mu m$. Additionally, by placing electrodes at different depths during forelimb stimulation, they noticed the electrical activity was appearing at Layer **IV** neurons (depth of $350\mu m$ to $500\mu m$ in the cortex) while in optogenetic stimulation the activity was occurring at two regions: between the top surface to $400\mu m$ and from $500\mu m$ to $900\mu m$.

These differences should not be neglected when researchers try to reproduce some sensory stimulation by using photostimulation. Nonetheless, optogenetic offers direct and precise (both temporal and spatial) brain stimulation mechanisms to interrogate the brain circuitry compared with electrical or sensory stimulation techniques. Additionally, it is widely accepted that blood flow in the brain, is mostly related to the collective neuronal activity rather than the exact chain of activity. Therefore, optogenetics is lending itself as a proper method of brain stimulation for hemodynamic studies.

1.2 Hemodynamic Recording

The brain hemodynamics can be recorded by several techniques including functional magnetic resonance imaging (fMRI), laser speckle imaging (LSCI), optical intrinsic signal imaging (OISI), multiphoton microscopy, or optical coherence tomography (OCT).

Increase in the neural activity in brain usually result in increase in the blood oxygenation level. Such a correlation between brain activity and BOLD signal makes fMRI BOLD signal one of the main tools for brain functional imaging. However, signaling pathways of brain neurons and vessels are not fully understood yet (16) and are of significant importance for interpretation of BOLD and other hemodynamic signals. Analysis of vasodynamic response to optogenetics stimulation can provide insight to the neurovascular coupling. The effect of optical stimulation on inducing electrical activity and blood oxygenation level has been studied (9), (17), (8), (10), (15), (18), (11), (12). The fMRI data provides insight to the global and local response in blood oxygenation level dependent signal following optogenetic stimulation. However, the spatial and temporal resolution of fMRI is always the major shortcoming of the technology. Moreover, the BOLD signal does not contain detailed information about the induced changes in blood velocity or vasodynamics separately.

Multiphoton imaging is a powerful method in study of functional hyperemia at the cellular level (19), (20). Recently it also have been used to investigate the effect of optogenetic stimulation on arteriolar diameter (21). However, in multiphoton imaging, cellular activity (neurons and astrocytes) and hemodynamic signals are both recorded optically via fluorescence imaging. Adding optical stimulation to this combination, can make the experimental design significantly complicated. Moreover, the field of view in most Multiphoton microscopes is limited to a few hundred microns and does not allow for analysis of vasodynamics in large scale vascular networks.

LSCI (22) and (12) and OISI (13) have also been applied to measure cortical hemodynamics response to optogenetic stimulation. Laser Doppler perfusion monitoring/flowmetry (23), (24), (15), are also tested to record hemodynamic signals in the brain. While they can

provide a larger field of view compared with multiphoton microscopy, the spatial imaging resolution of these techniques is not sufficient to study the small diameter changes in the vessels.

OCT provides a mechanism to image vascular network with a high resolution which allows for simultaneous blood velocity and vessel diameter measurements *in-vivo*. Moreover, since OCT typically uses infrared spectrum of light for imaging, it can be integrated with optogenetic technology and some other optical imaging modalities. Therefore, OCT is considered as a powerful tool for the interrogation of cortical hemodynamics.

The scope of my dissertation is to provide new methods for the investigation of vascular response to local brain stimulation. For this purpose we integrated optical coherence tomography, optogenetic technology, and fluorescence imaging techniques and design a set of biological experiments to address some of the questions in this field.

Chapter 2

Optical Coherence Tomography

2.1 Introduction

Optical Coherence Tomography (OCT) which was introduced in 90s (25) uses a Michelson interferometer to reconstruct high-resolution 3D images up to a few millimeters deep in a specimen. Generally speaking, OCT provides a 3D structural map of the scanned sample, by recording a set of axial scans (A-scans) from different lateral positions of the sample. Each A-scan contains information about photons that are backscattered from different depths in the specimen at that lateral position. By reconstructing A-scans at various lateral positions, an OCT system is able to image 2D or 3D structure of the scanned object. In addition to recording the structural images (26), (27), (28), (29), (30), (31), and (32) an OCT system is capable of detecting moving particles (33), (34), (35), (36), (37), and (38) and their velocity (39), (40), (41), (42), (43), (44), and (45).

In the first OCT scanner (25), they coupled a low-coherence light source to a fiber based Michelson interferometer. The Michelson interferometer splits the beam to two different paths: a reference and a sample path. The sample path illuminates a sample and collects the backscattered light. The reference path leads to a scanning reference mirror which reflects back the light. The optical length of the reference arm is modulated continuously. Light that is received back from the sample and the reference mirror are combined and sent to a photo detector. When the sample and the reference optical path lengths are equal (within the source coherence length) the amplitude of their interference is considerable. As the reference mirror moves and the optical length mismatch between the reference and sample

increase beyond the coherence length of the light source (l_c), the interference amplitude drops significantly and can be assumed there is no interference. Hence, the amplitude of the interference at different mirror positions is correlated with the amplitude of backscattering at the corresponding depth in the sample. Backscattering from particles in the sample with a separation less than l_c can not be distinguished which is considered as of this method (46). For a Gaussian light source at the central wavelength of λ_0 and bandwidth of $\Delta\lambda$ the coherence length is $l_c = \ln(2) \frac{2}{\pi} \frac{\lambda_0^2}{\Delta\lambda}$. This can be considered as the first generation of OCT imaging, which is referred to as time-domain OCT. The need for a scanning reference mirror was a bottle neck for speed and performance of this method. Frequency domain OCT technology later overcame this limitation by analysis of the spectral pattern of interference. This was achieved by either replacing the detector in the conventional time-domain OCT design with a spectrometer (spectral-domain OCT), or by utilizing a new generation of light sources that sweep the illumination wavelength across a desired bandwidth (swept-source OCT).

While swept-source OCT can achieve higher imaging speed, spectral-domain OCT offers a better phase stability and imaging resolution. Phase stability is particularly important for applications such as Doppler velocity measurement and angiography. Therefore, spectral-domain OCT is a better choice for functional OCT imaging. This chapter covers the basic theory and image formation of spectral-domain OCT and recent advances in functional OCT imaging. Moreover, I discuss optical design considerations of a typical spectral-domain OCT imaging system which form the basis for the next chapter in which the details of our custom-built OCT scanner is discussed.

2.2 Theory of spectral-domain OCT image formation

In 1995 Fercher et al. proposed a spectral interferometry technique, based on the Fourier diffraction theorem, to measure optical length of objects along the light beam (z axis) (47). For weakly scattering objects, where the first order Born approximation is valid, they demonstrate that under low-coherence illumination, the spectrum of the backscattered light is proportional to the Fourier transform of the scattering potential of the sample ($F(z)$). Their work can be considered as the foundation of Fourier domain OCT systems. We adapt their approach to estimate the backscattered electric field from a sample when illuminating it with a monochromatic Gaussian beam of power $P_S(k)$ at wavenumber $k = |\mathbf{k}_i| = |\mathbf{k}_s| = \frac{2\pi}{\lambda}$, where \mathbf{k}_i and \mathbf{k}_s are the wavevectors of illuminating and backscattering waves. Assuming the origin of the coordinate system at the surface of a specimen of thickness T , the backscattered electrical field (E_{Sample}^D) at a sufficiently large distance D along the illumination axis can be estimated by (47):

$$\begin{aligned} E_{Sample}^D(\mathbf{k}, t) &= \alpha \sqrt{P_S(k)} e^{(ik \cdot D - i\omega t)} \times \int_0^T F(z') e^{-i(\mathbf{k}_s - \mathbf{k}_i)z'} dz' \\ &= \alpha \sqrt{P_S(k)} e^{(ik \cdot D - i\omega t)} \times FT\{F(z)\}, \end{aligned} \quad (2.1)$$

where FT is the Fourier transform with respect to z , and ω is the angular frequency of monochromatic light, and α is a constant depending on the distances and configuration of the beam. When this beam is interfered with the beam from a reference mirror that is placed at location $z = 0$ (E_{Ref}^D) the combined electric field is:

$$\begin{aligned}
E_{total}^D(\mathbf{k}, t) &= E_{Sample}^D(\mathbf{k}, t) + E_{Ref}^D(\mathbf{k}, t) \\
&= \alpha \sqrt{P_S(k)} e^{(ik \cdot D - i\omega t)} \times FT\{F(z)\} \\
&\quad + \beta \sqrt{P_S(k)} e^{(ik \cdot D - i\omega t)} \times FT\{R\delta(z)\}.
\end{aligned} \tag{2.2}$$

The parameter R is the reflectivity of the mirror and β is the portion of the back-reflection light that is used to produce interference. The mirror is assumed to be infinitely thin so its reflection can be modeled as a dirac delta function at $z = 0$ ($\delta(z)$). Then the intensity of the interfered signal can be calculated as the squared magnitude of this electric field:

$$\begin{aligned}
I(k) &= E_{total}^D(\mathbf{k}, t) E_{total}^D(\mathbf{k}, t)^* \\
&= P_S(k) \alpha^2 |FT\{F(z)\}|^2 + P_S(k) \beta^2 |FT\{R\delta(z)\}|^2 \\
&\quad + P_S(k) \alpha \beta^* FT\{F(z)\} FT\{R\delta(z)\}^* \\
&\quad + P_S(k) \alpha^* \beta FT\{F(z)\}^* FT\{R\delta(z)\},
\end{aligned} \tag{2.3}$$

where superscript $*$ represent the complex conjugate. In general if reflection from the mirror is significantly stronger than the backscattering from the sample, then the first term ($P_S(k) \alpha^2 |FT\{F(z)\}|^2$) has negligible effect and can be ignored. Therefore, the intensity of interfered light at wavenumber k can be approximated by:

$$\begin{aligned}
I(k) &\approx P_S(k) \beta^2 |FT\{R\delta(z)\}|^2 + P_S(k) \alpha \beta^* FT\{F(z)\} FT\{R\delta(z)\}^* \\
&\quad + P_S(k) \alpha^* \beta FT\{F(z)\}^* FT\{R\delta(z)\}.
\end{aligned} \tag{2.4}$$

By measuring the interference intensity at multiple wavenumbers and applying an inverse FT to $I(k)$ it is possible to obtain the scattering potential of the tissue along the z axis

$(F(z))$:

$$\begin{aligned}
IFT\{I(k)\} &\approx IFT\{\beta^2 P_S(k)\} \star R^2 \delta(z) \\
&+ IFT\{\alpha \beta P_S(k)\} \star F(z) \star R \delta(-z) \\
&+ IFT\{\alpha \beta P_S(k)\} \star F(-z)^* \star R \delta(z).
\end{aligned} \tag{2.5}$$

The operator \star is a convolution operator. Here we assumed α , β , and R are real numbers independent of the wavenumber. If $P_S(k)$ is a smooth function of the wavenumber, then its IFT is mostly centered at the origin and can be approximated by a dirac delta function $\delta(z)$:

$$IFT\{I(k)\} \approx \beta^2 R^2 \delta(z) + \alpha \beta R \times F(z) + \alpha \beta R \times F(-z)^*. \tag{2.6}$$

By placing the origin of the coordinate system on the tissue surface, we know the sample is confined to positive z values. Hence, $A(z) = IFT\{I(r, k)\}$ on the positive z axis represents the scattering potential of the object which sometimes is referred to as depth profile. $A(z)$ is a hermitian function of z and on the negative z axis $A(z)$ is the complex conjugate of its values on the positive axis.

2.2.1 Axial resolution

In practice, the light source has a limited bandwidth which causes the $IFT\{P_S(k)\}$ to have a finite width. This width is the axial resolution of spectral-domain OCT imaging. For a given power spectrum $P_S(k)$ It is possible to use the Fourier theorem to calculate the axial resolution of OCT imaging. For a light source with a Gaussian spectrum of bandwidth $\Delta\lambda$ at the central wavelength of λ_0 the axial resolution is:

$$\delta z = \frac{2 \ln(2)}{\pi} \frac{\lambda_0^2}{\Delta\lambda} = l_c. \tag{2.7}$$

The theoretical resolution in spectral-domain OCT imaging is the same as the coherence length of light source (l_c). If α or β are not uniform across the light spectrum, the axial resolution can be larger than Eq. 2.7. The lateral resolution in an OCT imaging system is a function of the central wavelength and the numerical aperture of the imaging system and is decoupled from its axial resolution. For more in depth discussions and analysis of OCT image formation we refer the readers to many articles and books including but not limited to (48; 49; 50; 51; 52; 27; 53; 41; 54; 55; 56; 57; 58).

2.2.2 Imaging depth

In spectral-domain OCT imaging, the depth of the scatterer and the interference pattern are related via Fourier transform (Eq. 2.6). As a result, when the depth of scattering (z) increases, the maximum frequency in the interference pattern ($I(k)$) also increases. The spectrometer; however, acquires a finite number of samples from the interference pattern and, in practice, a discrete Fourier transform (DFT) is used to convert the interference pattern to a depth profile. According to the Nyquist sampling theorem, the spectral resolution of the spectrometer determines the maximum detectable frequency in the interference pattern ($I(k)$) and, hence, the imaging depth. When a scatterer falls outside this imaging range, it produces an interference pattern with a frequency larger than the Nyquist limit. Due to aliasing, the depth of such sample is miss-represented in the OCT images. If the number of pixels on the camera is N and the measured spectral bandwidth (in wavenumber) is $\Delta\kappa$, then the spectrometer's sampling interval is estimated by $|\delta\kappa| = |\frac{\Delta\kappa}{N}| \approx \frac{2\pi}{\lambda_0^2} \frac{\Delta\lambda}{N}$. Therefore, according to Eq. 2.6, the imaging range of the SD-OCT device is (48; 51; 57):

$$2 \times z_{max} = \frac{1}{2} \frac{1}{\frac{1}{\lambda_0^2} \frac{\Delta\lambda}{N}} = \frac{\lambda_0^2}{2 \frac{\Delta\lambda}{N}} \quad \text{or} \quad z_{max} = \frac{N\lambda_0^2}{4\Delta\lambda}, \quad (2.8)$$

where z_{max} is the maximum imaging depth without aliasing effect. z_{max} is directly proportional to the number of pixels in the spectrometer. For a large imaging range, a detector with sufficiently high number of pixels should be selected. According to Eq. 2.8, the imaging range can also be furthered by increasing the central wavelength or decreasing the bandwidth of the light source. However, either of these changes negatively affect the imaging resolution. Therefore, once the spectrometer is designed, there is a trade-off between the maximum imaging depth and the axial resolution of the system.

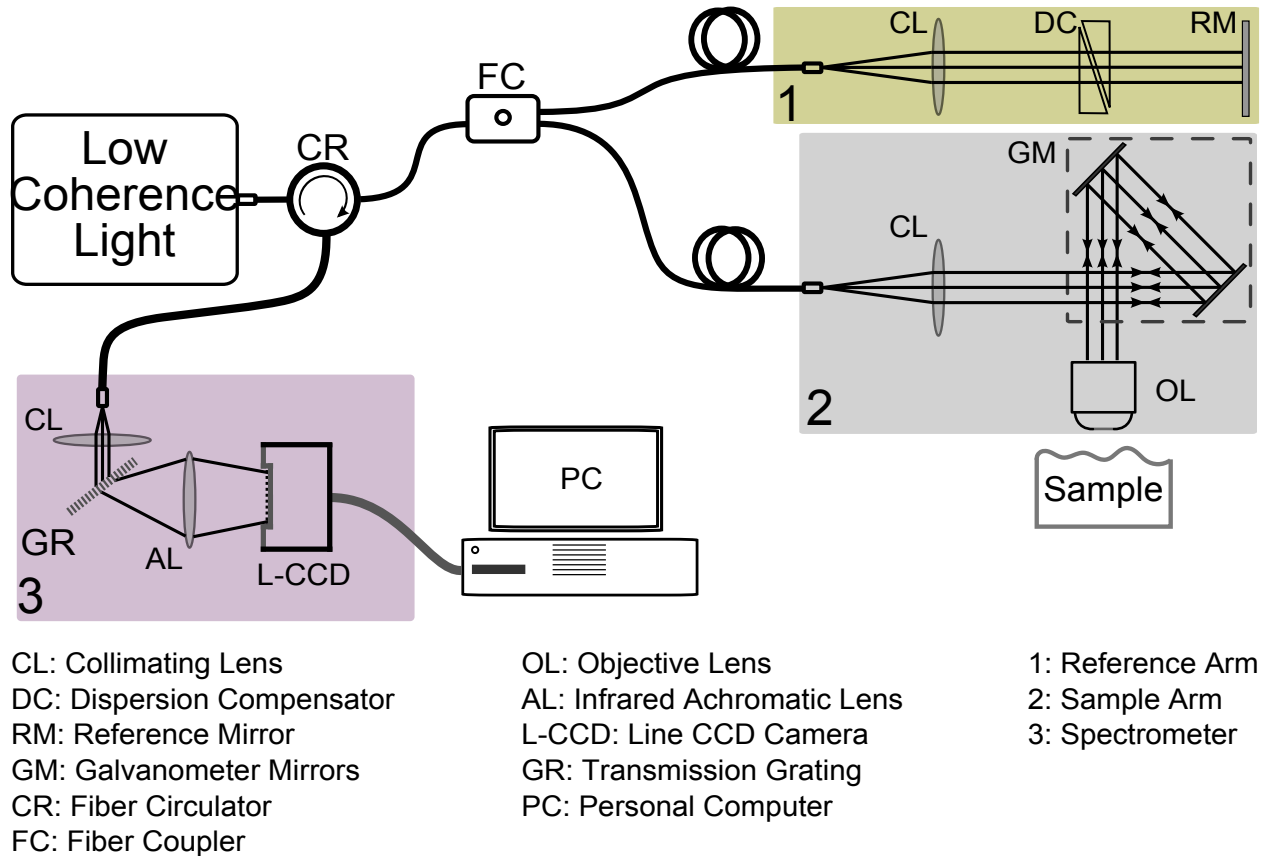


Figure 2.1: A fiber-coupled spectral-domain OCT scanner. It uses a low-coherence light source to illuminate sample (path 3) and reference arms (path 1). In the sample arm a set of galvanometric mirrors raster scan a sample. Light that is collected back from reference and sample arms recombine to form interference patterns which are detected by a spectrometer (path 3).

Eq. 2.6 formulates basics of a spectral-domain OCT imaging system where its axial

resolution can be obtained via Eq. 2.7. While this section covered the theory of OCT image formation, to achieve OCT imaging with desired specification, the scanner optical and optomechanical components of the system need to be designed cautiously. In the following sections we discuss the design considerations for an SD-OCT system and explain how they can influence the final resolution of the system.

2.3 Design Considerations

In the previous section we discussed briefly the effect of light source spectrum on the axial imaging resolution. However, yet there are some details that need to be considered when selecting a light source which is discussed in this section. All SD-OCT systems are consisted of three major compartments: a spectrometer, a sample arm, and a reference arm (Figure 2.1). In this section we cover some design criterion for each compartment.

2.3.1 Light source

According to Eq. 2.7, a low-coherence light source is essential to obtain a fine axial resolution. Since the axial resolution of an OCT image is directly proportional to the square of the central wavelength of the light source and inversely proportional to its bandwidth, similar axial resolutions could be achieved in different regions of the spectrum. When using longer wavelengths an increasingly wider light spectrum ($\Delta\lambda$) is required to maintain the axial resolution. The main drawback of such long wavelengths is their effect on the lateral resolution which is discussed later in this section. On the other hand, while shorter wavelengths can provide better lateral resolution, in majority of biological samples the scattering effect increases at shorter wavelengths which limits the effective imaging depth of an OCT. Therefore, the central wavelength of the light source should be chosen based on the application and the tissue of interest. For biological samples, both visible (e.g. (59; 60; 61; 62)) and near infrared wavelengths (e.g. (63; 64; 65)) have been used.

The light source should be stable and provide a low-noise output to obtain high quality images. Superluminescent Light emitting Diodes (SLDs or SLEDs) are popular for spectral-domain OCT applications since they can provide low-noise and stable low-coherence light while they demand less maintenance in contrast to pumped lasers. With the recent advances in supercontinuum laser technology, stability of this type of light sources have improved and their noise level has reduced. Supercontinuum laser sources provide light with an ultra-wide spectral bandwidth and are used to obtain a fine axial imaging resolution. They provide more optical power in comparison with SLDs. For applications that high power and large light spectrum are needed, such light sources are a proper choice. However, for applications that require a high phase stability and low noise levels, such as Doppler velocimetry and OCT angiography, SLDs remain as a superior choice to supercontinuum light sources.

2.3.2 Sample arm

Design of a sample arm in an OCT system depends on the desired lateral resolution, maximum field of view, and the spectral bandwidth of the light source. Therefore, proper design and implementation of the sample arm is essential to achieve the desired specifications. For example the axial resolution theoretically depends on the bandwidth of the light source; however, it still can be negatively influenced by a poor design of the sample arm if the chromatic aberrations cause significant spectral filtering in the sample arm ((66)). A sample arm basically consists of four major components, a collimator, two galvanometric mirrors, intermediary optics, and an objective. Each component is influential in the specifications of the system.

Collimator

A collimator is a lens or lens mechanism that is placed in front of an optical fiber to produce a collimated beam. In combination with the rest of the arm, it forms an imaging system that images the fiber tip on the sample and, vice versa, it images the focal plane of the

objective on the tip of optical fiber. In the forward path, when imaging the fiber on the sample, the collimated beam waist and the collimated beam quality have significant impact on the lateral resolution. The collimated beam radius depends on the numerical aperture of the optical fiber and also the effective focal length of the collimating lens system. When the fiber is placed at the focal plane of the collimator, the beam radius is approximated by:

$$w = f.\theta_{fiber} = f.\lambda/(\pi w_{fiber}), \quad (2.9)$$

where f is the effective focal length of the collimator, and w_{fiber} is the mode radius of the fiber at wavelength of λ . The mode radius of a fiber is dependent on the wavelength, and it slightly changes across the spectral range of a wide-band light. In OCT applications this dependency is neglected and the mode radius of the central wavelength is used in this calculation. By increasing the focal length of the collimator it is possible to produce a larger collimated beam waist which leads to a smaller spot size on the sample (as discussed later in this article). When using a large focal length, the aperture of all the intermediary optical components, including the galvanometric mirrors, need to be selected accordingly to avoid beam truncation and signal loss or image artifacts.

In the return path, the collimator couples the photons, which are collected by the objective lens, to the single mode fiber. Optical aberrations or mismatch between the beam profile at the focal of the collimator lens and the mode of the optical fiber causes loss in the signal and drop in imaging quality. The least power loss happens when the returning beam waist matches the effective aperture of the collimator. Ideally, the collimator and the objective lens should be selected such that the mismatch loss is minimum.

Optical aberrations in the collimating lens mechanism can degrade the quality of OCT images first, by introducing imperfections to collimated beam in the forward path which can increase the sample spot size. Second, by reducing the coupling efficiency to the fiber that decreases signal to noise ratio (SNR) in OCT images. Spherical and chromatic aberrations

are two important imperfections that can be caused by a collimating lens system. A large spherical aberration reduces the lateral resolution of OCT images and the coupling efficiency of the backscattered photons. Longitudinal and lateral chromatic aberrations can cause the axial and lateral position of focal spot to change as a function of wavelength. This affects the coupling efficiency across different wavelengths which may degrade the axial resolution of the system (67) as well as its lateral resolution. Therefore, it is critical to select a proper collimator to achieve the desired imaging resolution and SNR.

A conventional bi-convex or plano-convex lens may be able to produce a desired beam size; however, due to spherical and chromatic aberrations that is introduced by these type of lenses, the quality of the resulting beam is not satisfactory for high resolution OCT applications. Typical achromatic doublets introduce slightly less chromatic and/or spherical aberrations, but still the aberrations can prevent achieving a high lateral resolution.

A higher quality of collimated beam can be achieved by use of an aspherical lens. Aspherical lenses are more expensive, and are usually designed to have short effective focal lengths. Quality of Gaussian beam that is produced by this type of lenses is acceptable for most OCT applications. For extreme accuracy one can use a lens mechanism instead of a single lens; however, for most OCT applications an aspherical lens can deliver the desired beam quality.

Besides the lens type, the placement of the fiber with respect to the lens can affect the quality of the beam. Small misalignments (tilt or misplacement) of the fiber and lens with respect to each other can also introduce aberrations to the beam and affect the OCT resolution. When using a lens with small aperture, such misalignments cause beam truncation, which results in loss of resolution and artifacts in the OCT images. Therefore, the fiber and collimating lens should be aligned very carefully. There are collimating packages that are offered by different vendors. The packages are designed in such a way that for the designed wavelength and fiber radius, they can deliver high quality beam without need for fine alignment. Most collimating packages consist of a single aspheric lens. Some others, which are designed to

produce high quality Gaussian beam (M factor close to 1), use a combination of multiple lenses to reduce the aberrations. Typically this type of collimator lenses can provide a better beam quality, and higher coupling efficiency to the fiber but increase the cost of the system. Another important factor when choosing a collimator lens is its anti-reflection (AR) coating. Proper anti-reflection coating on the lenses in the sample arm, including the collimator, is important to acquire high quality OCT images as AR coating decreases the light reflection from the surface of the optical components and improves the image SNR. A good AR coating can reduce the reflection loss to as low as 0.2dB, while improper coating can result in a power loss up to 3dB or higher. More importantly, the strong light reflection from surfaces which are not covered with proper AR coating introduces image artifacts as horizontal lines across the OCT images.

Galvanometric mirrors

To obtain 2- or 3-dimensional images of a specimen, generally the OCT beam raster scans the tissue by using a laser scanning mechanism (Figure 2.1). Two galvanometric mirrors rapidly scan the OCT beam spot on the sample along two orthogonal directions (x and y), while depth profile at each (x, y) location is obtained via low coherence interferometry (Eq. 2.6). For fast and high resolution OCT imaging, it is necessary to use a galvanometric system which can achieve high scanning speeds with accurate control over the angle of the mirrors. Mechanical vibrations or timing jitter in the mirrors can affect the accuracy of OCT images or can produce artifacts in Doppler measurements and angiography images. Therefore, a servo circuitry which is equipped with a closed loop system control is essential to achieve high stability and accuracy in positioning and scanning speed of the mirrors. The size of mirrors affect the maximum speed that the galvanometric scanner can achieve. Small mirrors make it possible for the scanner to operate at higher speed; however, the mirrors must be sufficiently large to avoid beam truncation. In contrast, since the OCT resolution is dependent on the collimated beam waist, the OCT beam can not be selected arbitrarily

small. When a small beam and fine OCT lateral resolution are required simultaneously, it is possible to use a small diameter collimator followed by a scan-tube lens mechanism with a proper expansion ratio after the galvanometric mirrors to expand the OCT beam prior to the objective lens. Resonant scanning mirrors can achieve very high scanning rate in comparison with the galvanometric mirrors. However, their lack of flexibility to scan desired patterns limit their application in OCT imaging. Moreover, in most SD-OCT applications the imaging speed is limited by the detector line rate and, in practice, the speed of SD-OCT imaging is not limited by the speed of typical galvanometric scanning mirrors.

The physical dimensions of the mirrors dictates a separation between the two mirrors to avoid collision. The optimal alignment of the mirrors is to place back focal plane of the objective in the middle point between them. In such an arrangement, none of the mirrors satisfies the telecentric configuration (68). Telecentricity is important in OCT imaging and is discussed in the following section. The separation between the mirrors should be limited to the minimum possible distance otherwise it compromises the accuracy of OCT images. If the placement of the mirrors is far from telecentricity conditions, the OCT images suffer from a depth dependent magnification, where this magnification is different for the x and y directions. If the separation is small, commonly this imperfection is negligible. As the distance between the mirrors increases, this deformity also becomes noticeable and can introduce errors in measurements, especially when using a high magnification objective lens. In conditions that the mirrors can not be placed sufficiently close to each other, this problem can be avoided by use of a relay optics between the mirrors. This relay mechanism projects the image of the first mirror (x -axis) on the other mirror (y -axis) (69), (70) and the second mirror should be placed at the back-focal plane of the objective. Such a relay mechanism increases the size and cost of the OCT system. Another approach is to use two-axis tilt mirrors (71), (72), which uses same mirror to scan x and y directions. Generally, the galvanometric mirrors are able to provide a more linear and faster scanning compared to two-axis tilt mirrors. The recent advances in microelectromechanical systems (MEMS) devices reduced this gap;

however, with the current technologies the speed of galvanometric mirrors out perform two-axis tilt mirrors for most OCT applications.

The surface quality of galvanometric mirrors is important in low-coherence interferometry. Curvature on the mirrors' surface introduces phase-front distortion to the collimated beam which negatively impacts image quality. The scanning mirrors should be stiff so during mechanical tensions at the time of large angular accelerations the mirror's surfaces remain flat. These considerations may affect the thickness (weight) and the material that are used in the construction process of the mirrors, which limit the speed and settling time of the galvanometric system. Therefore, when selecting the scanning mirrors their speed as well as the mirror size and angular accuracy should match with the desired parameters of the OCT system.

Objective lens

Generally, in an OCT system, the lateral resolution and maximum possible field of view are limited by the objective lens. A high lateral resolution, can be achieved by use of an objective that is designed to work at large numerical aperture (NA). The lateral resolution of an OCT is defined as the radius of the beam spot at the focal of objective (57), (58). For a Gaussian beam of radius r_0 and wavelength λ that is incident on a lens with the focal length of f , the spot size is inversely proportional to NA (73):

$$\delta x = \frac{2\lambda f}{\pi r_0} = \frac{2\lambda}{\pi NA}, \quad (2.10)$$

where δx is the theoretical lateral resolution. Increasing the NA increases the divergence angle of the Gaussian beam which results a reduction in the depth of focus. Depth of focus (DOF) of a Gaussian beam is the range that the beam waist radius stays smaller than $\sqrt{2}\delta x$. Generally DOF is considered as the range in which the resolution is maintained close to the desired value, and outside this range the resolution drops quickly. For a Gaussian beam the

depth of focus can be calculated by (73):

$$b = \frac{\pi \delta x^2}{\lambda} = \frac{4\lambda}{\pi NA^2}. \quad (2.11)$$

Therefore, DOF is directly proportional to the square of the spot size which poses a fundamental trade-off between the lateral resolution and the depth of focus. An optical setup with a low NA (~ 0.1) strikes a good balance between resolution and DOF of an OCT scanner in the infrared spectrum. This is in contrast with many other microscopy technologies such as multi-photon fluorescence imaging which demand a large NA to perform optical sectioning. For optical sectioning, a high numerical aperture is desirable since the beam outside of depth of focus diverges very quickly and the effect of out of focus regions of a sample can be ignored. In OCT low-coherence interferometry separates the photons that are backscattered at different depths in the tissue. Therefore, it is desirable that the OCT scanner possess a uniform spot size across the depth of interest. This imposes a fundamental trade-off between the lateral resolution of an OCT scanner and its depth of focus.

By use of a light source with shorter wavelengths it is possible to strike a better balance between the lateral resolution and the depth of focus. However, a shorter wavelength experiences larger scattering in most biological tissues and has shorter penetration depth. In such samples, the scattering reduces the signal to noise ratio and quality of OCT images at short wavelengths. Therefore, depending on the application and the tissue properties, selecting a proper wavelength has a considerable impact on the quality and resolution of OCT images.

When a long central wavelength and a large depth of focus are necessary for OCT application, it is recommended to use a Bessel beam. A Bessel beam with a spot size similar to a Gaussian beam, offers a longer depth of focus (74), (75), (76). The compromise here is that Bessel beams have relatively strong side-lobes which can affect the accuracy of some

OCT measurements. Also implementing a system with a Bessel beam costs more than with a Gaussian beam due to increase in the cost of some optical components.

Optical aberrations that are introduced by the objective lens in the sample arm can degrade the resolution of the imaging system. Low chromatic aberrations (longitudinal and lateral) are important when a light beam with a large bandwidth is used for OCT imaging. The chromatic aberrations prevents different wavelengths to come into focus at the same focal point. Ultra-wideband OCT light sources such as super continuum lasers are becoming more popular to achieve high axial resolution. If the objective lens is not designed for such a large bandwidth, the chromatic aberrations prevent the scanner to achieve the theoretical lateral resolution. Proper coating of the objective for the desired wavelengths is also important to reduce the back reflection of the light from the objective. Since most objective lenses have complex structure composed of several layers of different types of glass, the strength of the backreflection can be comparable to or stronger than the tissue backscattering.

One other important aberration in OCT imaging is astigmatism which may confine the area of the diffraction limited resolution to the center of field of view. Astigmatism causes sagittal and tangential light rays to focus at different axial positions. Astigmatism reduces the lateral resolution of the OCT device when scanning the off-axis regions of a specimen. Besides the resolution, optical aberrations reduce the signal to noise ratio of OCT images. In a typical OCT device, the objective collects the photons that are backscattered from the tissue, and sends them back towards the mirrors and the optical fiber. The fiber core acts as a pinhole and rejects out of focus light. This significantly reduces the intensity of the light at the out of focus region significantly.

Other parameters that should be considered when selecting an OCT objective are magnification and telecentric property. Objective magnification determines the relationship be-

tween the change in angle of the incident beam and the transversal displacement of the spot on the sample. A low magnification objective lens requires small mirror angles to cover a field of view. While, the same scanning angles cover a smaller region of the sample when a high magnification lens is used. For typical OCT imaging, low magnification objectives with large FOV are desirable. The design of most commercially available low magnification lenses does not allow realization of small spot sizes, which is partially due to cost considerations. This couples the magnification of a lens to the imaging resolution which imposes a technical trade-off between the resolution and the field of view.

For laser scanning mechanisms such as OCT, a linear relationship between the scanning angle and the transversal displacement allows the device to obtain a uniform sampling across the transverse plane by simply swiping the angle of the galvanometric mirrors while the detector is recording at a constant rate. Such an objective is usually called an $f - \theta$ lens, since the displacement of beam is equal to the product of the effective focal length of the lens (f) and the angle of incident of the beam (θ). In general, $f - \theta$ lenses are able to produce a flat imaging plane and uniform resolution across the imaging plane. A non $f - \theta$ lens realizes a nonlinear relationship between the mirror angle and the beam displacement on the sample. This effect can cause a non-uniform magnification across the transverse plane and distortion in the recorded OCT images. It is important to select an objective lens that introduces a low level of distortion. For OCT applications is the uniformity of magnification at various depths is desirable. For such a purpose the lens must be used in the telecentric configuration. That is, when the geometrical center between the mirrors is placed at the back focal plane of the objective. A telecentric $f - \theta$ lens (which is usually referred to as a scan lens) provides a beam that is perpendicular to the flat imaging plane and its magnification is uniform inside the objectives depth of focus.

The above mentioned factors are related to the performance of an objective lens. Some other considerations are related to the mechanical properties of the objective. The distance

between the back focal plane of lens and the surface of the lens is called back focal length (BFL). The scanning mirrors should be placed such that the geometrical center of the mirrors collocates with the BFL of the objective. If the BFL is sufficiently large then the placement of the mirrors are more convenient. For many objectives that are designed for high resolution imaging, the BFL is short and it is impossible to place the mirrors in the designated position. In such conditions a relay mechanism is necessary to image the mirrors on the desired positions (68), (70), (77). Working distance in an objective, is the distance between the focal plane and the surface of the lens. A large working distance allows for more space between the sample and lens. This is especially important for *in-vivo* experiments when there are other devices and equipment attached to the subject, or the organelle under study, e.g. lung or heart, is surrounded by tissue. In such conditions large working distance is very beneficial.

2.3.3 Beam combination

For many applications, it is beneficial to integrate OCT imaging with other optical methodologies, such as fluorescence imaging, white light imaging, or Laser speckle imaging. Such a combination can be achieved by placing a dichroic beam splitter in the path of OCT beam in the sample arm. The dichroic mirror can be a long or short-pass beam splitter; however, each of them can introduce some imperfections or artifacts to the OCT image. Most dichroic mirrors are designed to work with a collimated beam and they should be placed in the sample arm accordingly. This becomes more crucial when a long-pass dichroic mirror is being used when the OCT beam is passing through this component. When a diverging or converging OCT beam passes through a slab of glass, different portions of the beam travel different lengths inside the glass which can introduce optical aberrations with profound impact on the quality of the OCT images.

2.3.4 Reference arm

The reference arm in an OCT system replicates the light path of the sample arm. It may consist of the same components as the sample arm; however, it is possible to use dispersion-compensating (DC) blocks instead of some components such as the objective lens to reduce the cost. A DC component has dispersion properties similar to the original component. In the reference arm a mirror is used in place of a sample. The path length of the reference arm should match the sample arm. In practice it is desirable to place the reference mirror on a micromanipulator to adjust the reference arm length. In many applications this length is adjusted such that the equal path length in the sample arm is placed a few hundred micrometers before the focal plane of the objective.

Since the reflection coefficient of a mirror is larger than a typical sample, the light that is collected back by the optical fiber in the reference arm is stronger than the collected light from the sample arm. A strong reference beam increases the signal to ratio (SNR) of OCT images. Also, a strong reference intensity reduces the visibility of the image artifacts caused by interference occurring between the reflected light from different sample reflectors. In some cases, a long exposure time is necessary to detect the weak backscattered light from deep tissue. In such cases a strong reference beam saturates the detector and makes the reconstruction impossible. To adjust the intensity of the reference beam one can place a variable attenuator or aperture in the reference arm. An alternative method of balancing the intensity of reference beam, with respect to the sample beam, is to use a variable fiber coupler instead of the fixed ratio fiber couplers as discussed in the following sections.

2.3.5 Spectrometer arm

The paths of photons that are collected in the sample and reference arms are combined using a fiber coupler. If a 50:50 coupler is used, the sample/reference power is equally divided between the output ports of the coupler and there is no preference between the

ports. When a coupler with a ratio other than 50:50 is being used to deliver more power, to one of the arms, then the same port that is connected to the light source should be used to detect the interference. In this condition, it is possible to use a single mode fiber optic circulator in the path of the light source to divert the path of the returned photons toward the detection (spectrometer) arm.

The spectrometer arm usually consists of a single mode fiber, a collimating lens, a diffraction grating, a lens (or lens mechanism), and a line detector. The light that is emitted from the single mode fiber is collimated using the lens and illuminates on the diffraction grating. The grating diffracts different wavelengths to different angles and by use of a lens mechanism in front of the grating, the diffracted light is focused on a line.

The detector in SD-OCT can be a line CCD camera that is placed at the focal of the spectrometer lens. The combination of source bandwidth, diffraction grating, lens mechanism, and camera pixel size determines the axial imaging resolution and maximum depth that SD-OCT can image as partly discussed in section 2.2. The overall spectral bandwidth that is being detected by the camera determines the axial resolution. A larger effective bandwidth, results in a better axial resolution (Eq. 2.7). The maximum imaging depth depends on how finely the light spectrum is being sampled by the camera. If the sampling is denser, by either using a smaller detector pixel size or a lensing mechanism of longer focal length, then the scanner can provide a larger imaging depth; however, it mandates using more number of pixels to capture the same bandwidth. Besides the number and size of camera pixels and also the source bandwidth, the optical performance of the grating and imaging lens are important in the quality of the images. There are commercial spectrometers available which offer easy installation; however, it is not possible to tune and adopt them for every arbitrary light spectrum. Here we present a simple and fast guide line on how to select proper components and implement an efficient spectrometer for OCT applications.

Optical grating

When selecting a grating, its designed wavelength, efficiency over the desired bandwidth, and polarization sensitivity should match with the application. Transmission holographic gratings strike a good balance between efficiency, working spectrum, and insensitivity to minor misalignments, which is beneficial for OCT applications. Blazed gratings, in comparison with holographic gratings, offer a better efficiency around their designed wavelength. However, their efficiency drops quickly for the wavelengths that are far from the central wavelength. This reduces the image signal to noise ratio (SNR) and/or degrades the OCT axial resolution by reducing the spectral bandwidth of the spectrometer.

For a non-polarized light source, a grating with less polarization sensitivity is beneficial. If its efficiency is highly polarization dependent, it reduces the optical power of the diffracted light and the SNR of OCT images. The grating needs to be aligned very carefully since the OCT beam should be incident on the grating with a specific angle with respect to the grooving. Another advantage of transmission gratings is their lower sensitivity to the imperfections in the angle of incidence (AOI), when compared with reflection gratings. However, to get the maximum performance, the optical alignment should provide an AOI that is matching the grating specifications. Overall, transmission holographic gratings with small polarization preference meet the requirements of most OCT applications.

Lens Mechanism

The spectrometer lens mechanism focuses the light dispersed by the grating on a line detector which is placed on its focal plane. In this configuration the spectrometer lens virtually acts as a scan lens. Different wavelengths exit the grating at different angles and are focused at different positions on a line along the direction of light dispersion (Figure 3.10).

Therefore, at the focal plane of the lens the wavelengths are spatially separated, and each pixel of the detector is receiving a portion of the spectrum based on its location. The lens FL should be selected such that the desired part of source spectrum is projected on the

extent of the sensor array. The bandwidth that is projected on the detector determines the theoretical axial resolution of the OCT system. If the FL is too large, only a portion of the source bandwidth is received by the detector that degrades the axial resolution. The SNR of OCT images reduces as well due to the power loss in the spectrometer. In this case, the spectrum is sampled more densely which results in a larger imaging depth. In contrast, if FL is too small, some of the camera pixels practically are not receiving sufficient photons are not contributing to the reconstruction process. In such conditions the axial resolution still can be obtained by Eq 2.7 where $\Delta\lambda$ is the bandwidth of the light source. However, because of larger sampling interval, the maximum imaging depth decreases (Eq. 2.8).

Since the pixel size is not infinitesimal, each pixel integrates over the portion of the spectrum that is projected on the its sensor area. Therefore each detector's pixel acts as a low-pass filter which smoothens the interference patterns. In this process the fringes with high frequency are attenuated. Since a deeper scatterer creates a higher frequency in the interference pattern, such a low-pass filter results in a depth dependent attenuation ((78)). This signal fall-off, which sometimes is referred to as sensitivity drop-off, causes the SNR of typical OCT images to drop quickly as the depth increases.

Besides the physical dimension of detector area, the focal spot size of the lens mechanism is another factor that can cause signal fall-off. When the spectrometer spot size is smaller than the detector's pixel size this effect can be ignored. When the spot size is the comparable or larger than the detector's pixel size, energy of each wavelength spreads to more than one pixel which can be modeled by another low-pass filter being convolved with the interference signal, and worsens the signal fall-off. The spot size on the detector is directly proportional to the FL of the lens mechanism and inversely related to the collimated beam diameter (Eq. 2.10). If a lensing system with a large FL is required, then the size of the collimated beam, that is incident on the grating, should be selected accordingly to realize a small spot size on the detector. Optical aberrations such as astigmatism and Petzval field curvature result

in a non-uniform spot size along the detector plane. When the aberrations are significant, the varying spot size causes an attenuation in the interference pattern which varies as a function of the position across the detector. Therefore these aberration types result in an attenuation which is wavelength dependent. This acts as a spectral filter which may degrade axial resolution of the system as the depth increases. By use of proper lens mechanism and collimating lens, it is possible to produce sufficiently small spot size on the detector and reduce the optical aberrations to achieve a high axial resolution and reduce signal fall-off.

Detector

In recent years several line-CCD cameras are designed and manufactured particularly for SD-OCT imaging. Their spectral response, dark noise, exposure time, data transfer rate, and pixel size allow for fast, high-resolution, high-dynamic range, and high-sensitivity OCT imaging.

The sensitivity of an OCT scanner is defined as the inverse of sample reflectivity which produces an amplitude equal to the noise amplitude in the OCT image. This value has a great impact on the image quality and is affected by several parameters in the detector. The dynamic range is defined as the ratio between the minimum reflectivity that causes saturation and the noise level in the detector. Therefore, this value represents the span of reflectivity values in the sample arm that can be detected by the scanner. Practically, the dynamic range of a system is smaller than its sensitivity. The typical values for sensitivity and dynamic range are $\sim 100\text{dB}$ and $\sim 60\text{dB}$, respectively (58). The detector array records the reference and sample signals along with the interference signal. Generally, the amplitude of the reference signal is much stronger than the interference signal; therefore, the detector should have large photoelectron capacity to record weak interference signals that are superimposed on top of the strong reference signal. Shot noise, readout noise, thermal noise, and analog to digital conversion noise are some types of noise that may limit the sensitivity of an OCT system. It is desirable for a detector to work at the shot noise limit which is a

fundamental noise in imaging techniques. A small receiver noise is essential for a SD-OCT detector to take advantage of its large photoelectron capacity and to achieve a shot noise-limited performance (41), (52), (54). Since in SD-OCT the depth profile is calculated by using a discrete Fourier transform, to achieve a dynamic range of 60dB in the image it is not required for the detector to capture the interference signal with such a large dynamic range. A detector with 12bits Analog to Digital converter provides sufficient bit depth to achieve sufficient dynamic range and low discretization noise for SD-OCT imaging.

The scanning speed of a SD-OCT imaging system is mainly limited by the line rate of its detector. Commercially available line CCD cameras are able to provide up to $> 240k$ lines per second at cost of larger readout noise and smaller dynamic range compared to lower speeds. Although, such detectors are sufficiently fast for many applications, faster and more sensitive detectors are required in certain *in-vivo* experiments e.g. to reduce motion artifacts or perform Doppler velocimetry of fast moving particles. With the new state-of-the-art electron-injection based detectors (79) it might be possible to improve the sensitivity and dynamic range of the OCT imaging systems in the future and achieve higher imaging speeds. The spectral response of the detector acts as a filter, similar to other optical components. If the spectral response is smaller than the light source or such that it deforms the spectrum of the recorded signal in comparison with the source, then it can degrade the axial resolution of the OCT imaging system. Most line detectors have fairly flat response over a large spectral range and one can ignore their effect on the axial resolution. However, for ultra-high resolution the spectral range of the detector should match with the light source.

In diffraction-based spectrometers, each wavelength is diffracted to a different direction. The angle between the diffracted light beam and the optical axis of the grating is proportional to the light wavelength and not its frequency (κ space) (51). Consequently, the the line CCD non-uniformly samples the interference pattern in κ space. Applying the Fourier transform (Eq. 2.6) to this sampled interference signal to obtain the depth information, prior to any

further processing, results in low resolution images and the reconstructed image suffers from low signal to noise ratio (SNR). As a result, the majority of spectral-domain OCT systems perform a resampling as a part of the OCT signal processing procedures to convert a signal that is recorded in λ space to a signal in κ space, as is covered later in this section. However, some hardware solution has been offered by some groups to avoid the resampling process. For example Hu et. al (67) and Gelikonov et. al. (80) have used a custom designed prism between the grating and lens in their interferometer to compensate for this nonuniform frequency sampling property of the grating. However, this method involves costume design of specific prism. Placing the prism in the spectrometer to obtain uniform sampling in the frequency domain is a very sensitive and time-consuming task. Moreover, there are some imperfections, like the mismatch between the dispersion in sample and reference arms, that eventually demands for a software based resampling process and can not be solved by a prism in the spectrometer arm. Therefore, a soft processing would be necessary to obtain uniformly sampled signal in the frequency domain (78). The majority of spectral-domain OCT systems perform the resampling as a part of the OCT signal processing procedures as is covered later in this section.

2.3.6 Fibers, Coupler, and Circulator

For OCT applications single mode optical fibers and single mode fiber-based components are required. Core diameter of such fibers are in the range of a few microns to 10 microns depending on the central wavelength. The designed spectral bandwidth of the fibers should match with the light source bandwidth. Otherwise the coupling efficiency might be very low, or the fiber may act as a multimode fiber. A multimode fiber is not suitable for OCT applications, since in different modes the light experiences different optical path lengths which causes numerous artifacts in the OCT image which practically make it impossible to perform imaging.

The fibers should also provide angled physical contact (APC) with the rest of the system to

avoid image artifacts. Noticeable back reflection of light from any object can contaminate OCT images. The back reflection from the surface of the fiber tip is sufficiently strong to cause image artifacts. For this reason, the fibers need to have an angled cut to reduce the power of the back reflected light that is being coupled back to the fiber. When using single mode fibers with angled cut, the rest of the fiber based components (collimators, fiber coupler, light source, and optical fiber circulator) need to be selected accordingly.

2.4 Functional spectral-domain OCT

Several methods have proposed to use OCT for measuring blood flow or visualizing vascular network in a tissue. This requires extra steps of signal and image processing which is covered in this section.

2.4.1 Measuring Blood Velocity

Phase stability in spectral-domain OCT allows to precisely measure the phase of the spectral interference at each depth (81). On the other hand, movements (even smaller than the imaging resolution) along the OCT beam leads to some significant change in the phase of the spectral interference. In 2002, Leitgeb *et al.* showed that the phase information can be used to estimate the flow velocity at an angle α with respect to the light beam by taking two scans from the same position and calculating velocity, v , via (82):

$$v(z) = \frac{\Delta\Phi(z)}{T \cos(\alpha)} \frac{\lambda}{4\pi}, \quad (2.12)$$

where z is the depth at which we are measuring the flow velocity, T is the time interval between the two scans from the same position, $\Delta\Phi(z)$ is the phase change at depth z , and λ is the central wavelength of the light source.

This technique is known as phase resolved Doppler optical tomography (PR-DOT) and has

been used widely to measure bidirectional velocity of blood *in-vivo* (81), (83), (34). Since phase resolved Doppler determines the velocity by measuring the rate of phase change, if the time interval T is too big, then the phase change potentially exceeds $\pm\pi$ and aliasing effect happens. As a result, the maximum velocity that can be detected by this technique is limited to: $\pm\frac{\lambda}{4T}$. Besides, phase detection is sensitive to noise and to suppress the noise, several Doppler measurements are usually recorded and averaged to produce reliable phase information: $\Delta\Phi(z) = \frac{1}{N} \sum_{j=1}^N \Delta\Phi_j(z)$, where N is the number of measurements. When the velocity approaches the $\pm v_{max}$, then $\Delta\phi_j \approx \pm\pi$. However in practice due to noise in the measurements some of $\Delta\Phi_j$ s might wrap around to $\mp\pi$. Therefore, the average of phase change approaches zero. In 2008, Szkulmowska *et al.* (84) suggested to calculate the phase of averaged phasors instead of directly averaging the phase components: $\Delta\Phi(z) = \text{arg}(\sum_{j=1}^N e^{i\Delta\Phi_j(z)})$ to solve this problem, where $i = \sqrt{-1}$.

Although Doppler measurements can accurately estimate the phase shift introduced by a moving particle, in practice because of background produced by the back reflected light beam from different surfaces in the OCT system, and/or the fact that in some voxels there is a mix of moving and non-moving particles, this estimation is not accurate. In 2006, Ren *et al.* (85) have introduced moving-scatterer-sensitive optical Doppler tomography (MSS-ODT) to increase the sensitivity of phase measurements by removing the interference introduced by the stationary tissue. To remove the reflection from the static tissue, first they calculated the difference between consecutive A-scans to remove the constant part, and then they measured the phase difference between the A-scans. Although in their method they were able to see some small vessels not possible to see in the phase resolved method, the problem with this method is that the subtraction cannot remove all the background and static tissue since the recordings are not exactly from the same position due to bulk motion in the tissue and galvo jitter. Therefore, this method is not sensitive enough to detect some capillaries.

In 2009, Wang and An (45) introduced Doppler optical micro-angiography (DOMAG) technique in which they densely sampled the tissue with the OCT such that about 90% of

consecutive A-scans overlapped. Afterward, they high-pass filtered the complex depth profile along the transverse direction. Before applying the PR-DOT to obtain the velocity, they added a constant value at each depth to suppress the noise for positions where the high-pass OCT signal was almost zero. They showed that their method is more sensitive than PR-DOT and can provide accurate velocity measurements.

In another approach by Szkulmowski *et al.* in 2008 (44), to improve the sensitivity of the Doppler measurements, they introduced the joint Spectral- and Time- domain Optical Coherence Tomography (joint STdOCT) which uses frequency analysis instead of phase estimation to find the the velocity. In Joint STdOCT, we scan sample densely and assume the A-scans have sufficient overlap such that up to 7 consecutive A-scans are approximately recorded from the same position. After the necessary processing to extract the complex depth profile (such as background removal, resampling, and applying FFT), we use FFT along the lateral direction to estimate the spectrum of the complex OCT signal at each depth. Then, we find the frequency that carries the maximum intensity as the Doppler frequency shift. Later in 2013, Chan *et al.* (86) proved that this method is actually a maximum likelihood estimator (MLE) of the Doppler frequency shift under the assumption of additive white Gaussian (AWG) noise. However, based on our experiments the MLE estimator is unreliable at low SNR. Furthermore, the noise is not necessarily AWG. For example, motion caused by heart beat or galvanometer jitter can not be modeled as an AWG noise and will introduce bias in the results. In addition, for such a small number of samples usually available in Doppler measurements, the MLE performance is not optimal which is in agreement with the high noise we observe in the results.

Doppler measurement can estimate the bi-directional velocity (82), but it has a fundamental drawback. Doppler measurement only estimates the axial velocity because Doppler frequency shift is only sensitive to the axial movement. Therefore, in situations where the angle between the light beam and the flow is unknown, it is not possible to estimate the absolute velocity. In many experiments the flow direction is perpendicular to the light beam which

means the axial velocity is very small and is not detectable due to noise. To overcome this fundamental problem, two different approaches were proposed in 2010 and 2012 which use autocorrelation function of scattered light to detect the transversal velocity. Wang *et al.* used the fact that autocorrelation of the complex OCT signal recorded at depth z vanishes after a time lag of τ_0 where τ_0 is the time it takes for a particle to pass across the beam waist (87). With this method, it is possible to measure the transverse velocity when the axial velocity is small enough to not disturb the autocorrelation function. In 2012, Lee and his colleagues were able to employ the dynamic light scattering (DLS) model to formulate the OCT signal back-scattered from a tissue sample (88). With this model, they were able to measure transversal and axial velocity as well as the diffusion coefficient of the blood perfusion (88), (89). Although with the DLS-OCT model they measured velocity regardless of its direction, the method has two limitations: first of all in this method there is ambiguity regarding the direction. In other words, the method can not detect the direction of the flow, while the Doppler method can distinguish whether the particles are moving toward or away from the light source. The other limitation is related to the number of scans. To use the DLS-OCT model in (88) they recorded 100 A-scans per position; therefore, to cover a complete 3D volume, this algorithm is time consuming which makes it impractical in some *in-vivo* experiments. A similar method was also proposed in (90) which requires 100 recordings from each position to provide the velocity profile estimation.

Another approach to measure velocity in capillaries was proposed in (91) which estimates the velocity by measuring the time it takes for a red blood cell (RBC) to pass across the focal spot of the light beam. To achieve this goal, it is assumed that at any moment one RBC passes across the monitored position and this RBC increases the intensity of the OCT signal. Then, the motion of this RBC produces a Gaussian like intensity profile over time at the capillary position. The width (variance) of a Gaussian function fitted to the data is used to determine the velocity. This method, similar to the previous ones, needs many recordings to estimate the velocity. It is also assumed that only one RBC is passing at any moment

and the axial and lateral sizes of the OCT voxels are the same.

Generally, the methods that estimate blood velocity based on Doppler effect do not require as many recordings as other methods and can provide better temporal resolution. However, their measurements are limited to the velocity along the axial direction. Among different variation of Doppler-based velocimetry techniques, Joint STdOCT provides better sensitivity for velocity measurement. We have adopted a similar technique to measure blood velocity in our experiments, which is covered in the next chapter.

2.4.2 Angiography

OCT angiography is an emerging field in which we locate vessels by detecting changes in the scattering parameters of the tissue caused by moving particles. By assuming that the main portion of moving scatterers are red blood cells and these particles are submerged in blood, it is possible to use OCT angiography to detect blood vessels. One of the first time domain-OCT angiography techniques was proposed by Zhao and colleagues in 2000 (33) in which the variance of Doppler phase shift was used as an indicator of movement in a voxel. Later in (92), (35), (93) and (94) similar technique was adapted to visualize vessels. This method provides higher contrast compared to the Doppler method and they were able to see more vessels. This method is not able to detect the vessels the phase change is constant. Actually, the method detects the variance of changes in the phase. Therefore, if the variance of changes is close to zero (constant change in the phase) then it would not be able to detect it.

In addition to the phase variance, the intensity variance method (95), (36), (96), (97) have been used to obtain motion contrast images as well. In intensity variance method, as is clear from the naming, moving particles are detected by measuring changes in the intensity of each pixel over a certain time interval.

In a separate research, Wang *et al.* introduced optical micro-angiography (OMAG) (37), (98). In this method, they invented a moving reference mirror to produce a modulation frequency.

This modulation enabled them to use Hilbert transform and detect pixels that have a Doppler frequency shift larger than the modulation frequency. The underlying assumption of this method is that the tissue is densely sampled such that the change in the complex-valued OCT signal between adjacent pixels is mostly due to particles movements. Although this method is able to detect some vessels there are three drawbacks: first, the method depends on the Doppler frequency shift which means the flow orthogonal to the light beam can not be detected. Secondly, it is not very sensitive and can not detect slowly moving red blood cells in capillaries. The third drawback is related to the moving mirror which adds to the alignment and synchronization difficulties specially in high speed OCT systems. The technique of densely sampling the tissue and using high frequency fluctuations along the lateral direction due to particles motion was also used in (99) to visualize vessels.

A simple, yet effective, OCT angiography technique was proposed by Srinivasan (100) in 2010. This technique, known as phase sensitive OCT angiography, finds the amplitude of changes in the complex-valued OCT signal obtained from two different recordings at the same position: $|\Delta A_n| = |A_{corrected,2n} - A_{2n-1}|$, where A_{2n-1} and A_{2n} are two B-scans recorded from the n th cross section of tissue and corrected which means the phase shift introduced by the bulk motion of the sample is compensated. To further reduce the motion artifacts they repeated the recording 5 times and averaged the angiography results. This method is sensitive to both intensity and phase changes in the OCT signal produced by moving particles.

Correlation mapping optical coherence tomography is another approach which measures the change in the correlation of a pixel with its neighborhood over time (101), (102). The low spatial resolution is one of main drawbacks of this method.

Phase-sensitive angiography has been one of the most successful angiography techniques that has been developed for SD-OCT imaging. This method is sufficiently sensitive to detect motion of RBC's in capillaries while the recording time processing load is relatively low. We developed a similar technique to the method proposed in (100) to detect the vessels in the rodent's brain. Details of our algorithm is discussed in the next chapter.

Chapter 3

Optogenetic SD-OCT system

3.1 Introduction

We designed and implemented a custom-made system which provided us with sufficient flexibility to integrate optical coherence tomography, fluorescence imaging modality, and optogenetic technology in a single unit. This system development included some optical design, machinery of custom parts, and software development. The first design aim was to enable OCT functional imaging (Doppler OCT velocity measurement and OCT angiography), and achieving near real time flow measurement in desired vessels in small rodents. Axial and lateral imaging resolution in the range of $\sim 5\mu m$ was sufficient for this goal. The second design aim was to offering proper intermediary optics to integrate OCT with other imaging methodologies.

In this section we discuss the details of a SD-OCT system that we implemented for brain imaging applications and provide practical tips on implementation process. We also evaluate the practical performance of the system and compare it with the design goals. At the end we present some in vivo results that demonstrate the ability of this system for velocity measurement or angiography. With slight modifications the same design can be used for other applications that may require a different resolution, imaging depth or light spectrum.

3.2 Light Source

To image up to several hundred micrometers deep inside a scattering medium, such as brain, with axial and lateral resolutions of $\sim 5\mu m$ or better, a light source with long central wave-

length is preferred. According to Eq. 2.7, the axial resolution of a SD-OCT system is linearly proportional to the central wavelength of the light source and inversely proportional to its spectral bandwidth. To achieve a balance between the penetration depth and resolution a light source with central wavelength of $1300nm$ and FWHM bandwidth of $> 170nm$ (LS2000B, THORLABS, NJ, USA) is used. With this light source the theoretical axial resolution is about $4.4\mu m$ in air which meets our requirement.

Since the infrared light is not visible to the human eye, for the alignment purposes an aiming red laser is utilized in this design. The beam of this laser is coupled to the infra-red fiber path via a fiber coupler. The same fiber coupler splits the OCT light beam between the reference and sample arms.

3.3 Sample arm

Our goal was to obtain a lateral resolution of $5\mu m$, and, accordingly, selected an OCT objective lens (LSM02, THORLABS, NJ, USA) with an effective focal length of $18mm$. In combination with an incident beam diameter of $3.4mm$ this lens provides a theoretical FWHM spot size of $\sim 5.2\mu m$. The collimated beam was produced by connecting a single mode optical fiber to a collimating package with the effective focal length of $18.86mm$ (F280APC-C, Thorlabs, NJ, USA).

Our sample arm uses a set of galvanometric mirrors (GMs) to raster scan the tissue. The GMs are designed for beam diameters smaller than $5mm$ (GVSM002, THORLABS, NJ, USA). The geometrical middle point between the mirrors should be positioned at the back-focal plane of the objective lens (OL). In this OL, as in most objective lens compounds, the back-focal plane is very close to the objective which makes it challenging to place the mirrors at the designated positions. We installed the mirrors on a costume-made holder (Figure 3.6), and then used a scan lens and tube lens mechanism to image the mirrors to

the back-focal plane of the objective. Moreover, for combining the optical paths of OCT and fluoresce imaging or optogenetic stimulation a dichroic mirror should be installed between the scanning mirrors and the objective, which is not possible without this auxiliary optics.

3.3.1 Scan-lens and tube-lens mechanisms

Figure 3.1 demonstrates such scan/tube lens mechanism placed before an objective lens so that a dichroic mirror can be integrated in the optical path. Imperfections in this lens system introduce optical aberrations which affect the OCT resolution. Chromatic aberrations (longitudinal and lateral) in a lens prevent different wavelengths to focus at the same focal point. Equally important, astigmatism causes sagittal and tangential light rays to focus at different axial positions. These imperfections increase the focal spot size of the lens system and therefore degrade the resolution of an OCT scanner. Moreover, in the presence of a large Petzval field curvature (PFC), the focal plane is not flat and OCT images do not have a uniform resolution across the transversal surface.

Here, we analyze the effect of different designs of scan-lens and tube-lens on the lateral resolution of an OCT device. First, we used Zemax optical design software to compare the performance of three popular and inexpensive lens systems, which are based on off-the-shelf components, as scan/tube lenses. In practice, we used an OCT objective lens with an effective focal length of $18mm$ (LSM02, Thorlabs, NJ, USA) in combination with a collimator lens that provides a beam waist of $3.4mm \varnothing_{\frac{1}{2}}$ at $1310nm$ (F280APC-C, Thorlabs, NJ, USA). According to the Gaussian beam propagation equation (73), the FWHM focal spot size of this combination is $\sim 5.16\mu m$ which is close to the desired resolution. We selected the simulation parameters according to the practical setup and a paraxial lens model of focal length $18mm$ was used as an objective lens for simulation purposes. With this lens, a scan angle of $\pm 6.4^\circ$ results in a scan field radius of $2mm$. Moreover, in the design process, a reciprocal structure with a $1\times$ magnification was considered for the intermediate lens

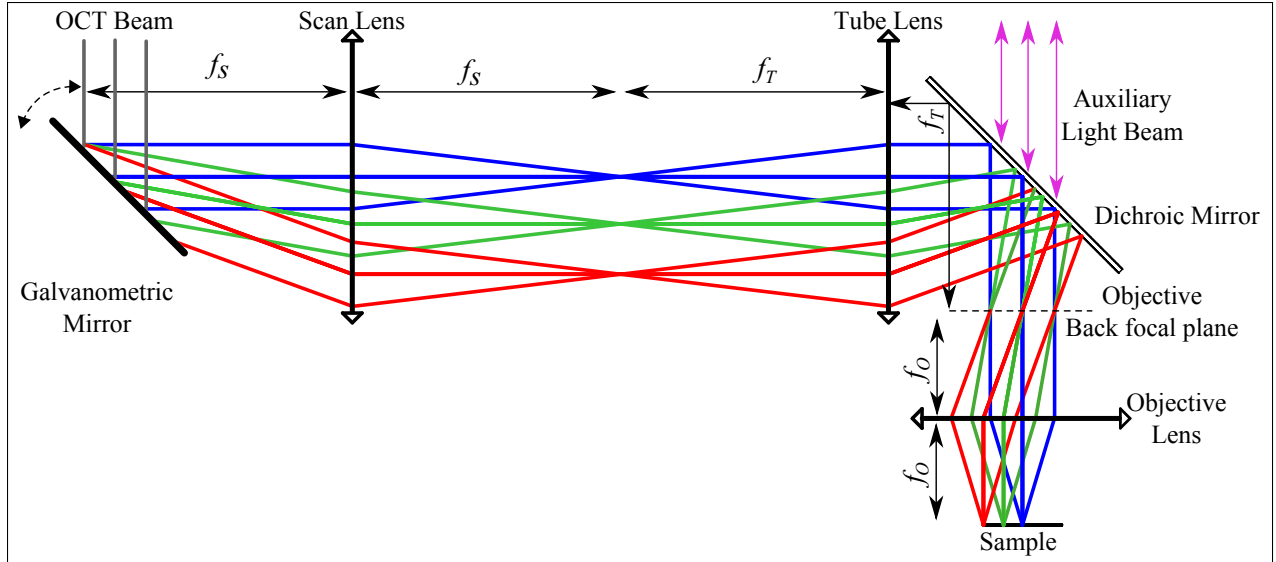


Figure 3.1: The schematic of a scan-lens and a tube-lens in an OCT optical path. A galvanometric mirror is located at the focal of the scan-lens and the scan/tube lens mechanism projects the OCT beam on the back-focal-plane of the objective lens. A dichroic mirror is added to separate the OCT beam and an auxiliary beam. An auxiliary light beam can be used for other imaging modalities or optogenetic stimulation applications. f_s , f_T , and f_o are respectively the focal lengths of the scan-lens, tube-lens and objective.

system. In our OCT, the collimating lens and objective have similar effective focal lengths and no magnification is required to achieve the desired resolution. Since the illumination and backscattered light travel via the same lens mechanism in a two-way path, a similar performance in both directions serves the purpose of this design.

Scan-lens and tube-lens simulations

During our simulations we investigated performance of three common lens designs for scan/tube lens. The first two lens systems consist of single lenses and the third lens system uses a four element lens mechanism (similar to Plössl compound) for scan-lens and tube-lens. The same lens structure was used for both scan-lens and tube-lens to achieve reciprocal performance.

Biconvex Singlet Lenses The simplest relay lens system would be two lenses that are placed in a $4f$ configuration. Since OCT light sources are wide-band (typical bandwidth of $\sim 100nm$ or larger) it is necessary to use lenses that are properly designed for such a

wide spectrum. Calcium-Fluoride (CaF₂) has low dispersion in the near infrared spectrum. Consequently, lenses that are made from CaF₂ generally introduce low chromatic aberration over a wide bandwidth at the center wavelength of 1300nm. In our first design, we used biconvex CaF₂ lenses of focal length 50mm (LB5284, Thorlabs, NJ, USA) as the scan/tube lens. Simulations show a severe astigmatic aberration for this lens which can degrade the performance of an OCT system. When the corresponding 4*f* lens system is used with the paraxial objective model at the maximum scan angle (6.4°), sagittal and tangential rays come to focus around 200μm and 590μm away from the focal plane, respectively, because of the field curvature and astigmatism aberrations. The separation between the focal of sagittal and tangential rays (> 380μm) at this scan angle is significantly larger than the Rayleigh range of the light beam (~ 46μm), and worsens the OCT resolution at the corners of the FOV. This can be confirmed by the root mean square (RMS) of the wavefront error which exceeds the diffraction limit threshold (0.072*waves*) at scan angles larger than 2.7°. Consequently, with this lens mechanism the diffraction-limited FOV is confined to an area with a diameter smaller than 1.7mm (Figure 3.2).

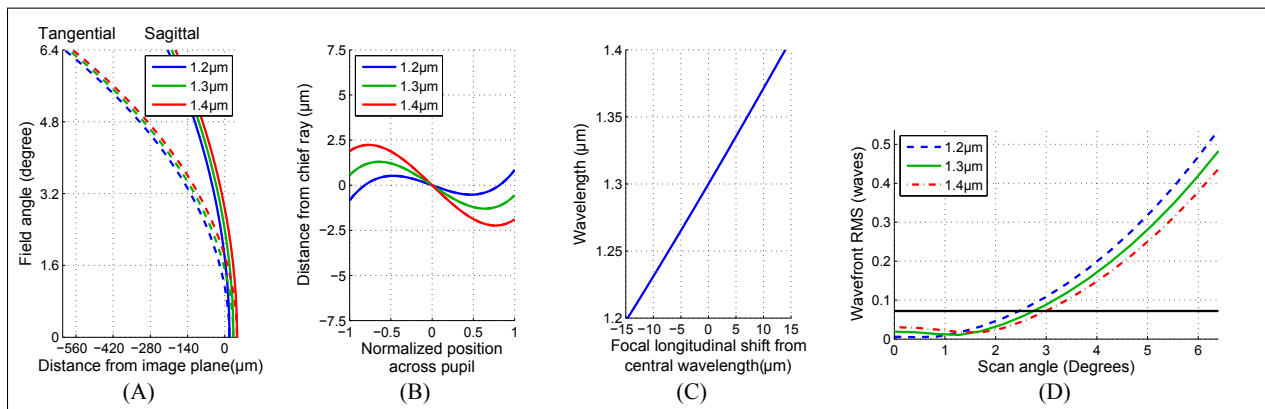


Figure 3.2: Optical aberrations when two CaF₂ lenses (LB5284, Thorlabs, NJ, USA) are used as scan and tube lenses in combination with an 18mm focal length objective lens. (A) Field curvature and astigmatic aberrations. (B) Ray aberration as a function of pupil coordinate. (C) Chromatic focal shift. (D) Wavefront RMS vs scan angle.

Achromatic doublet Achromatic doublets (AD) are designed to introduce less spherical and chromatic aberrations to an optical beam compared to singlet lenses. Therefore, the next lens we studied was an AD of focal length $\sim 50\text{mm}$ (AC254-050-C, Thorlabs, NJ, USA). With this lens we observed smaller spherical aberration than the previous lens at a similar chromatic aberration (Figure 3.3). Since these aberrations are already below the diffraction limit of our system, this improvement does not provide any superiority over the CaF2 lens. However, the AD lens introduces larger astigmatic and field curvature aberrations to the light beam compared with the CaF2 lens, which further reduces the diffraction-limited FOV compared with the previous lens system. As presented in Figure 3.3.D, when two AC254-050-Cs are employed as the scan-lens and tube-lens, the wavefront error RMS increases above the diffraction limit at scan angles $> 1.9^\circ$ and the diffraction-limited resolution is confined to a FOV of radius $\sim 1.2\text{mm}$. At the scan angle of 6.4° , the separation between tangential and sagittal focal planes is more than $800\mu\text{m}$. The focal spot size enlargement due to the severe astigmatism considerably reduces the signal to noise ratio of OCT images at large scan angles as well. Several lens providers offer various designs for AD lenses with different performance levels. Although some of the designs show moderately improved astigmatism, all models available on-line introduce large amount of astigmatism to the light beam.

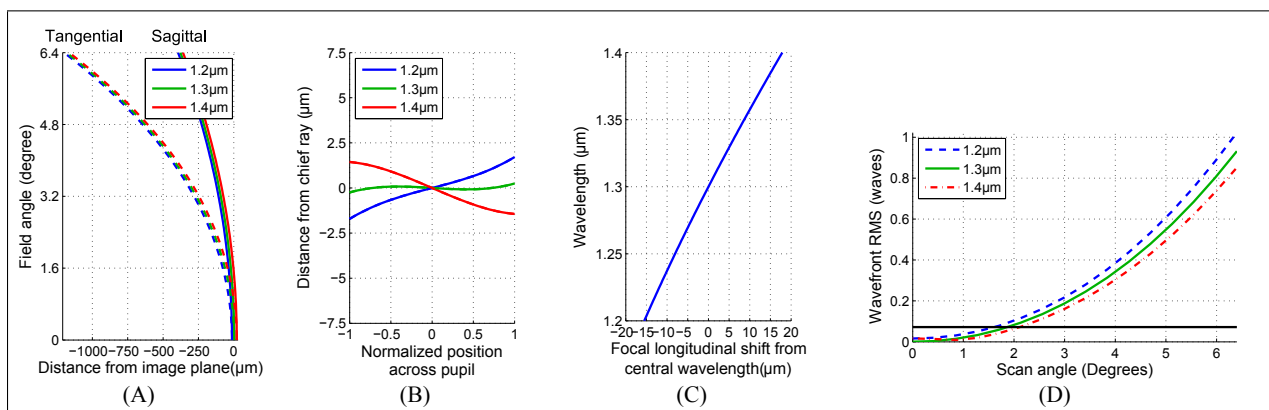


Figure 3.3: Optical aberrations when two achromatic doublet lenses (AC254-050-C, Thorlabs, NJ, USA) are used as scan and tube lenses in combination with a paraxial objective with an 18mm focal length objective lens. (A) Field curvature and astigmatic aberrations. (B) Ray aberration as a function of pupil coordinate. (C) Chromatic focal shift. (D) Wavefront RMS vs scan angle.

Four-Element semi Plössl compound A Plössl compound lens is usually used as an eyepiece and according to its good performance we considered it as a potential scan/tube lens. Generally, a Plössl compound lens consists of two identical achromatic doublets; however, by removing this constraint, we were able to test a more diverse collection of lenses. To make an asymmetric semi Plössl compound of the desired focal length (between $50mm$ and $85mm$), we used two achromatic doublets with focal lengths of $\sim 125mm$ (AC254-125-C, Thorlabs, NJ, USA) and $\sim 150mm$ (AC254-150-C, Thorlabs, NJ, USA) (Figure 3.4). The lens compound has an effective focal length of $\sim 66mm$ and its performance is summarized in Figure 3.5. This simple lens system introduces fairly small amount of aberrations and performs close to the diffraction limit at field angles smaller than 6.4° (FOV of radius $4mm$ combined with the designated objective). The field curvature and astigmatic aberrations, which were the major limiting factors in the previous lens mechanisms, are significantly reduced when using this semi Plössl compound. At the maximum scan angle, Petzval field curvature is $\sim 13\mu m$ toward the lens for sagittal rays and $\sim 44\mu m$ away from the lens for tangential rays. The curvature is negligible for many applications. Also the separation between sagittal and tangential focal planes is $58\mu m$ which is marginally larger than the Rayleigh length. However, the wavefront error RMS at this scan angle is smaller than the diffraction limit threshold and the overall lens system performs within the diffraction limit over a FOV of radius $2mm$.

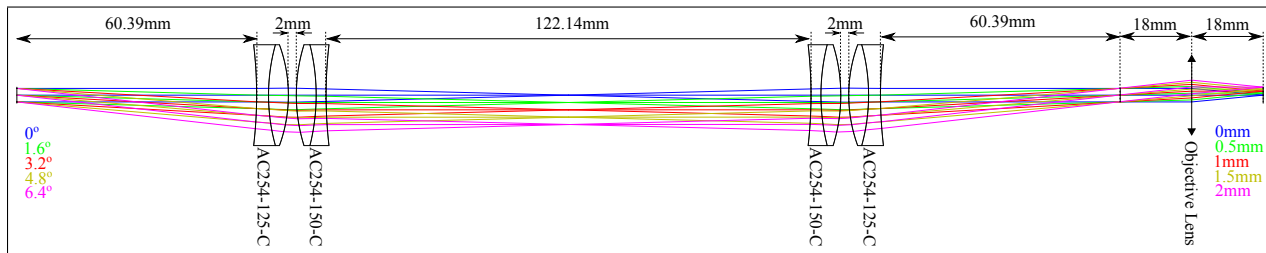


Figure 3.4: The schematic of the lens mechanism based on four element scan/tube lens. The effective focal length of the lens compound is $\sim 66mm$

At the end we selected four-element semi Plössl compound lens mechanism for final system implementation. Figure 3.6 shows the practical design of this lens mechanism in the

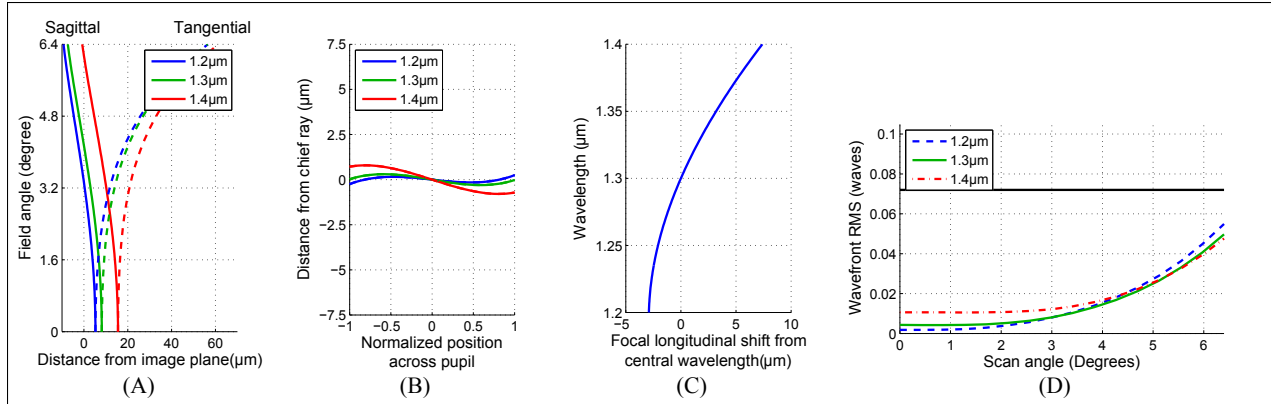


Figure 3.5: Optical aberrations when two semi Plössl compound lenses (AC254-125-C+AC254-150-C, Thorlabs, NJ, USA) are used as scan and tube lenses in combination with an 18mm focal length objective lens. (A) Field curvature and astigmatic aberrations. (B) Ray aberration as a function of pupil coordinate.(C) Chromatic focal shift. (D) Wavefront RMS vs scan angle.

OCT system.

3.3.2 Beam combination

With the use of the scan-tube lens, there is space to place a dichroic beam-splitter in the sample arm. This dichroic beam-splitter can separate OCT and visible light paths (visible port in Figure 3.6) and allow for simultaneous OCT and bright-field or fluorescence imaging. The proposed design is for a long-pass dichroic beam-splitter; however, a custom mount can be slightly modified to accommodate a short-pass dichroic instead. When using a long-pass dichroic, the OCT beam passes through the glass slap. The length that light travels via the glass varies as a function of scanning angle. This causes a spurious change in the depth of reconstructed OCT images across the transversal plane as the beam raster scans the tissue. This spurious change in the depth may appear as bias in OCT Doppler velocity measurements. A short-pass dichroic does not introduce such artifacts; however, multiple reflections from different layers of reflectors in a short-pass filter can cause strong artifacts in the OCT image that appear as replications of the original image. A short-pass dichroic should be selected carefully to avoid such artifacts. We used a long-pass beamsplitter (FF875-Di01,

Semrock Inc., NY, USA). This dichroic mirror reflects wavelengths that are shorter than 900nm . A simple design of a fluorescence/bright field imaging path is shown in Figure 3.7.

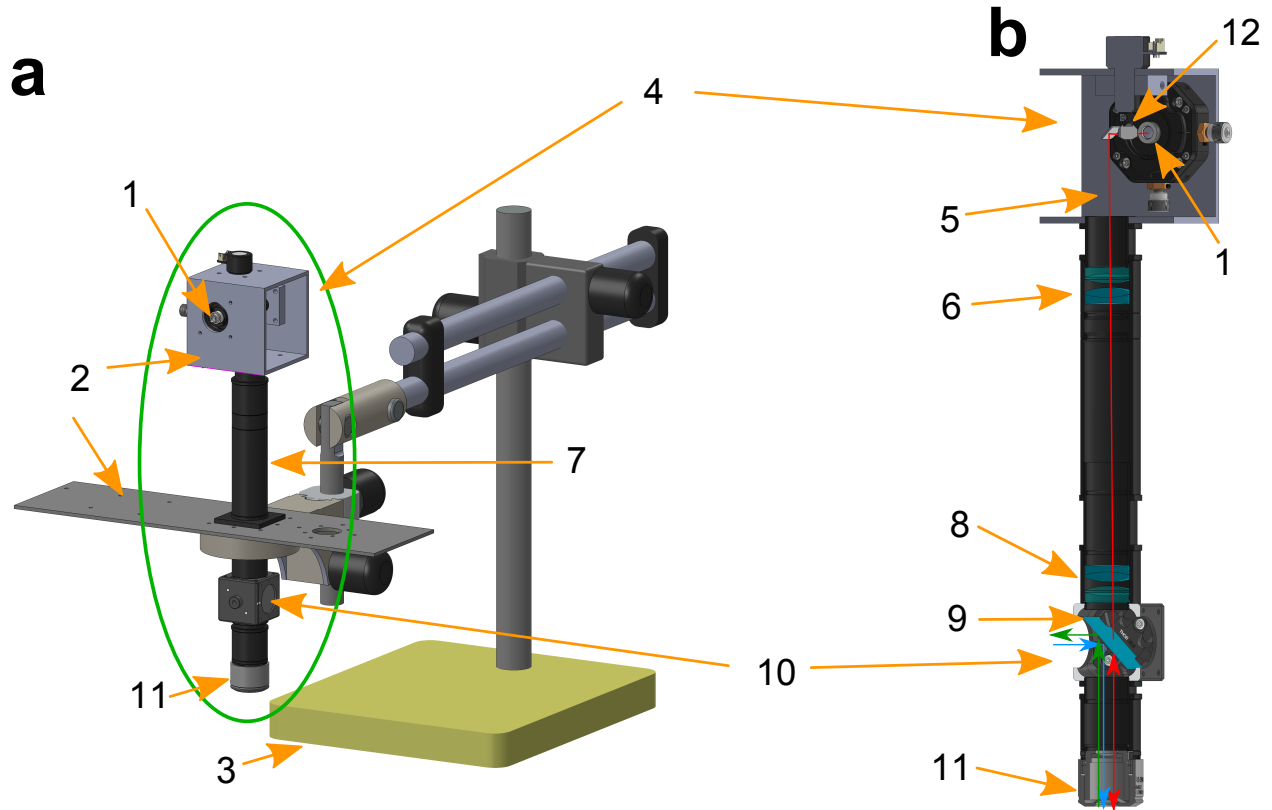


Figure 3.6: Sample arm. This image demonstrates the design of the sample arm that is mounted on a typical microscope stand. This system uses two identical semi Plössl lenses as scan and tube lenses. The cross section shows the optics including galvanometric mirrors, scan and tube lens mechanisms and the infrared dichroic mirror. 1-OCT collimator, 2-custom mounts, 3-commercial microscope stand, 4-scan head, 5-OCT beam, 6-scan lens, 7-lens tube, 8-tube lens, 9-dichroic mirror, 10-visible port, 11-objective lens, 12-galvanometric mirrors.

The sample arm and the visible path are mounted on a custom-made adapter and a typical microscope single-arm boom stand (Figure 3.8). This allows for adjustment of the OCT head angle to approach a specimen from an arbitrary angle.

3.3.3 Reference arm

Ideally, in an OCT system the reference arm should replicate the length that light travels and the dispersion that it experiences in the sample arm. If the light dispersion in the sample

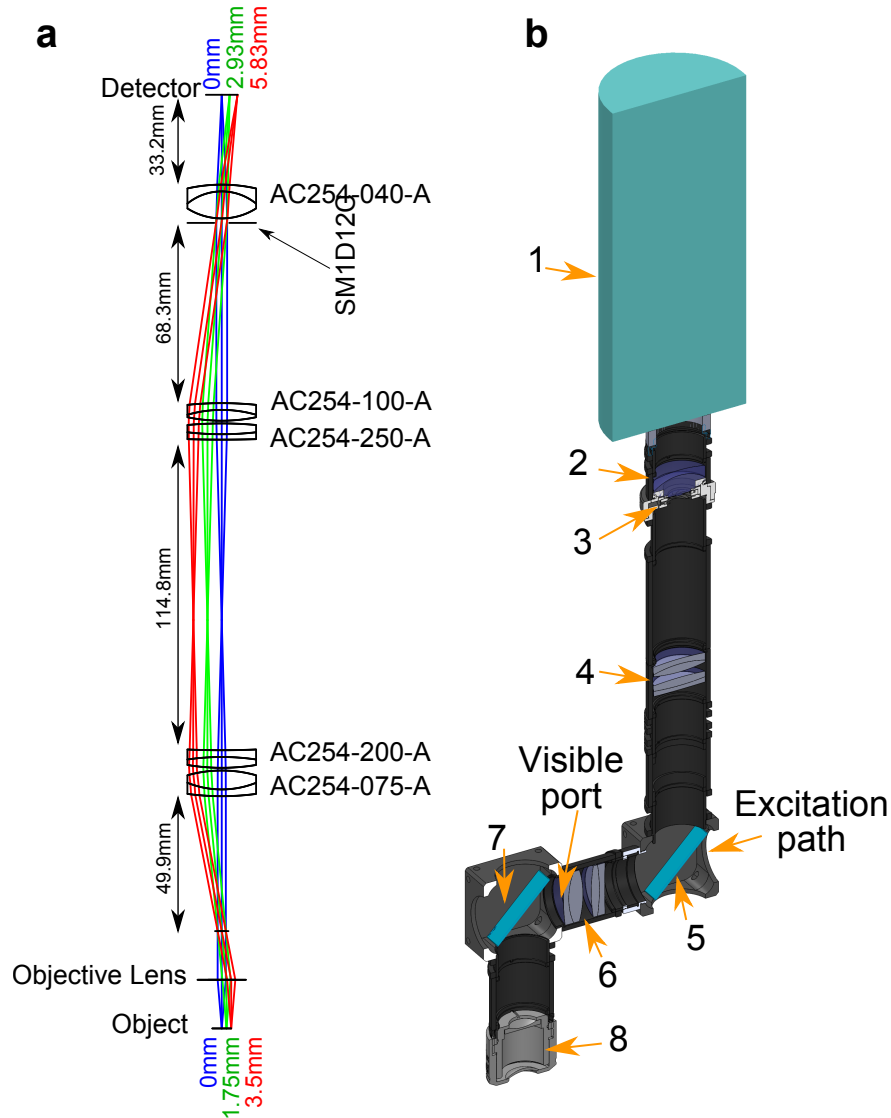


Figure 3.7: Fluorescence imaging path. a) the schematic and b) the solid work design of the fluorescence imaging path. The fluorescence imaging path uses two semi Plössl lenses to image the back focal plane of the objective to the entrance pupil of an imaging lens. There is an adjustable iris in this path to adjust the aperture diameter of the imaging system. This is helpful to reduce the aberration in the optical path and improve the imaging resolution. 1-Fluorescence camera (Exi Aqua, Qimaging, BC, Canada), 2-adjustable iris (SM1D12CZ, Thorlabs, NJ, USA), 3-imaging lens (AC254-040-A, Thorlabs, NJ, USA), 4-semi Plössl lens (AC254-100-A + AC254-250-A), 5-Visible light dichroic mirror (FF440-520-Di01, Semrock Inc., NY, USA), 6-semi Plössl lens (AC254-075-A + AC254-200-A), 7-Long-pass infrared dichroic (FF875-Di01, Semrock Inc., NY, USA)

arm is not properly replicated in the reference arm it may greatly affect the axial resolution and quality of the OCT images. To minimize the dispersion mismatch between sample and

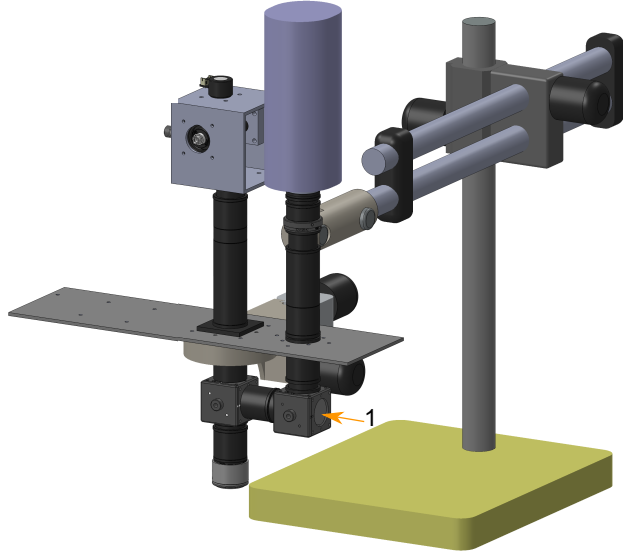


Figure 3.8: Multi-modal scanner setup. The system incorporates the visible and OCT imaging mechanisms to allow for OCT data acquisition simultaneous with optogenetic stimulation or fluorescence imaging. Port 1 is the stimulation/excitation beam path.

reference arms, we assembled the reference arm with identical components that were used in our sample arm, except the scan head and the objective lens. In reference arm we used a single glass dispersion compensator (DC) (LSM02DC, THORLABS, NJ, USA) to replicate the optical path of the beam inside the objective lens (Figure 3.9). This reduces the cost. At the end of our reference arm we use a protected gold mirror (PF10-03-M01, THORLABS, NJ, USA) to obtain a flat reflection spectrum within the wavelength range of our light source. The light power that is back reflected from a mirror is typically much stronger than the backscattered light from a tissue in the sample arm. We installed an adjustable iris in the reference arm to tune the reference power. A removable right-angle mirror is used in the reference arm to incorporate multiple optical paths in the reference arm. This is useful when more than one objective lens should be used during an experiment.

3.3.4 Spectrometer

For recording the interference patterns we used a custom-made spectrometer which consists of a transmission grating, a Plössl compound lens, and a line charge-coupled device (L-CCD).

We chose a volume phase holographic transmission grating (wasatch photonics, UT, USA) with 1145 grooves per mm to obtain a large bandwidth and a balanced performance for different light polarizations. The optimal incident and diffraction angle at $\lambda = 1.31\mu m$ for this grating are $\sim 48.6^\circ$. These requirements were accommodated by installing the grating on two rotation mounts (PRM1 and RP01, THORLABS, NJ, USA) for fine adjustment of yaw and roll angles (Figure 3.9). The beam was delivered to the spectrometer via a SMF-28e+ single mode fiber and a collimating package (F280APC-C, THORLABS, NJ, USA).

The diffracted beam is imaged on the L-CCD by two achromatic doublet lenses (AC508-150-C, THORLABS, NJ, USA) which form a Plössl compound (Figure 3.10) with an effective focal length of $\sim 72mm$. The L-CCD detector in this system (SU1024-LDH2, Sensors Unlimited, NJ, USA) has 1024 pixels with a $25\mu m$ pixel pitch and aperture height of $500\mu m$. The length of the focal plane array in this camera is $25.6mm$ which is sufficient to receive at least $200nm$ of the spectrum ($1200nm$ to $1400nm$) in combination with our lensing mechanism. For an incident beam diameter of $3.4mm$, this lens compound forms a theoretical FWHM spot size of $\sim 20\mu m$ which is smaller than the camera pixel pitch. Optical aberrations that are introduced by this lens system are sufficiently small (Figure 3.10.b, c) and the root-mean-square wavefront error stays below the diffraction limit at different diffraction angles (Figure 3.10.d). The small spot size reduces the sensitivity roll-off by reducing the spread of each wavelength over multiple pixels.

3.3.5 Fiber-based components

The light source was directly connected to a fiber optic circulator (CIR-1310-50-APC, THORLABS, NJ, USA). The circulator illuminates a 50/50 fiber coupler (FC1310-70-50-APC, THORLABS, NJ, USA) which splits the OCT beam between the sample and reference arms via two single mode fibers with APC cut (P3-980A-FC-2, THORLABS, NJ, USA). The backscattered or back-reflected light for the sample and reference arms are recombined by

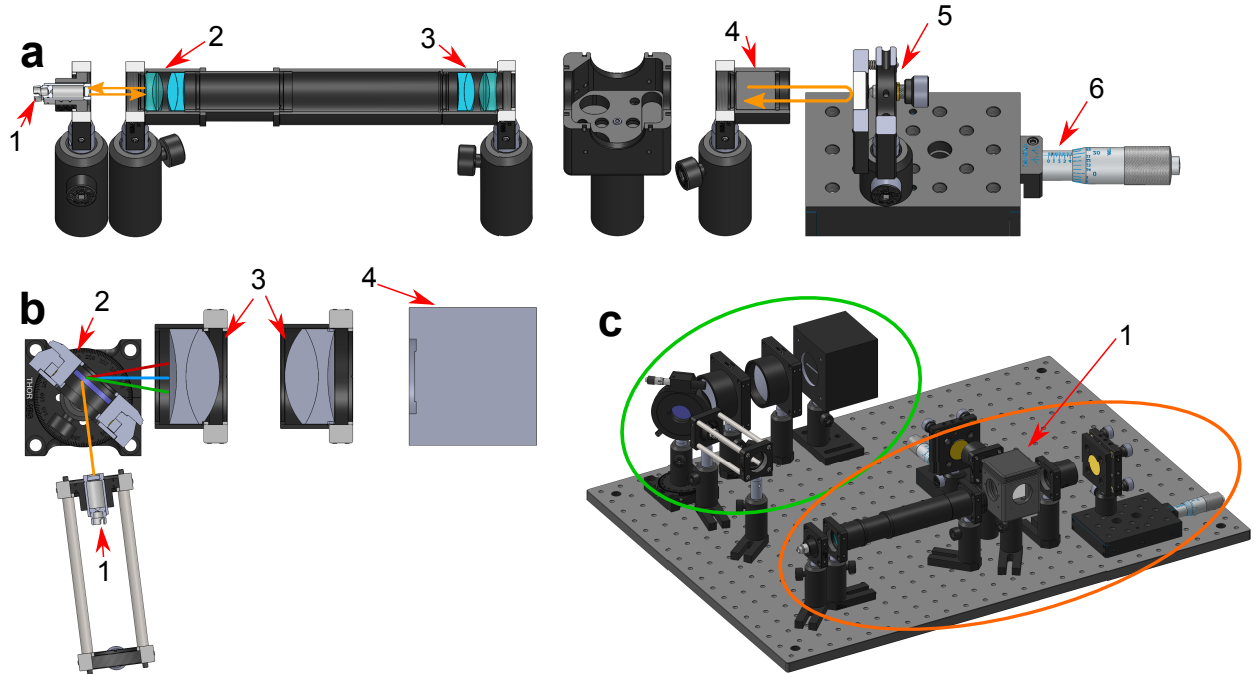


Figure 3.9: (a) The solidwork design of the reference arm. 1- fiber connector, 2-scan lens, 3-tube lens, 4-dispersion compensator for the objective. 5- a gold mirror installed on a kinematic mount with adjustable angles. 6-translational stage to precisely control the position of the reference mirror. (b) The solidwork design of spectrometer arm. The grating has an optimal incident angle of 48.6° , diffracted angle of 48.6° . It is mounted on rotatory mounts to adjust the angles of the grating with respect to the OCT beam and the lens mechanism. 1-fiber connection, 2-Grating installed on rotatory mounts. 3-Plössl lens, 4- line CCD camera. (c) the reference and spectrometer arms are installed on an optical bread board to facilitate transportation. There is a movable mirror mount (1) in the reference arm that can change the beam path to match different objective lenses in the sample arm. The reference and spectrometer arms are encircled with the orange and green outlines, respectively.

the fiber coupler and guided toward the spectrometer arm via the fiber circulator. The fiber coupler possesses two input ports, where one is used for OCT beam and the other port is connected to a red light source. The red light is used for alignment purposes and guiding the operator to the region of interest at the time of imaging.

3.4 Experimental Results

We measured the point spread function and resolution of the proposed OCT system by using a custom-made gold nanoshell embedded 3D phantom. The effect of two different in-

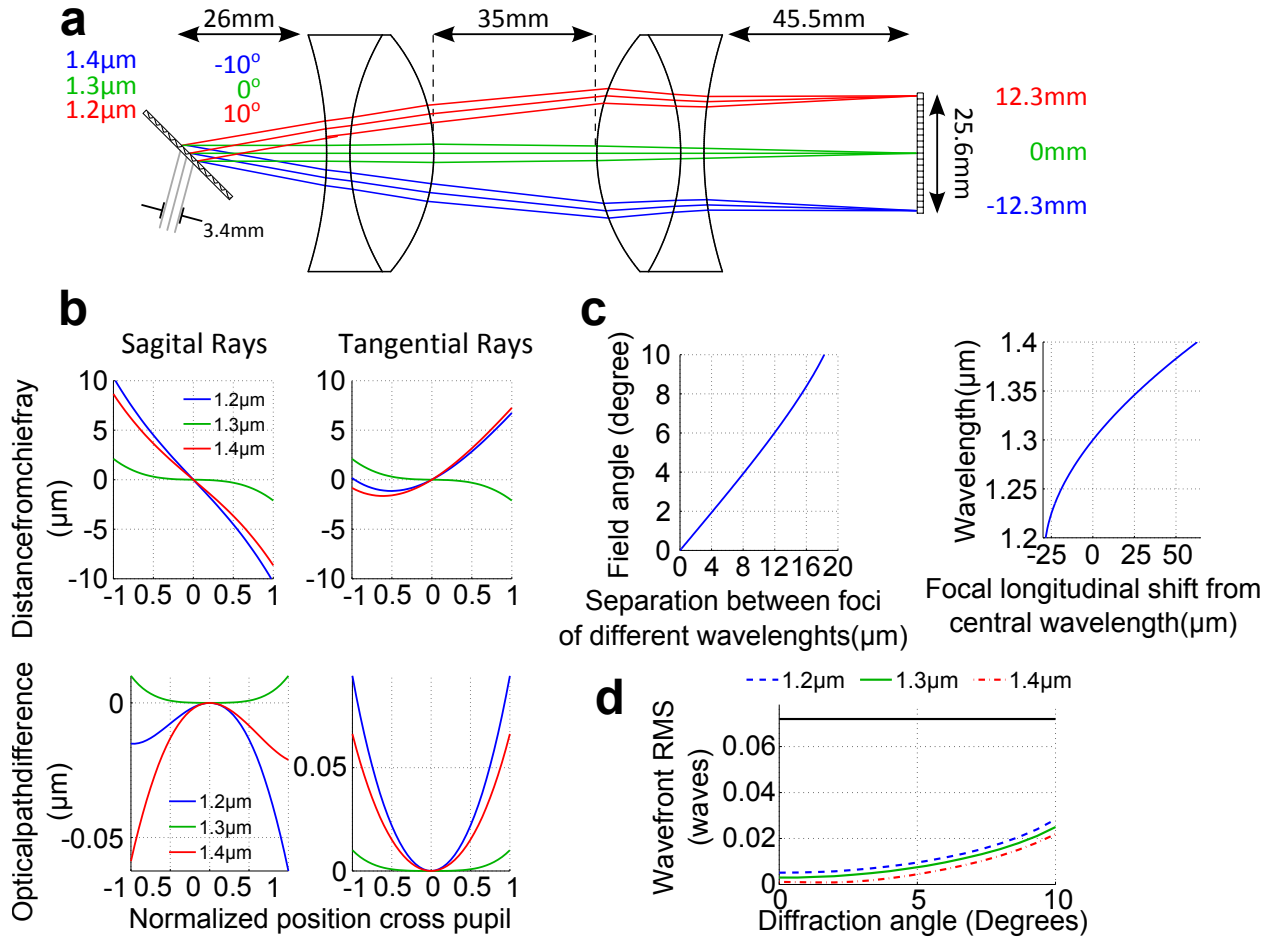


Figure 3.10: A schematic of the spectrometer. The grating diffracts the broadband collimated beam. The lens system acts as a scan lens and focuses the diffracted light beams on the focal plane array of a line scan camera. The focal length of the lens mechanism is designed such that the desired spectrum (1200nm to 1400nm) is covering the extent of the detector array. Optical aberrations in this scan lens system is low which reduces the sensitivity roll-off of the OCT images.

termediary scan/tube lens mechanisms was analyzed and compared with our Zemax software simulation results. The scan/tube lens mechanisms were assembled using achromatic doublets or semi Plössl lenses and the PSFs of the corresponding OCT systems were obtained. The FWHM values of the PSFs are reported as a resolution for the OCT system to compare the performance of different relay lens mechanisms.

3.4.1 Sample Preparation.

In recent years, several groups have attempted to measure the PSF of OCT systems (103; 104; 105; 106) by fabricating 3D phantoms with embedded sub-resolution particles. We prepared a 3D sample following a procedure similar to what was described in (103). To make our sample, we desiccated a $130\mu L$ suspension of gold nano-shells. The nano-shells consist of a silica core of radius $\sim 99nm$ and a gold shell of $16.4nm \pm 5.9nm$ thickness (980 nm Resonant Gold Nanoshells, nanoComposix, CA, USA). Then, nano-shells were dispersed in $20mL$ of epoxy resin (EpoxiCure Epoxy Resin, 20-8130-128, Buehler, IL, USA) using an ultrasonic bath. At the end, $5mL$ of an epoxy hardener (EpoxiCure Epoxy Hardener, 20-8132-032, Buehler, IL, USA) was slowly added and mixed with the resin mixture and allowed to harden for approximately 12 hours. The spacing between the gold nano-shells was estimated to be $\sim 50\mu m$. Since the particles were selected to be significantly smaller than the theoretical PSF of our imaging system ($0.22\mu m$ compared to $5.16\mu m$), the image formed by each particle is representing the PSF of our imaging system.

3.4.2 Point Spread Function Measurement

The prepared 3D sample was scanned by the custom-made OCT system. The scan parameters were set to cover a sub-area of $400\mu m \times 400\mu m$ on the phantom with $0.5\mu m$ spacing between axial scans (A-scans). 800 axial scans were recorded along the fast galvanometric mirror axis at the speed of 20,000 A-scans per second to form a B-scan. For each cross section, 10 B-scans were recorded and averaged to reduce noise and then the slow moving mirror was moved to the new cross section. This process was repeated for 800 different cross sections. The data was further processed to detect and extract transversal images of gold nano-shells which represent the lateral PSF of the imaging system at that sub-area. The FWHM of each PSF at the focal plane of the objective was measured and averaged to obtain the FWHM of the imaging system at that sub-area. To calculate the FWHM of a PSF, first a 2D Gaussian function was fitted (107) to the particle image and then FWHM along the fast

(F) and slow (S) mirror directions were calculated by $\text{FWHM}_{F/S} = 2\sqrt{2\ln(2)}\sigma_{F/S}$ where σ_F and σ_S are the standard deviations of the fitted 2D Gaussian function along the fast and slow mirror axes, respectively (Figure 3.11). This procedure was repeated at different sub-areas across the entire FOV to obtain a map of the imaging resolution.

Effect of scan lens and tube lens mechanisms

Figure 3.12 presents the measured FWHM at different areas of the field of view when achromatic doublets or four-element semi Plössl lenses were used as the scan-lens and tube-lens. For the first lens mechanism a $4\text{mm} \times 4\text{mm}$ area was scanned; however, due to the large PSF size and low signal to noise ratio at the borders of the FOV, the resolution measurements were performed only at the central $2\text{mm} \times 2\text{mm}$ area. With this lens mechanism at 1mm away from the optical axis, the FWHM increased to $\sim 8\mu\text{m}$ and $\sim 10\mu\text{m}$ along the fast and slow axes, respectively. Therefore, the maximum FOV with close to the diffraction-limited resolution that our OCT system could achieve with this lens systems was $\sim 2\text{mm}$ in diameter. Another important imperfection caused by the first relay lens was the large field curvature. Because of astigmatism, the curvature was different for tangential and sagittal rays. Tangential focal curvature can be observed in a cross-sectional image captured from the 3D phantom (Figure 3.13), in which the out of focus particles become larger and their intensity drops. For the lens system that consists of four-element semi Plössl compounds, the resolution is $5.6\mu\text{m}$ and $6.4\mu\text{m}$ at the center of FOV along the fast and slow axes, respectively, and remains fairly uniform across most of the FOV. At scan angles larger than 6.4° , the FWHM increases above $7\mu\text{m}$ along both axes, possibly due to aberrations or beam cut at the edge of lenses.

Depth dependent PSF

We also measured the change in the shape of the PSF as a function of depth when we placed the focal plane of OCT at $\sim 390\mu\text{m}$ below the surface of the phantom. At the focal plane, we

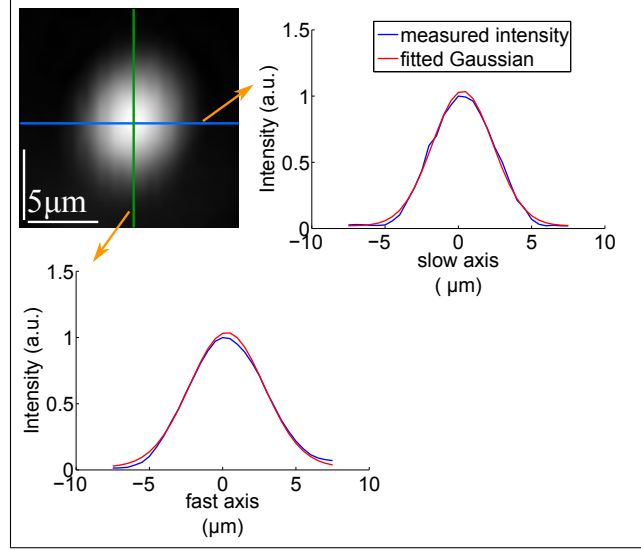


Figure 3.11: A typical lateral PSF measured for semi Plössl relay lens system. A 2D Gaussian function is fitted to the PSF to measure the FWHM along the fast and slow scan mirror axes. Cross-sectional profile of the PSF and the fitted Gaussian function are plotted for each of the fast and slow axis directions.

observed a quasi-Gaussian PSF. At deeper regions the spread of the Gaussian increases and its intensity drops. At regions above the focal plane we see that the spot size shrinks while a ring starts to form around it. This ring is visible for particles that are located $\sim 100\mu m$ above the focal plane. At shallower regions ($-120\mu m$ above the focal) the ring becomes almost as intense as the central spot. We conducted a similar measurements when we modified the design of our sample arm to place the objective lens directly after the scanning mirrors and removed the intermediary optics. Our measurements (not included in here) revealed a similar ring pattern at shallow regions of the OCT images. This measurement confirmed that the designed scan/tube lens mechanism does not considerably contribute to the formation of the surrounding rings in the OCT PSF. We anticipate the combination of spherical aberrations in the objective and collimating package and beam-cut at the collimating packages can result in the ring formation in the PSF of this OCT system.

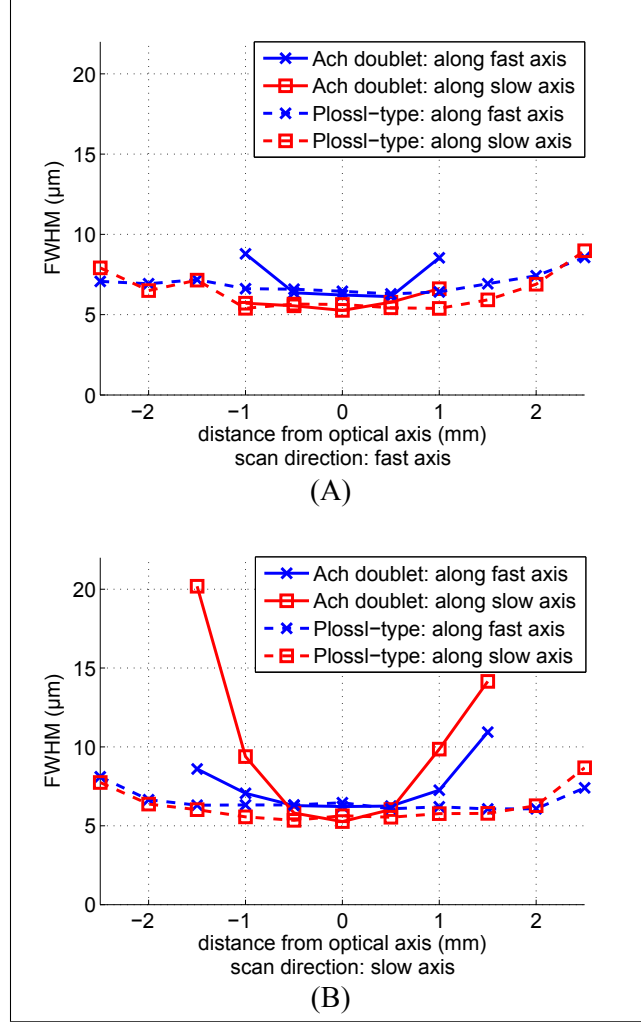


Figure 3.12: FWHM of the PSF of the OCT system in the transversal plane at different positions along the fast mirror axis (A) and the slow mirror axis (B). FWHM of the lateral PSF of the OCT system with the semi Plössl lens mechanism remains below $8\mu\text{m}$ for positions up to 2mm away from the center of field of view. For the single achromatic doublet lens at the 1mm distance from the optical axis FWHM exceeds $8\mu\text{m}$

3.4.3 Axial resolution measurements

In practice by placing a gold mirror (PF10-03-M01, THORLABS, NJ, USA) in the sample arm we measured the axial resolution of this device. The FWHM of the recorded A-scans where $\sim 5.6\mu\text{m}$ (Figure 3.15). The measured FWHM is slightly larger than the theoretical resolution. The imperfections in the components and optical aberrations in lensing mechanisms can contribute to degradation of axial resolution. The non-Gaussian distribution of

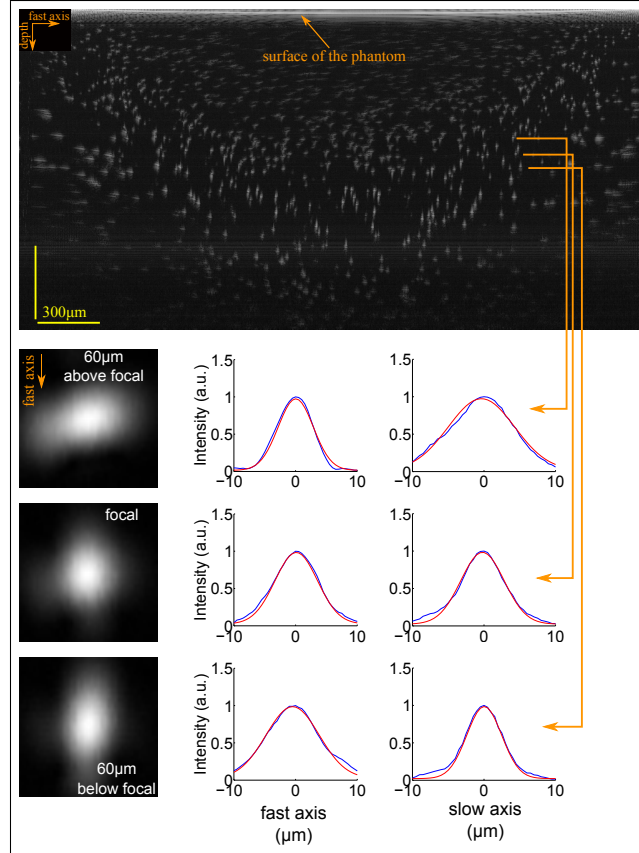


Figure 3.13: Top: A 2D cross-sectional image taken when two achromatic doublets were used as the scan-lens and tube-lens. To be able to see out of focus particles a logarithmic scaling is used which compresses the dynamic range of the image intensity. The out of focus nanoshell gold particles have much smaller intensity and the corresponding PSF is spread over a larger area compared to the particles in the focal of the objective lens. The field curvature is considerable and at the sides of the image the focal approaches toward the surface. Typical lateral PSF measurements at 1mm from the center of FOV are shown at the lower panel. Due to astigmatism PSF's are not similar above and below the focal surface. The arrows are just for illustrative purposes and are not showing the exact location of PSF measurements since they were obtained from a different recording.

the source power is another important factor that can negatively affect the resolution.

3.4.4 Intensity change across the field of view

The intensity change in the OCT images across the field of view was measured by using a 3D phantom with embedded sub-resolution gold nanoshells. At each desired location in the field of view a $400\mu\text{m} \times 400\mu\text{m}$ block of the phantom was imaged and the average intensity

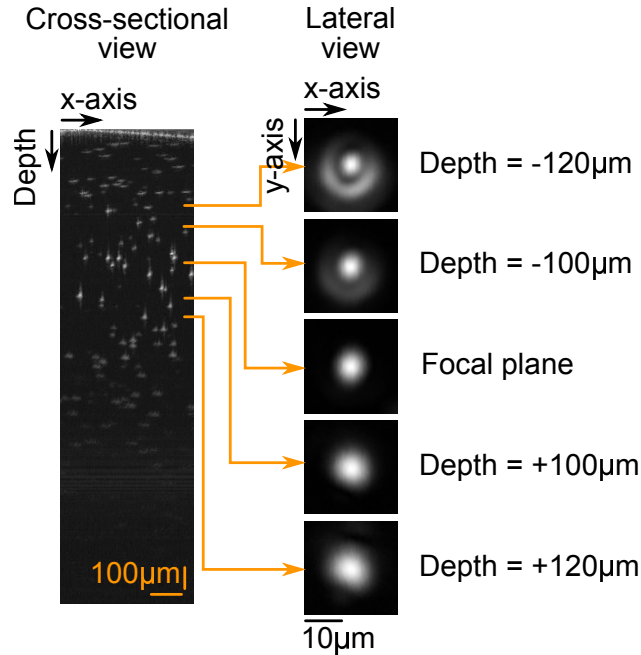


Figure 3.14: the lateral point spread function of the proposed OCT system at different depths. These measurements are conducted when the focal plane of the OCT was placed $350\mu\text{m}$ below the surface of a 3D phantom with embedded gold nanoshells. At regions above the focal plane we observed a ring surrounding the central spot in the lateral PSF.

of the detected nanoshells at the focal plane of the system was calculated. This calculation was repeated at different locations across the field of view and the results are presented in Figure 3.16. The system is able to provide almost a flat intensity (less than 2dB drop in the intensity) for a field of view of up to 4mm in diameter. However, when approaching the boundary of diffraction limited field of view ($\sim 4.7\text{mm}$) the intensity declines noticeably. A combination of beam truncation and different optical aberrations can result in such an intensity drop in the imaging system.

3.4.5 Fluorescence imaging

The visible path in this system can be used for bright field or fluorescence imaging. In some experiments we use this capacity to image the vascular network and guide the OCT scanner to target a region of interest. An example of such image is shown in Figure 3.17. The same system was used for calcium imaging to detect brain neuronal activity. In calcium imaging

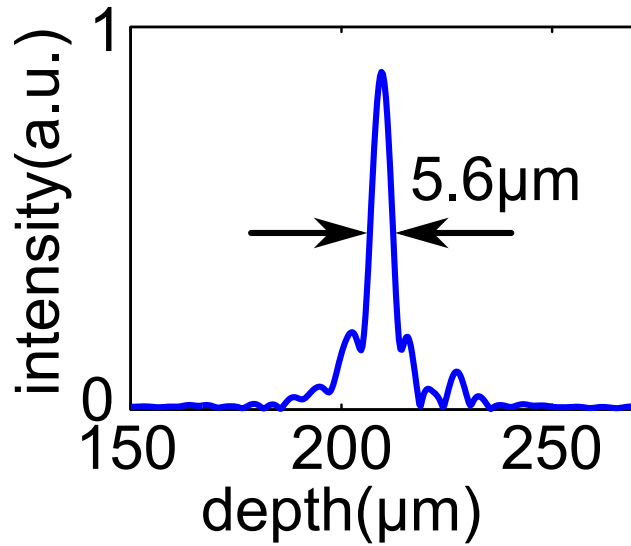


Figure 3.15: Axial resolution of the implemented SD-OCT system.

a calcium indicator is introduced to the neuronal cell to allow for detection of neuronal activity by analyzing fluorescence images. Calcium indicators are fluorescent proteins which their fluorescence properties changes as they bind to a calcium ion. Cellular activity results in an increase in the intra cellular concentration of the calcium ions, which consequently, increases the concentration of calcium indicators that are bound with calcium ions. This increase in the concentration bound indicators can be detected as a change in the fluorescence light emitted from the tissue or cell. Here we used calcium imaging capacity of our device to detect neuronal activity in the brain following a direct brain electrical stimulation via graphene-based, carbon-layered electrode array (CLEAR) devices (108) and (109). Figure 3.18, demonstrate the detected change in the fluorescence light of GCaMP6f (110) at different time points following delivery of stimulation pulses at $150Hz$ for a period of $600ms$. The amplitude of the stimulation varied between $50\mu A$ to $150\mu A$. As the stimulation intensity increases, the amplitude of the fluorescence signal increases. The CLEAR device can not be seen in the images as it is transparent in the wavelength range from ultraviolet to shortwave infrared.

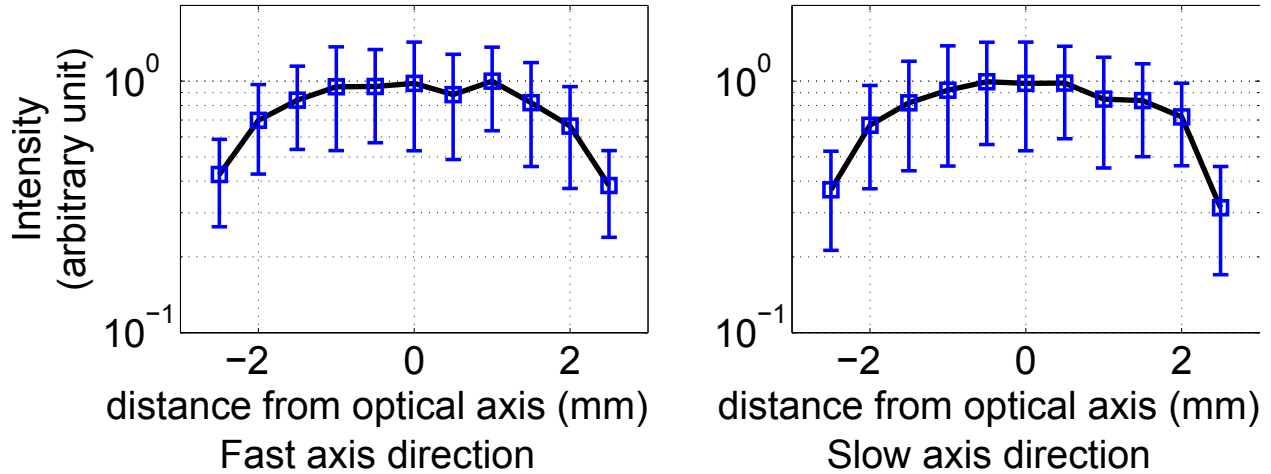


Figure 3.16: Variation in the OCT images across the field of view. The maximum diffraction limited field of view for this objective is $\sim 4.7mm$ in diameter. When we approach this limit the intensity drops.

3.5 Practical considerations

While the design of our OCT system is presented in this chapter it is beneficial to include some practical tips about the alignment procedure of an OCT system. These practical points can facilitate the OCT fine alignment particularly when the user with a no or minimum optical experience.

Scan and tube lens mechanisms. The scan and tube lens mechanisms in our design are two identical Plössl compounds. We suggest first putting the compounds together. Then assembling them to form a relay mechanism. The two Plössl lenses should be placed at the approximate distance by connecting them using a tubing and proper tube adapter mechanism. For fine alignment, the relay mechanism should be illuminated with a collimated infrared light at $\lambda \approx 1300nm$. The outcome should remain collimated at a distance more than a foot. If not, use the tube adapter to adjust the distances between the scan and tube lenses. The beam diameter can be investigated visually using a near infrared (NIR) detector card. Once the optimal distance is achieved lock the adapters using retro rings. Two identical relay lens mechanisms are needed in this design. These pre-aligned mechanisms are used in the sample and reference arms.

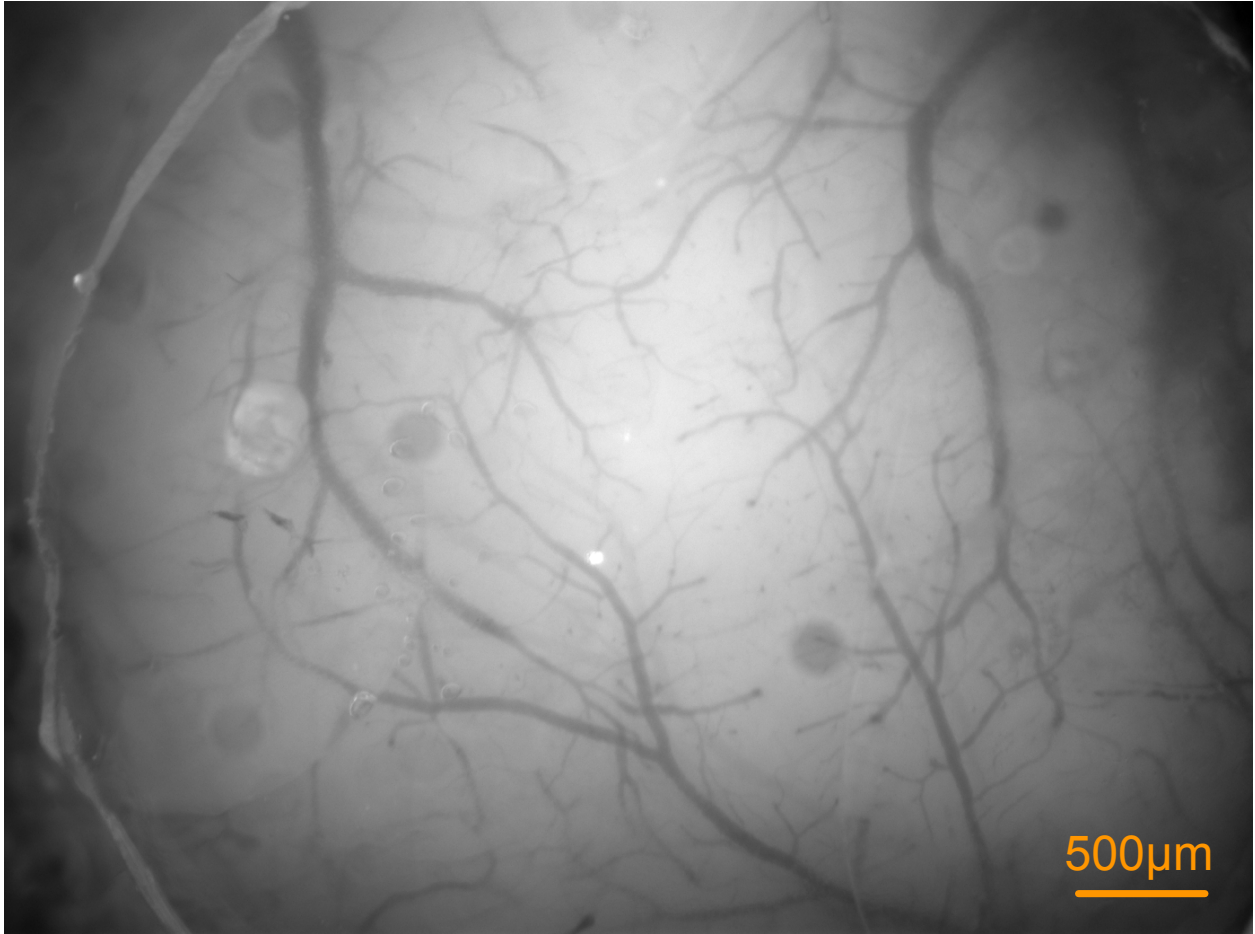


Figure 3.17: A sample fluorescence image captured by the device. The animal was a Thy1::ChR2/H134R-YFP mouse with yellow fluorescence protein expressed in excitatory neurons. The image shows the morphology of the vessels under a thin layer of skull (thickness of $\sim 100\mu m$).

Aligning the scan head. The scan head consists of a light collimator, a translational stage, and two galvanometric mirrors that should be aligned properly. We use a small beam diameter galvanometric system package from Thorlabs. The package includes the necessary drivers, heat sinks, and power sources for proper function of the galvanometric mirrors. The galvanometric mirrors should be clamped using the custom made brackets, while the brackets can be mounted on a holder using cap screws. It is helpful to first attach the brackets loosely. Then inserting the first scanning mirror. Once in place, by turning the drivers on and commanding the mirror to go to angle 0. The body of the mirror should turn to approximately 45 degrees with respect to the collimator axis and then locked at that

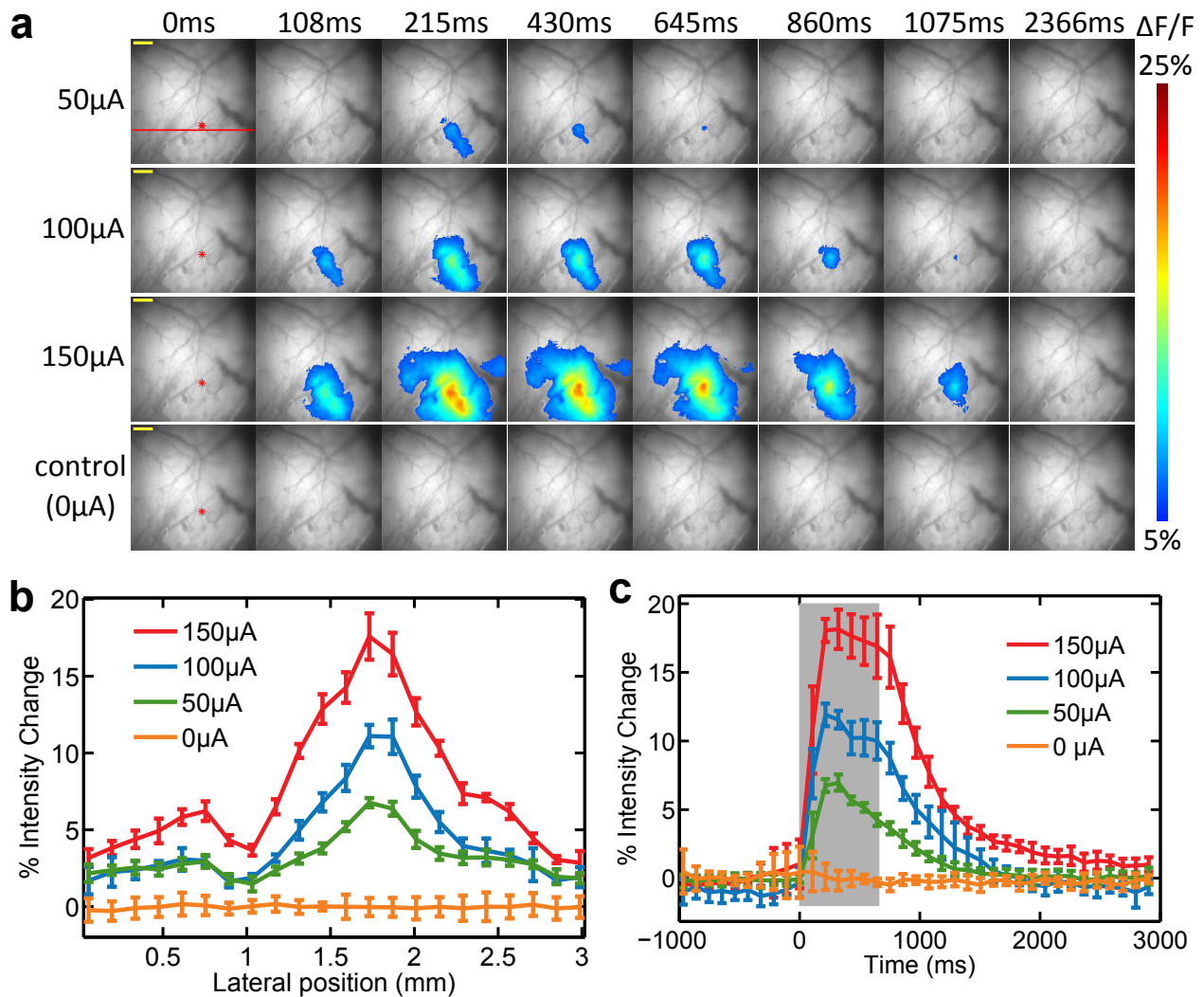


Figure 3.18: A sample result of calcium imaging. Stimulation pulses at $50\mu A$, $100\mu A$, and $150\mu A$ were delivered to the brain of a GCaMP6f mouse. The stimulation duration was $600ms$ with a pulse frequency of $150Hz$. a) The change in the fluorescence intensity is color coded and superimposed on the original images. The stimulation location is shown by an asterisk. b) the intensity line profile across the line marked in panel (a). The line profile is obtained by averaging 3 frames starting at time $t = 200ms$. c) the intensity temporal profile at the site of stimulation. The error bars show the standard deviation across at least 5 recordings at each current level.

position before placement of the second scanning mirror. The same procedure can be used to install the second mirror. The alignment procedure can be started using a visible laser. The laser should be hitting almost the center of the mirrors. This can be done by adjusting the position of the collimator which is mounted on a translational mount. If the beam is not incident at the center of the mirrors a beam truncation can be detected by looking at

the beam profile after the scanning mirrors. Once the beam location on the mirrors are adjusted, the angle of the mirror should be tuned such that the beam exits the scanning head and hits the center of the scan lens and is parallel to its optical axis. This process can be facilitated by first connecting an empty lens tube instead of the relay lens to the scanning head. This tube uses two adjustable iris at its ends. Attempt to angle the mirrors such that is incident at center of the first iris while monitoring the location of the beam at the other end of the tube. At the beginning the irises are opened at their maximum diameter. As the alignment process moves forward the iris diameters can be reduced to achieve a reasonable alignment. This is when the beam is almost parallel to the optical axis and passes both irises when their diameters are less than 1mm s. If the beam is almost parallel to the tube axis but is off-centered more than 1mm then the galvanometric mirrors and the collimator locations should be relocated. This can be done by loosening the mirrors and translating them slightly in the desired direction. After each translation, the process should start over until satisfactory result is achieved. Once the alignment is done using the visible light, it should be confirmed by the OCT light as well. If the OCT light beam is not centered of there is beam cut then the same process can be repeated. The pre-alignment with a visible light, reduces the alignment time of the infrared light. We do not recommend using translation mounts for the galvanometric mirrors as they can increase the vibration in the scan head as the mirrors move.

Installing the relay lens. After the scan head alignment, the relay lens tube (scan lens + tube lens) can be installed in place. The back focal plane of the scan lens should be located center of the two scan mirrors. The distance of the lens tube and the mirror can be adjusted by using a proper tube adapter to connect the lens tube to the scanning head. The ideal position for the tube lens is such that the conjugate image of the mirrors locate at the back focal plane of the objective. The conjugate image of each mirror can be located by commanding the mirror to scan at its maximum angle. Using the infrared detector find the

location that the beam has the least motion. If the location of the conjugate image of the mirrors are far from the designated locations by more than a few millimeters ($\sim 3 - 5mm$) tune the tube lens location by adjusting top tube adapter.

Reference arm. The reference beam should illuminate the reference mirror perpendicularly such that it travels back to the collimator and couple into the optical fiber. For this reason the reference mirror is mounted on a kinematic mount which can adjust the angle of the mirror. The coarse alignment can be done using the visible light and placing a pinhole ($< 1mm$ in diameter) at the center of the beam. The mirror angle should be adjusted until the reflected beam travels back through the pinhole. At this point the pinhole can be removed and the fine tuning can be done by maximizing the power of light that is re-coupled to the fiber. An optical circulator is necessary to guide the re-coupled light toward the detector.

There is an adjustable iris in the reference arm that controls the strength of the reference beam at the time of experiments. This iris can be used as a pinhole during the coarse alignment. This iris should be placed in the path of the collimated beam. The reference arm can incorporate paths for different objectives by adding a removable folding mirror in its path. The mirror can be inserted to the arm to redirect the light beam to a path which is designed for the desired objective.

Typically the location of the zero path difference (the conjugate location of the reference mirror in the sample arm) should be above the imaging focal plane ($\sim 200 - 500\mu m$). This way the whole depth of focus is within the sample. Such fine positioning can be done by mounting the reference mirror on a high resolution translational stage. Moreover, in many applications, the location of the zero path difference with respect to the imaging focal plane needs to be adjusted according to the sample configuration and depth of interest.

Spectrometer alignment. After placing the collimator and grating at their designated positions, one should confirm that the OCT beam incident on and diffracted by the grating

is not partially blocked by the rotary mount. If the beam is truncated, the collimator should move accordingly. Use the rotatory mount to adjust the roll angle of the grating so that the diffracted OCT beam forms a horizontal line. When the input is a monochromatic light at $\lambda = 1300nm$ rotate the bottom rotatory mount to adjust of the yaw angle until it follows the desired angle ($180 - 2 \times 48.6 \approx 83^\circ$) with respect to the incident beam. If a monochromatic light source is not available, the OCT beam can still be used to coarsely adjust the yaw angle (the bottom rotatory mount). Then place the achromatic lenses at the designated locations. The diffracted beam should be incident as close as possible to the center line of the lens mechanism, otherwise lens aperture may truncate the diverging beam, or optical aberrations increase the focal spot size. By using a NIR detector card confirm the image plane. It is the location that the horizontal line is the sharpest and brightest. If it does not match the expected image plane, check the alignment of the lensing mechanism. If it is accurate, then check the alignment and angle of the grating.

The diffracted OCT beam that is focused by the lens mechanism forms a horizontal line. The line-CCD detector array should be aligned properly with this line. Under an imperfect alignment the recorded spectrum is contaminated with artifacts, which may appear as a strong high frequency pattern in the recorded interference pattern. Our suggestion is to first tune the angle of grating by using fine adjustment knob in PRM1 until a horizontal line is formed at the focal plane. After confirming the focal location of the diffracted beam, place the detector at the desired locations. By reading the detected spectrum ensure that there are no significant artifact in the recorded spectrum. If there is continue fine tuning until an artifact-free spectrum is obtained. This means the spectrum should not include high frequency patterns and resemble the spectrum that is provided by the light source manufacturer. To find proper axial placement of the detector, place a mirror in the sample arm so there is a strong sinusoidal interference pattern. Adjust the location of the mirror in the sample arm until a high frequency interference pattern is formed on the camera detector. Adjust the position of the detector along the lensing optical axis until the interference is at

its maximum amplitude. Due to a long depth of focus of the beam it is possible to find a range of displacement which causes no significant amplitude change. Then the best positioning is around the middle point of that range. Typically it is necessary to do this alignment in an iterative fashion in which periodically the grating angle and camera horizontal are aligned until it approaches the best performance. Placing the camera on a horizontal axis translational stage might be helpful; however, we did not find it necessary. This alignment process might take about 1 hour.

3.6 Software

In this section I cover the signal processing of the structural as well as the functional SD-OCT.

3.6.1 Structural SD-OCT processing

The structural SD-OCT includes all the basic steps: resampling, Fourier Transform, fixed pattern removal, and dynamic range compression.

Resampling

A resampling algorithm is used to remap the interference pattern, which is recorded in the wavelength space, to the wavenumber space. This resampling algorithm needs a front face mirror to be placed as a sample in front of the objective lens. The interference produced by the mirror should be a perfect sinusoidal signal in the wavenumber (frequency) domain., which means the corresponding analytical signal has a linear phase as a function of frequency. In our resampling algorithm, we first calculate the Hilbert transform of the interference produced by the mirror and its corresponding phase. Since the line CCD camera is sampling the interference signal in the wavelength domain, this phase is not a linear function of the

pixel number. We fit a 5th order polynomial to the phase information, while the horizontal axis is the wavelength and the vertical axis is the phase information. In polynomial fitting, the weights of the first and last 10% of pixels are set to zero, because SNR in those pixels is relatively low. The polynomial fit helps to remove fluctuations in the phase that are introduced by noise. The phase span of the analytical signal, which is obtained from the fitted polynomial, is then divided into equidistant intervals. To find camera pixel corresponding to each of the equidistant phase values, then another interpolation is performed. Then, camera pixels are indexed from 1 to N , where N is number of camera pixels, and are assumed to be a function of phase. Assuming pixel index as a function of phase, then we estimate new indexes at the equidistant phase values, obtained from the previous step. The new indexes are not integer and represent virtual pixels in between the original pixels of the camera. If we estimate the interference in the new indexes, the result should be a signal which is uniformly sampled in the frequency domain.

In order for the SD-OCT image reconstruction, the recorded interference pattern is first interpolated at the new wavelengths. and then a Fast Fourier transform (FFT) is used to convert the interference data into complex-valued axial scans (called A-scans or axial depth profiles).

Fixed Pattern Noise and Background Removal

Due to reflection from some of the constant surfaces (such as lens surfaces, dichroic mirrors, and etc.) there are interferences which are stationary over different A-scans. Additionally due to dark current of the camera, the recorded interference signal is noisy. This noise is consistent in different A-scans and appear as a fixed pattern noise (FPN). The FPN and constant background which are superimposed on the OCT images are usually strong and degrade the image quality (Figure 3.19). Such fixed patterns can be detected and subtracted by simply calculating median of all the A-scans at each depth and subtracting it from the data (111). The data are complex-valued and the fixed pattern removal is done on the

real and imaginary parts of the OCT data independently.

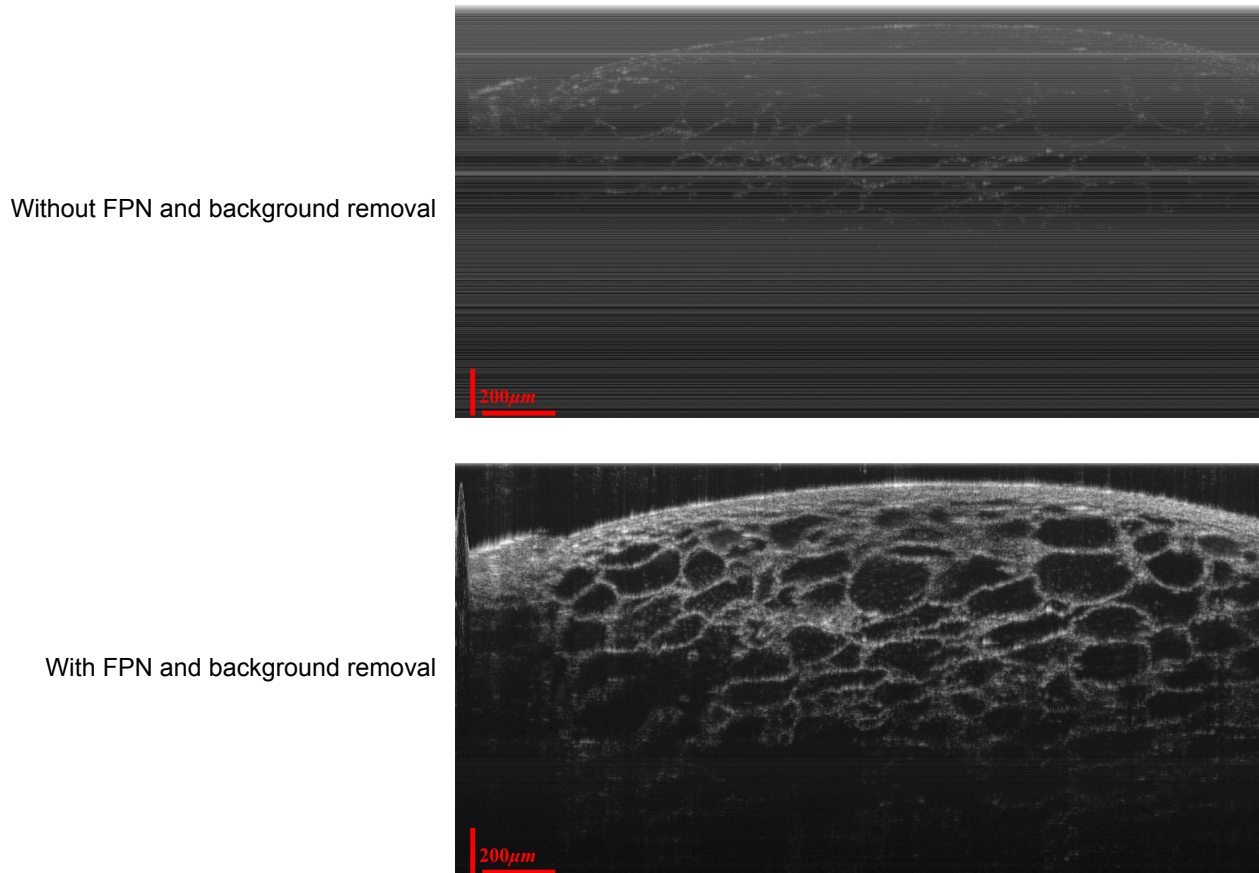


Figure 3.19: Fixed pattern noise (FPN) and fixed background cover the cross-sectional OCT image of an orange pulp. Using background removal we can improve quality of OCT images.

After FPN and background removal, Amplitude of the complex-valued depth profiles are used to obtain the cross-sectional images of the specimen's structure. The intensity of the structural data drops as the depth increases mostly due to an inherent sensitivity drop-off of SD-OCT at higher depth (78). The nonzero focal spot-size of the lensing, nonzero camera pixel size, cross talk between the camera pixels, and non-uniform sampling in the wavenumber space are the imperfections that are responsible for the sensitivity drop-off. Beside the inherent short-comes of the spectrometer, the spot imperfection at the sample arm will also affect the interference intensity. Ideally at the focal spot, the beam should be a plane wave, which means the optical path difference between different rays should

be zero. However, away from the focal plane the beam is not a plane wave and OPD increases as we get further from the focal. Higher OPD causes rays of light traveling from different paths, be out of phase when they reach the sample and do not form a constructive superposition. Moreover, the efficiency of coupling to the fiber drops noticeably for the light that is reflected from surfaces outside the focal plane. All these imperfections in the system cause the intensity of the reconstructed structural OCT image to be nonuniform and significantly varies at various depths.

3.6.2 Velocimetry

Since Doppler-based velocimetry requires much less number of recordings compared with the statistical model-based velocity measurements (87), (88), (112), (91), (89), we used Doppler effect to estimate velocity of red blood cells in tissue. Frequency shift induced by Doppler effect is usually, very small compared to the incident light frequency and practically it is not feasible to measure it directly. Instead Doppler effect can be detected by analyzing the phase of complex-valued depth profile at each point over a certain period of time. This is equal to measuring the phase change is produced by axial displacement of a particle inside a voxel (44). Whenever there is an axial movement, smaller than the axial resolution of OCT, this movement will not be visible in structural OCT but affects the phase of SD-OCT value at that position. Assuming constant velocity between the two recordings, this phase change is the same as the phase change we observe from Doppler point of view.

One of shortcomings of phase resolved Doppler is its Low sensitivity which makes it impractical to detect small velocity values. We developed our own technique to measure the velocity which is similar to method presented in (44). In our technique we oversample the tissue such that up to 7 consecutive A-scans can be assumed from the same position. Then, phase fluctuation of each of these A-scans, which is usually produced by tissue bulk movement (35), with respect to the central A-scan (4th A-scan) is detected and compensated. We use $\Delta\phi_l = \angle \text{median}_z(A_l(z)A_4^*(z))$ as the phase fluctuation of the l th A-scan, where $l = 1, \dots, 7$,

'*' denotes complex conjugate, $median_z(.)$ calculates median of its argument over different depths, and ' \angle ' returns angle of a complex value. After compensating for phase fluctuations, we detect the Doppler induced phase change at each depth z , by calculating the fast Fourier transform (FFT) of 7 successive complex-valued SD-OCT data at that depth. Signal in the frequency domain can be decomposed into three components:

- constant component: this component will not change over time and is usually produced by a constant sample, or fixed pattern artifact.
- phase modulated component: particles moving in the axial direction will produce a complex value which its phase is changing over time.
- noise: particles moving in the lateral direction, fluctuations in the spectrum of the light source, and measurement noise are categorized under this group.

Eventually the complex value for the l^{th} recoding can be written as:

$$x[l] = A_s e^{i\Phi_s} + A_p e^{i\Phi_p[l]} + A_n e^{i\Phi_n[l]}, \quad l = 0, \dots, 7 - 1,$$

where subindexes s , p , and n stand for static tissue, phase modulating moving particle, and noise components. A is the amplitude and Φ is the phase of the corresponding components. Assuming the moving particle has constant velocity over the recoding time, then $\Phi_p[l] = \Phi_0 + l\Delta\Phi$. In this equation Φ_0 is the initial phase of the moving particle, and $\Delta\Phi = 2\kappa v\Delta t$, where v is the axial velocity of the particle, and Δt is the time interval between the scans. Consequently the spectrum of this short signal will have most of its energy concentrated around $\omega = 0$ produced by the constant tissue and $\omega = \Delta\Phi$ caused by the moving particle. The frequency components which most of the signal energy is centered around it, is estimated by weighting each frequency component with the energy at that component and then calculating the weighted average. Weight of the zero frequency was

set to zero to reduce the effect of constant tissue. Before the Fourier transform signal was zero-padded to increase its length by 3 times. Also for pixels that the intensity of OCT signal is below the noise level the velocity was set to zero. The velocity is calculated as:

$$v = \frac{\Delta\Phi}{2\kappa\Delta t}$$

This method will be less susceptible to noise while still able to detect motion of RBCs in small capillaries (Figure 3.20).

3.6.3 Angiography

For angiography we rely on the fact that motion of a particle at depth z will change the complex-valued OCT signal at that point. To detect the change we scan each cross section 10 times (record 10 successive B-scans), compensate for the tissue motion, and calculate the normalized difference between the B-scans. This process is elaborated in the following paragraphs.

Motion Compensation

Motion is a common problem in many in-vivo imaging techniques. Even if the sample is fixed to minimize the tissue movement, heart beat and breathing produce motion in tissue. SD-OCT is a high resolution imaging modality and is susceptible to micro motion. To obtain high quality OCT angiograms computer algorithms are necessary to compensate for motions (113).

Since OCT is a laser scanning-type imaging system, different lateral positions in each B-scan are recorded at different times and motion is not uniform across the image. Therefore, a local motion compensation algorithm is developed to reduce the motion artifact. In the proposed method, to detect the motion between two B-scans, the first B-scan is considered as a reference. In each lateral position of the second B-scan, motion is detected by cross

correlation maximization: we shift the corresponding A-scan and its neighbors (a block of 11 A-scans consisting of the corresponding A-scan at the center and 5 A-scans to each of its sides) axially and laterally. At each shift the cross correlation of the block and its corresponding block in the reference B-scan is calculated. The shift that maximizes the cross correlation is the local motion of the corresponding lateral position. This process repeats for all A-scans and the detected motion is then compensated in the second B-scan. In SD-OCT intensity of the initial surface is usually very high compared to the deep tissue due to the inherent depth dependent intensity drop of the SD-OCT and also higher refraction change that happens when light enters the tissue. Therefore, the cross correlation is mostly affected by the initial surface. To obtain a better estimate of the motion across the depth, we reduce the dynamic range of the intensity of images prior to motion compensation. The dynamic range compression was simply obtained by taking the intensity of OCT A-scan to a power smaller than 1.

Cross-sectional Angiogram

After motion compensation of two B-scans recorded from the same cross section in the specimen, the normalized difference between them is calculated. If we denote the two B-scans with B_1 and B_2 for lateral position x and axial depth z the angiogram $C(z, x)$ is calculated by:

$$C(z, x) = \frac{|B_1(z, x) - B_2(z, x)|}{b + |B_1(z, x)| + |B_2(z, x)|} \quad (3.1)$$

where b is a positive constant to reduce effect of noise at positions where both $|B_1(z, x)|$ and $|B_2(z, x)|$ are very small. In our experiments of b was imperically set to $b = average_{z,x}(|B_1(z, x)| + |B_2(z, x)|)$. The normalization process is used to cancel out the intensity variations across the image due to factors such as sensitivity drop off or tissue absorption.

In our experiments we record 10 B-scans per each cross section. For each of 2 B-scans out of 10 (45 combinations) the motion is compensated and then the normalized difference was calculated according to Eq. 3.1. The 45 angiograms are combined to reduce the noise and motion artifacts and obtain one cross-sectional angiogram for that position as follows. The proposed motion compensation algorithm is not able to detect and compensate for the motions along the y axis (direction normal to the plane of the B-scan). The motions that are not compensated correctly for, introduce noise/artifact into the cross-sectional angiogram. Such an artifact can be detected as increase in the angiogram of A-scans where motion has not been compensated. Consequently the motion artifact at each axial scan increases the median of intensity on that axial scan. To efficiently decrease the motion artifact we combine at each lateral position we select 10 axial scans that have the smallest median. These selected axial scans are averaged together to produce the final line angiogram of that lateral position. Figure 3.21 shows the efficacy of local motion compensation and selective averaging in reducing motion artifacts.

3D Angiogram

By obtaining the cross-sectional angiograms for different tissue cross sections, the 3D map of vessels can be reconstructed. 3D map is useful to vessels in different layers of brain. Moving red blood cells disturb the light passing through them. This will produce artifacts below the vessels which usually can be seen as shadows (Figure 3.22). At each position the shadowing effect is stronger if the light distortion produced in the upper pixels is higher. For 3D visualization purposes we would need to remove the shadow. The shadow removal algorithm we are using is simple: at each position, we attenuate the angiogram value based on how much distortion is introduced by tissue above it. The larger the vessels or the more the number of vessels above a pixel, the higher the distortion. The attenuation is performed

by applying a biased sigmoid to the angiogram value at each pixel:

$$B_d(z, x, y) = \frac{1}{e^{-25(B(z,x,y)-b(z,x,y))} + 1} \quad (3.2)$$

where $B(z, x, y)$ and $B_d(z, x, y)$ are the angiogram before and after deshadowing, respectively, at position (z, x, y) . Parameter $b(z, x, y)$ is the bias value at each point. By changing the bias based on the intensity of angiogram above each point we can control amount of shadowing effect we will allow for each vessels. Larger values for b will remove more of the shadowing effect, but also will remove some of the capillaries since their angiogram values are usually weak. Therefore, value of the bias at each point should be selected carefully. Empirically we found $b(z, x, y) = \max(.25, \sum_{i=0}^{z-1} w_{z-i} B(i, x, y))$ provides a good balance between the number of capillaries that are attenuated and the amount of shadowing effect. In this equation w_k is the weight at depth k which is selected to be a Gaussian function of the depth. Figure 3.22 shows an example of the effect of deshadowing on a cross-sectional angiogram.

Due to the distortions that are created by the shadowing effect, in many applications a maximum intensity projection (MIP) along the depth of of the angiogram is used to visualize the vessel network and measure vascular diameter. At the first step a 3D Gaussian kernel with a standard deviation of 5 pixels is applied to the 3D angiographic data. Then the depth of interest is selected. This is usually includes a thickness $\sim 200\mu m$ to $400\mu m$ across the field of view. Then, the average of the largest 3 values across the depth is calculated at each lateral location. The results can be further processed by applying a local contrast enhancement such as histogram equalization (Figure 3.23).

While the maximum intensity projection can be applied to the the raw 3D angiogram data or the data after deshadowing process, we recommend using the raw angiography data.

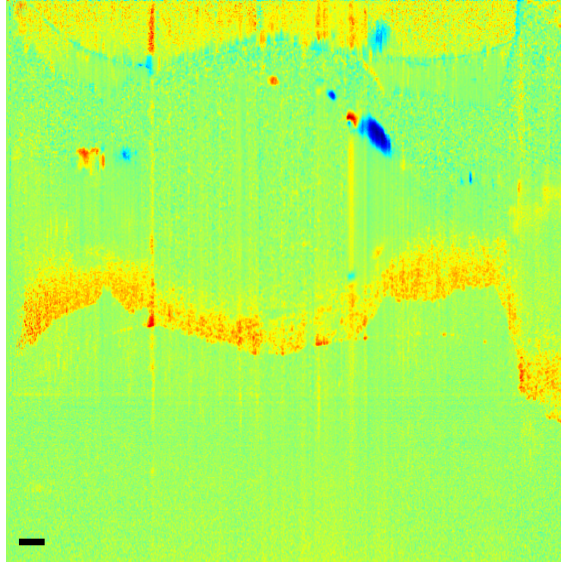
The vessel's shadows do not considerably affect the quality of MIP images; however, the proposed deshadowing process attenuates the intensity of some small vessels and capillaries. The capillaries that are attenuated by the deshadowing usually are removed during the maximum intensity projection process.

3.7 Conclusion

This chapter presented details of the optical design of the SD-OCT scanner that was used in our studies. The system was designed to achieve a lateral and axial resolution of $5.1\mu\text{m}$ and $4.4\mu\text{m}$, respectively, and the desired field of view was over 4mm in this configuration. We used a gold nanoshell embedded 3D phantom to measure the lateral resolution and the effective field of view. The axial resolution of the system was measured by using a mirror in the sample arm. The performance of the device was close to their theoretical values. The design allowed us for incorporating a visible path in the system than can be used for optogenetic stimulation or fluorescence imaging. Easy transportation of this design increases the flexibility of experiments as the device, including reference arm, light source, computer, data acquisition system and power supplies, can be transported to various locations. This feature greatly facilitates the research throughput by allowing the device to participate in multiple research projects in parallel with each other. Also, optical aberrations associated with three popular and economical scan/tube lens systems were analyzed and the performance of two of these lens mechanisms were experimentally measured in an OCT scanner. Our simulations demonstrated that using singlet lenses or achromatic doublets as scan/tube lens reduces the FOV with diffraction-limited resolution and degrades the quality of OCT images due to astigmatism and field curvature. A four-element semi Plössl compound lens system provides superior performance over a FOV of diameter 4mm when used in combination with an objective of focal length 18mm. To experimentally measure the resolution of OCT systems with different scan/tube lens mechanisms, we prepared a

transparent 3D phantom with embedded gold nano-shells. The outer diameter of these particles was $\sim 231nm$ which was significantly smaller than the theoretical resolution of our OCT system. Using this 3D phantom, the PSF of the OCT system for each of the scan/tube lens mechanisms was measured experimentally. These measurements confirm that achromatic doublet lens as scan/tube lens can not provide the diffraction-limited performance over a field of view larger than $2mm$ in diameter, while with the four-element semi Plössl lens we were able to achieve PSF with the FWHM smaller than $7\mu m$ over a field of view with a diameter of $4mm$. This performance is acceptable for many OCT applications; however, to achieve a larger FOV, custom-made Plössl lenses similar to what has been presented in (70) can be employed. In fiber-based OCT scanners, backscattered photons need to couple back into the same single-mode optical fiber from which they are emitted; therefore, light travels back and forth through the same optical components. A comprehensive two-way simulation is necessary to analyze aberrations in a more accurate manner and also to consider diffraction effects on the overall resolution. The authors also suggest investigating the far-field backscattering by the gold nano-shells under Gaussian field illumination. This can give a better insight on possible differences between the measured resolution with a gold nano-shell phantom and real-world specimens.

Proposed method



Phase-Resolved method

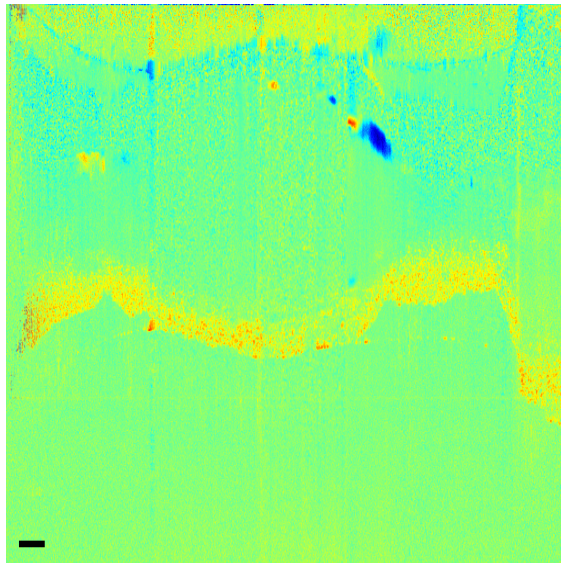
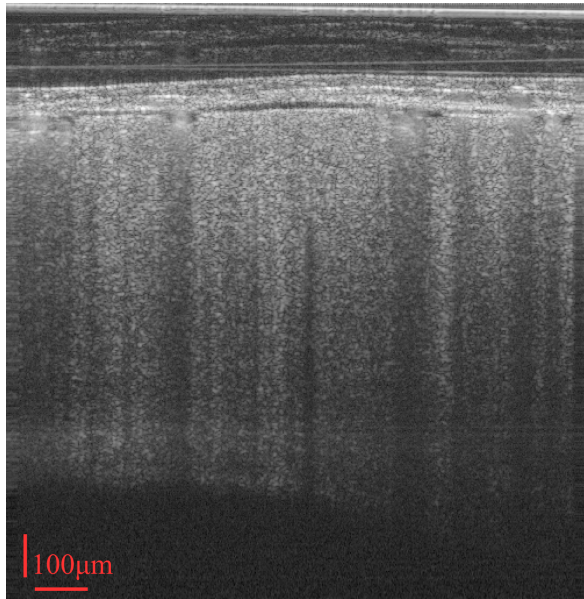
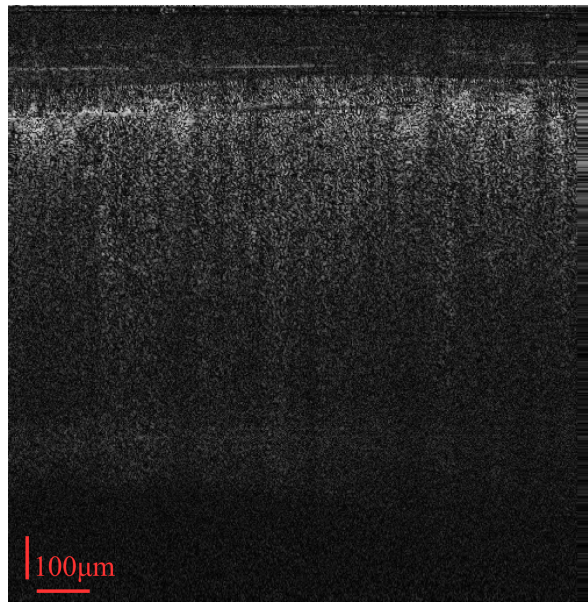


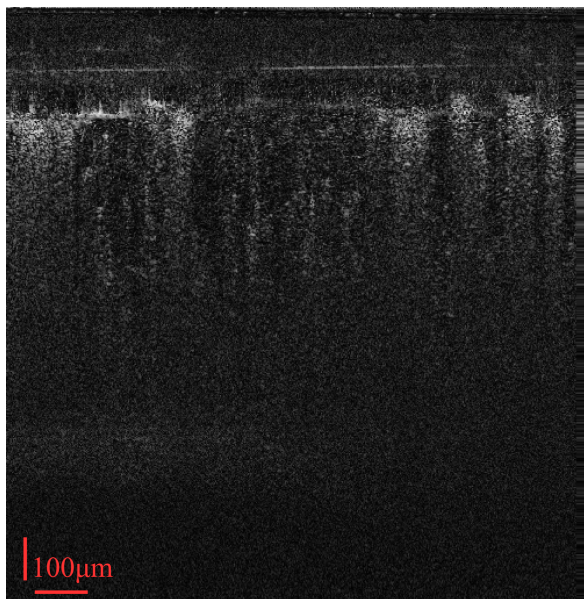
Figure 3.20: Comparison between the velocity profiles obtained by the proposed method and phase-resolved method. There are some vessels in the top image that can not be detected with the phase-resolved method.



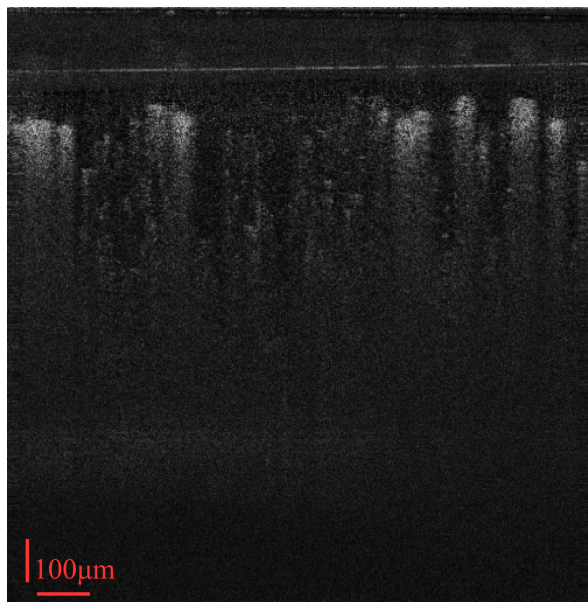
a) Structural SD-OCT image obtained from a mouse brain



b) Cross-sectional angiogram without motion compensation



c) Cross-sectional angiogram with motion compensation



d) Cross-sectional angiogram after selective averaging

Figure 3.21: Cross-sectional structural and angiographic images of a mouse brain.

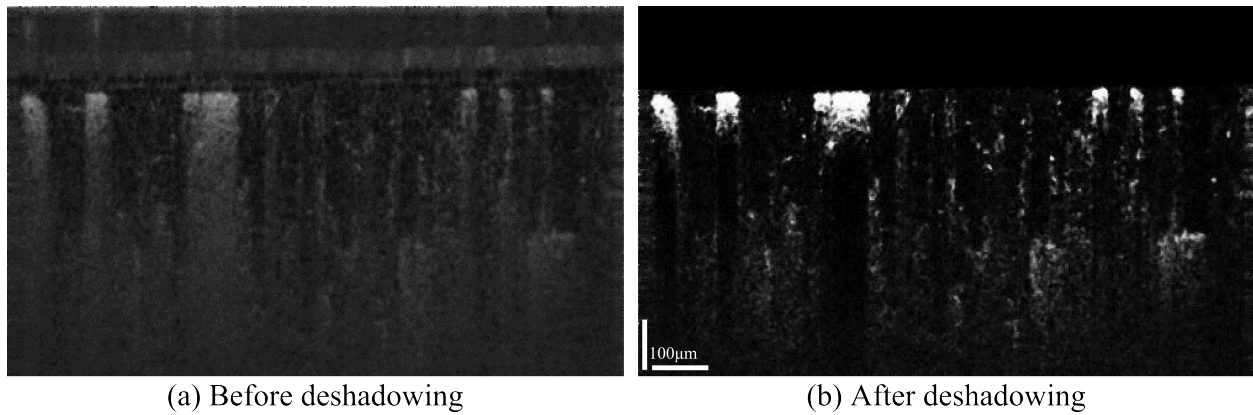


Figure 3.22: A cross-sectional angiogram of a mouse cortex before (left) and after (right) deshadowing. Deshadowing can remove the shadows created by large vessels while keeping most of the capillaries intact. The contrast of the angiogram also has significantly improved after applying the deshadowing.

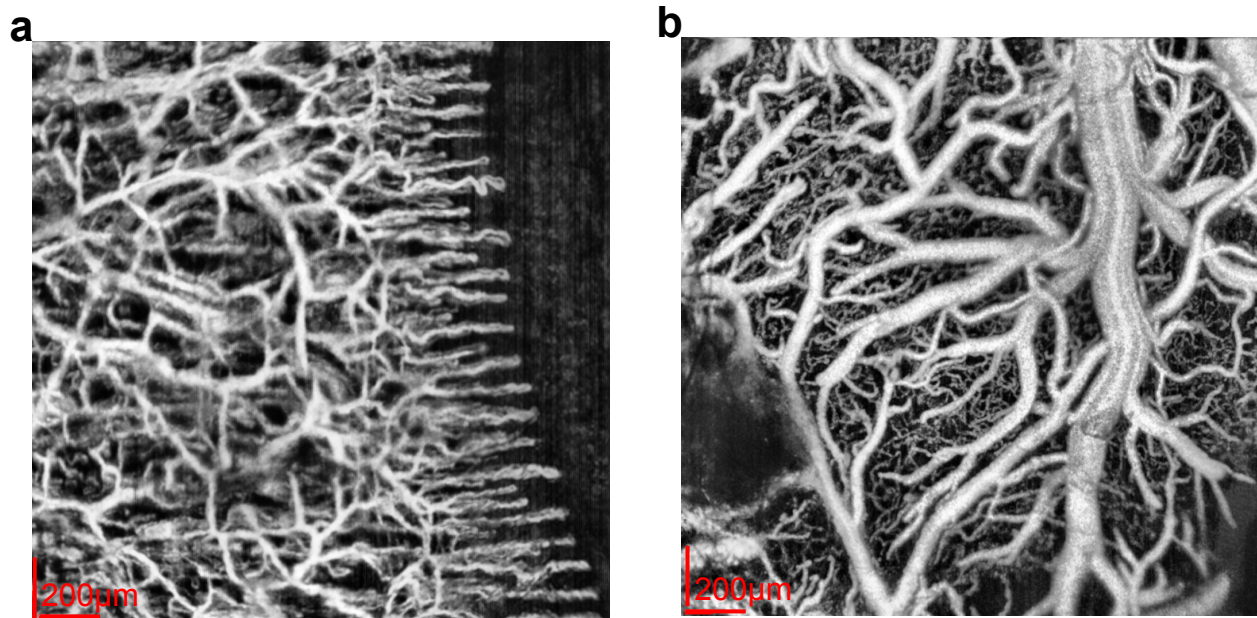


Figure 3.23: Examples of maximum intensity projection of the OCT angiography data for human finger nail bed (a) and rat brain (b) after local contrast enhancement.

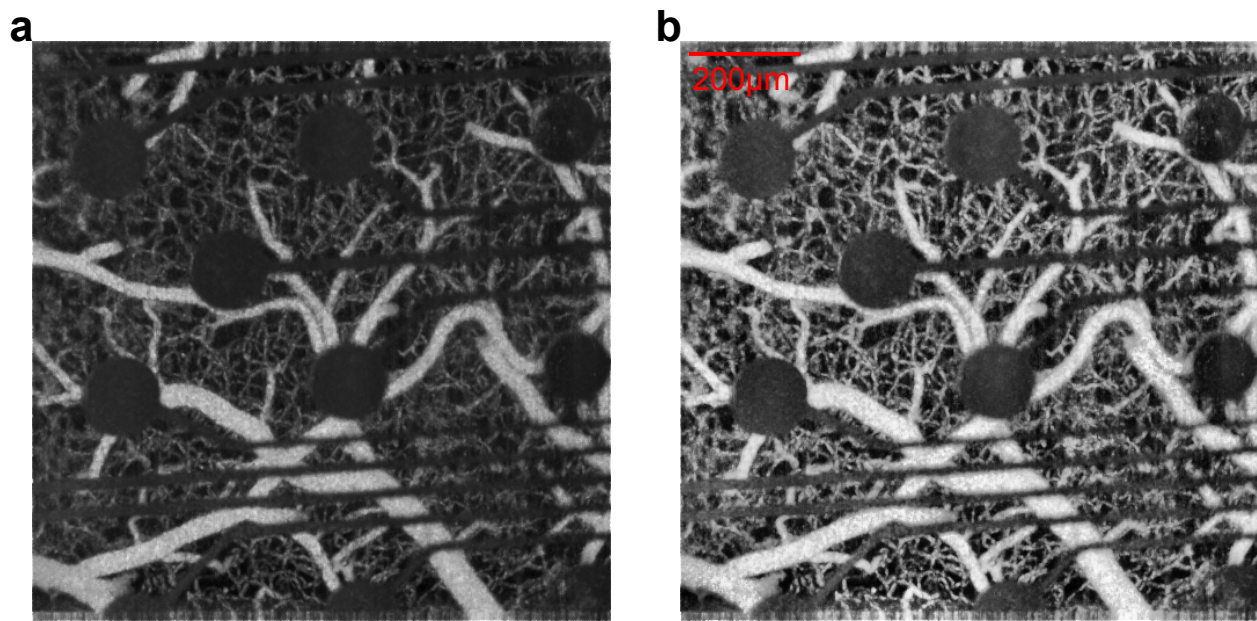


Figure 3.24: A example of contrast enhancement on MIP OCT angiograms. (a) the MIP image in a mouse brain prior to histogram equalization. (b) the same MIP in (a) after applying histogram equalization. There are dark areas in the images which are produced by platinum ECoG devices. The platinum ECoG that was placed on the brain surface in this animal blocked the OCT beam and created dark regions in the images.

Chapter 4

Wide field brain stimulation

4.1 Introduction

Cortical blood flow and neuronal activation are two fundamentally coupled processes that regulate function in the brain. It is well understood that neuronal activity is intimately coupled to hemodynamic signals in the central nervous system (114), (16). However, the mechanisms that are involved in neurovascular coupling or functional hyperemia, at the molecular or system level, are still not completely identified. To assess neurovascular coupling, specifically in cortical regions, we need mechanisms to stimulate neurons in large scale networks and simultaneously monitor the induced hemodynamic signals. For this purpose, we combined optogenetic neurostimulation with Spectral Domain Optical Coherence Tomography (SD-OCT) in an integrated platform which allows us to optically stimulate cells inside the field of view and simultaneously monitor changes in vessel diameter and blood velocity.

Optogenetics is an emerging neuromodulation modality in which specific cell types of interest are genetically targeted to produce light activated proteins (4), (3), (115), (1), (116). Once these proteins are expressed, the activity of the targeted cells can be manipulated with high spatial and temporal resolution by exposing the cells to appropriate wavelengths (117). Advent of optogenetics in recent years has provided the opportunity to selectively modulate the activity of cells in the large networks of the brain and study the contribution of each cell-type in functional hyperemia.

In previous publications, optogenetics is combined with other imaging modalities, such as functional magnetic resonance imaging (fMRI), to study neurovascular coupling in small rodents (9), (17), (10), (11). The fMRI data that is presented before provides insight to the

global and local distribution of blood oxygenation level dependent (BOLD) signal following optogenetic stimulation of a specific neuronal subpopulation. Nonetheless, the spatial and temporal resolution of fMRI is always the major shortcoming of the technology. Moreover, the BOLD signal does not contain detailed information about the induced changes in blood velocity or vasodynamics separately. In some advanced studies in recent years, multiphoton imaging is used to investigate functional hyperemia at the cellular level (19), (20). In multiphoton imaging, cellular activity (neurons and astrocytes) and hemodynamic signals are both recorded optically via fluorescence imaging. Adding optical stimulation to this combination, can make the experimental design significantly complicated. SD-OCT provides a mechanism to image vascular network with high resolution and measure velocity simultaneously *in-vivo* via Doppler tomography. Few other relatively less complex optical imaging methods, such as intrinsic optical signal imaging (IOS) and laser speckle imaging (LSI) (13), or laser Doppler perfusion monitoring/flowmetry (23), (24), (15), are also tested to record hemodynamic signals in the brain. While these devices are less expensive and relatively easy to use during surgeries, in terms of image quality, they do not match SD-OCT.

SD-OCT is a fast, non-invasive, and high resolution tomography technique (47), (51), (27) that is used to image semitransparent biological tissue of few millimeters thickness ((118), (28), (29), (43), (32), (112)). It has been successfully used to monitor blood flow and vasculature structure *in vivo* ((35), (37), (119), (88), (38)) and is capable of tracking variations in hemodynamics with better spatial and temporal resolution compared to most functional imaging modalities. The wavelengths that are commonly used in SD-OCT are far from those used for stimulation or fluorescence imaging. As a result, it is possible to combine SD-OCT with other optical techniques to investigate the signaling pathways involved in functional hyperemia. While OCT data acquisition is currently limited to superficial brain areas such as cortex, new advances in this field, including the addition of ultra wideband supercontinuum lasers and line CCD cameras with better sensors (in terms of the number of photodetectors in the array and sensitivity of each detector) will make it possible in near

future to significantly improve the spatial resolution, depth of focus, and the scan rate of these imaging systems and potentially covers the whole brain tissue of small rodents such as mice. Therefore, optical coherence tomography can become the superior technology in this field.

By combining optogenetics and SD-OCT technologies, we were able to record on average a 20% increase in diameter and a 100% increase in blood flow inside the middle cerebral artery (MCA) and neighboring vessels in response to optical stimulation of neurons in the cortex of transgenic mice. Observed changes in blood flow were repeatable and gradually returned back to baseline once the stimulating light pulses were removed. Optical stimulation of wild-type mice produced less than 10% change in diameter and blood flow, which is comparable to the intrinsic periodic fluctuations observed in non-stimulated cortical tissue (19). The hardware design and software algorithms are discussed in section II and experimental protocols are explained in section III. Results are included in section IV and concluding remarks are summarized in section V.

4.2 System Design

We designed a custom SD-OCT to record cerebral hemodynamic signals in mice. The system utilizes a 200nm wideband light source with a central wavelength of 1300nm (THORLABS LS200B) that delivers 10mW of optical power at the tip of a single mode fiber. In this design, the interference patterns are projected onto a 1024 pixel InGaAs line CCD (GOODRICH LDH2, maximum read-rate of 91,900 lines/sec) through a transmission grating (Wasatch Photonics, 1145 lines/mm), Fig. 4.1. The system possesses an axial resolution of 5 μ m in air. The optogenetic stimulation path is integrated into the sample arm of the SD-OCT system via a cold mirror which reflects the beam of a blue laser (LaserGlow 473nm, 100mW) while it transmits the infrared light to deliver both beams to the objective lens. The objective is a 10x telecentric lens which has 160 μ m depth of focus and lateral resolution of 4 μ m.

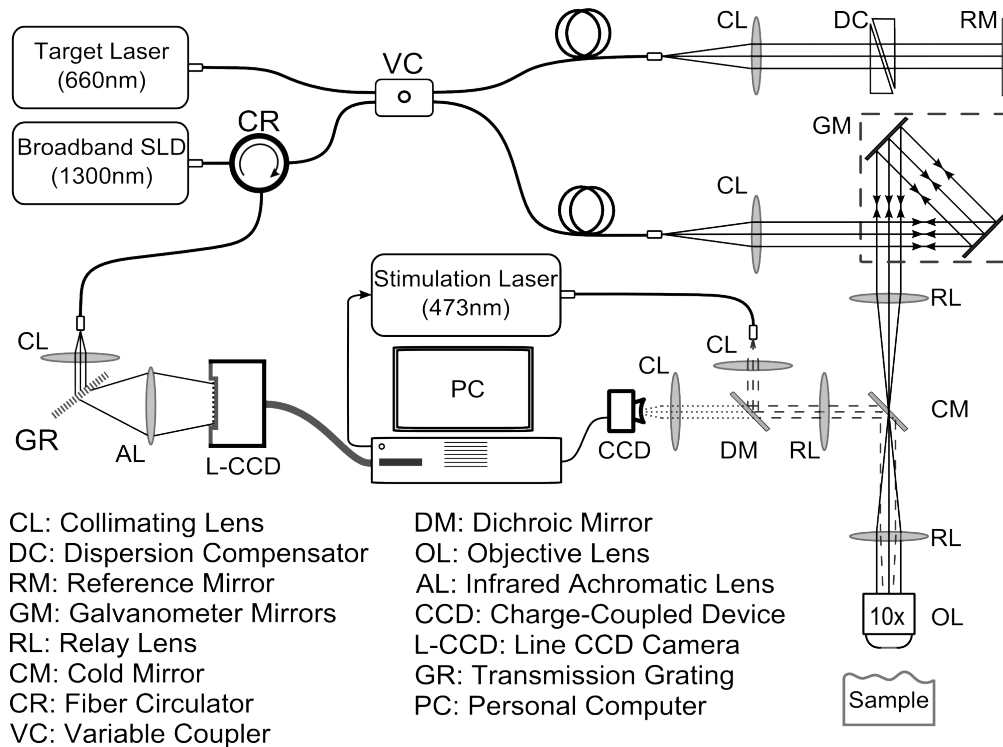


Figure 4.1: Schematic of the SD-OCT system used in the optogenetic stimulation study. The beams of a broadband infrared superluminescence diode (SLD) and a red aiming laser are coupled in the sample and reference arms using a variable fiber coupler. The red laser beam is employed for visual targeting only and is not used for the imaging purposes. Using the variable coupler, we adjust the percentage of the optical power which is coupled in each arm of the interferometer. For optical stimulation of the brain tissue, a cold mirror is integrated in the sample arm which reflects the beam of a blue laser toward the objective lens. The blue laser is controlled by a computer and generates 15Hz light pulses when the laser is activated.

At each transverse position, the interference pattern is recorded using the line CCD camera. The complex depth profile (A-scan) is obtained by applying a non-uniform re-sampling algorithm (27) to the recorded interference pattern and taking the Fourier transform of the output. Negative frequencies are canceled out and A-scans are stacked together to produce complex cross-sectional tomographs (B-scans) which are used next to generate velocity profiles or three-dimensional angiograms.

4.2.1 Velocity Measurement

One of the widely used techniques for velocity measurement in OCT is based on Kasai's method which was originally developed to measure the Doppler frequency shift introduced by the blood flow in the envelope of ultrasound echo signals (120). Kasai *et al.* estimated the Doppler shift by calculating mean angular frequency of the power spectrum of the envelope signals. A similar approach has been used in the OCT to measure the Doppler shift (82), (121). In 2008, Szkulmowski *et al.* (44) reported a new procedure to achieve high sensitivity velocity measurements by frequency analysis of A-scans recorded over time from the same position. In this algorithm, after applying the Fourier transform to the data, the frequency with the maximum intensity is introduced as the Doppler shift. Under the assumptions of additive Gaussian noise (AWGN) and ergodicity it is shown (86) that the peak frequency would be the maximum likelihood estimator (MLE) of the Doppler frequency shift and variance of the MLE will approach the Cramer Rao Lower band (CRLB). Investigations of Chan *et al.* (86) show in practice due to the decorrelation noise introduced by the red blood cells moving in and out of the voxel, the AWGN assumption would not be valid anymore. Also the MLE is sensitive to outliers and in low signal to noise ratio (SNR) its variance will be far above the CRLB. In such conditions Kasai's estimator will outperform the MLE (86). Consequently, in our measurements we estimate the Doppler shift by calculating the mean of angular frequency, as discussed later. For Doppler measurements, the tissue is sampled at 1500 A-scans per *mm*. Therefore, consecutive A-scans have more than 90% overlap and it can be assumed that these scans are recorded from the same position. To calculate the velocity at depth z and lateral position x , after zero padding and taking the Fourier transform of $B(z, x - 3 : x + 3)$, the weighted-average of the frequencies, ω_a , is calculated. For each frequency component, the weight is the partial energy at that frequency. To increase the velocity sensitivity, weight of stationary tissue (zero frequency) is preset to zero. Then, velocity (v) is calculated by:

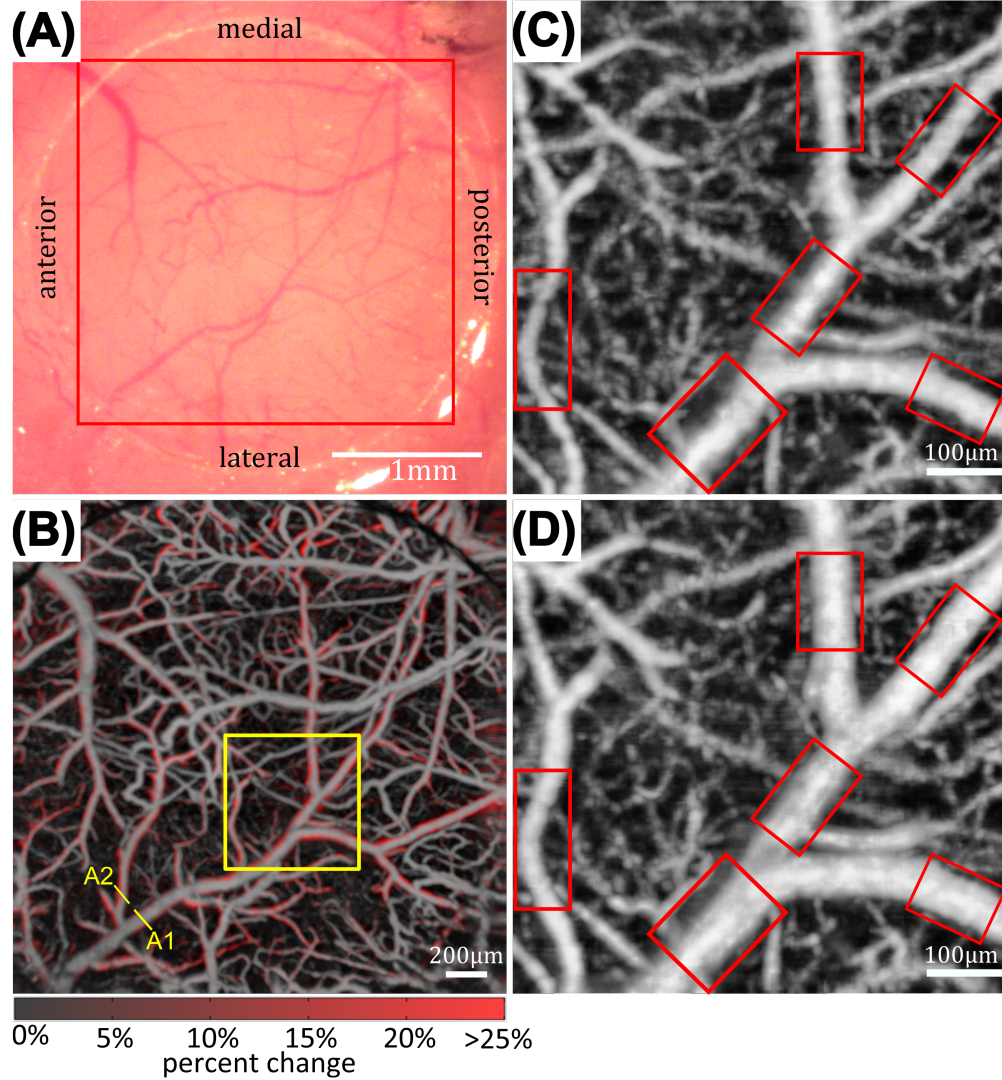


Figure 4.2: Dilation of cerebral vessels during optogenetic stimulation in a ChR2 mouse. (A) the bright field image taken with a CCD camera of a ChR2 mouse. (B) Maximum intensity projection of 3D angiogram of (A). A1 shows the MCA and A2 is one of its branches. The red color specifies the difference between the angiogram taken before and the angiogram recorded during the optogenetic stimulation. The intensity of the red color is proportional to the percent change in pixel intensity from before to during stimulation. (C) and (D) provide a closer view of the angiograms before and during the stimulation, respectively. The images show noticeable increase in the vessel diameter.

$$v(z, x) = \frac{\omega_a(z, x)}{2\pi\Delta t}. \quad (4.1)$$

Variable Δt in this equation is the time difference between consecutive A-scans which in our experiment is set to $25\mu\text{sec}$. At the positions where the energy of the complex signal is at the noise level, the velocity is considered to be zero.

4.2.2 Angiography

3D angiograms are obtained by developing a phase sensitive technique similar to the method proposed in ref. (100) in which 10 B-scans were recorded from each cross section. To remove supra-pixel motion, a local motion compensation algorithm was developed which divides the B-scan into groups of 5 A-scans, and for each group estimates the motion by finding the maximum correlation. Then sub-pixel motion is estimated by finding the overall phase change between the two corresponding A-scans in the two recordings. Afterward, the cross-sectional angiogram at transverse position x and depth z is calculated by:

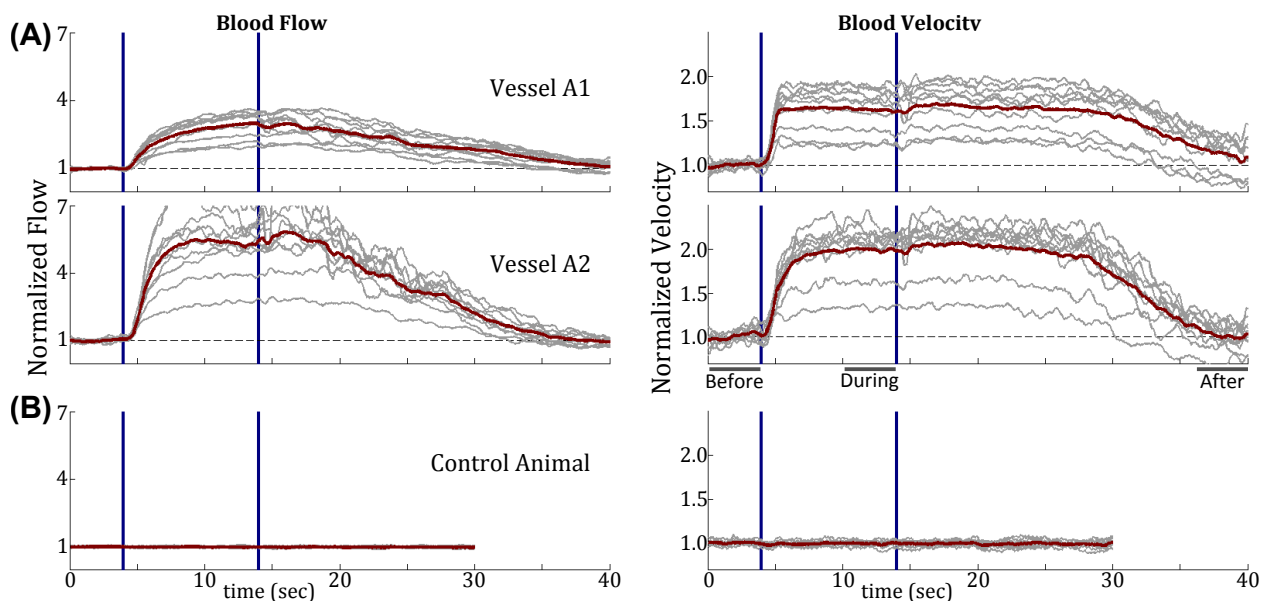


Figure 4.3: Fluctuation in the blood velocity and blood flow in a ChR2 mouse in response to optical neuro stimulation. (A) blood flow and velocity change in A1 and A2 in response to optical stimulation. The vertical lines specify the beginning and end of stimulation period. Blood velocity and flow are normalized to the baseline value (average of the corresponding data during the first 4 seconds of recording). (B) an example of flow and velocity response for control animal.

$$\frac{|B^1(z, x) - B^2(z, x)|}{b + |B^1(z, x)| + |B^2(z, x)|}, \quad (4.2)$$

where B^1 and B^2 are two B-scans recorded from the same cross section. The parameter b is a positive number that suppresses the noise when B-scans are very small and is empirically set to:

$$b = 2 \times \langle |B^1(z, x)| + |B^2(z, x)| \rangle_{(z,x)}, \quad (4.3)$$

In this equation, the operator $\langle \dots \rangle_{(z,x)}$ computes the mean value over z and x . The normalization cancels out the effects of inherent depth dependent sensitivity roll-off in SD-OCT imaging (78) and ensures that the dynamic range of all pixel intensities in an angiogram is limited to the interval between 0 and 1. To build a 3D volumetric angiogram, each cross section is scanned 10 times before moving to the next cross section providing 45 (combination of 2 out of 10) cross-sectional angiograms for each position. Average intensity for each cross-sectional angiogram is used as a noise and/or motion distortion measure and 10 angiograms which have the least distortion are selected and averaged to produce the final cross-sectional angiogram for that position. The cross-sectional images are then stacked to produce a 3D volumetric angiogram. A 3D blurring kernel is applied to the stack of cross-sectional angiograms to reduce the speckles before performing a 2D maximum intensity projection of the 3D angiogram.

4.3 Experiments

The optogenetic stimulation study was performed on 13 mice, five with a standard cranial window during a terminal procedure preparation and eight implanted chronically with a reinforced thinned-skull window (122) and (123). All animals produced similar results, al-

though only results from the latter group are reported here since their neural tissue showed reduced signs of cerebral edema and were more hemodynamically stable due in part to the thinned skull cranial window (124). Keeping a thin layer of bone on top of the brain not only prevents exposure of dura matter to air which reduces inflammation in comparison with standard cranial window surgeries, but also reduces intrinsic mechanical pulsations of the brain by maintaining intracranial hydrostatic pressure. For thinned-skull experiments, five transgenic *Thy1 :: ChR2/H134R - YFP* mice (ChR2) from Jackson Laboratories (stock number 012350) and three wildtype mice were used. The *H134R* variation of the ChR2 gene was chosen for larger photocurrents due to its slower closing kinetics (125). Along with the ChR2 mice, three wildtype mice were also used as control animals. In vivo experiments were approved and performed under the Institutional Animal Care and Use Committee at the University of Wisconsin - Madison. Each animal was implanted with a thinned-skull cranial window and glass coverslip (122) and given at least three days for recovery before imaging. During implantation, the mice were administered buprenorphine ($50 \mu\text{g}/\text{kgSC}$) and anesthetized with isoflurane ($1.5 - 2.0\%$ in oxygen). The scalp was retracted and the skull was fixed to a titanium plate and mounted to a fixed post. A $3\text{mm} \times 3\text{mm}$ area of skull was thinned and a 3mm diameter glass cranial window was installed. During SD-OCT imaging and scanning procedures the mice were anesthetized with Ketamine ($25 - 100 \text{mg}/\text{kgSC}$) and dexmedetomidine ($0.05 - 0.5 \text{mg}/\text{kgSC}$).

During imaging sessions, to optically stimulate the brain, a 473nm laser was pulsed at 15Hz delivering an average power of 18mW . The laser beam was focused onto a 1.7mm diameter spot for a calculated optical intensity of $\sim 8 \text{mW}/\text{mm}^2$. The hemodynamic response to the optical stimulation was monitored using 3D angiograms and 2D cross section velocity profiles.

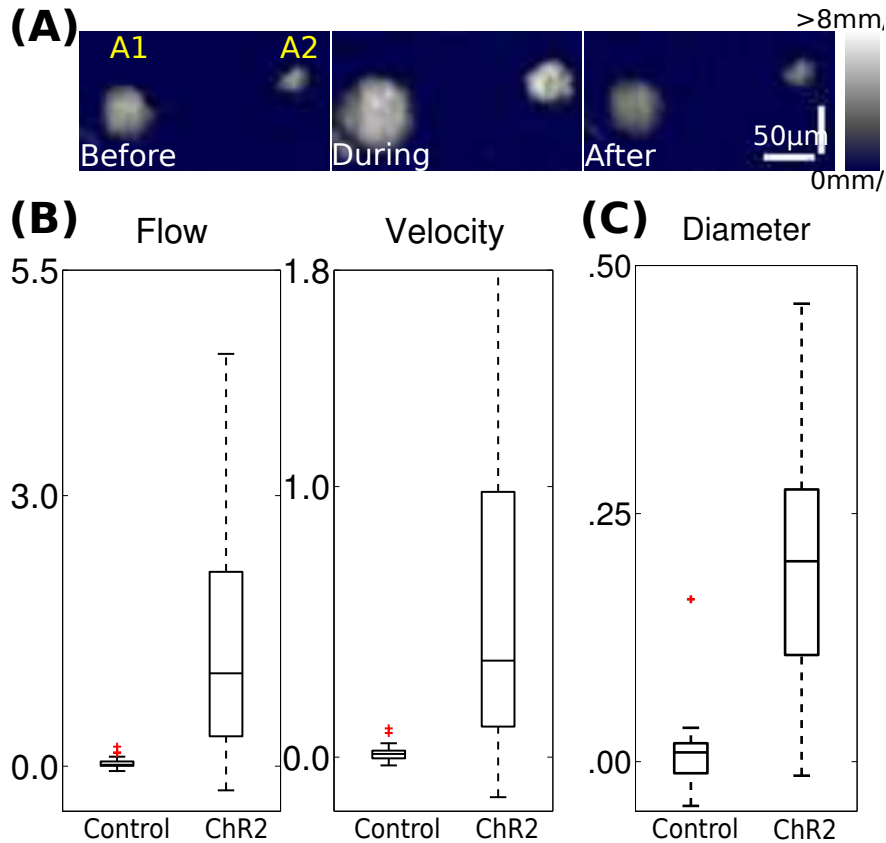


Figure 4.4: Hemodynamic response of transgenic mice compared with the control animals. (A) shows the velocity profile for A1 and A2, before (left), during (middle) and 22 second after (right) stimulation. To remove fluctuations the profiles were averaged over four seconds for each of the profiles. (B) shows fractional change in flow and velocity for control and ChR2 mice after 10 second of stimulation. (C) Quantitative comparison of fractional change in the vessel diameter after stimulation for three control and two ChR2 mice.

4.4 Results

To monitor the effect of stimulation on the vessel diameters, the field of view (FOV) was adjusted to include one branch of the MCA. Two consecutive 3D angiogram covering the same $2mm \times 2mm$ area were then recorded, one without and one with optical stimulation. To ensure repeatability and to validate the observed hemodynamic responses, this sequence was repeated at least two times for the wild-type animals and three times for the ChR2 mice within the same FOV for each animal. Fig. 4.2(B) shows an angiogram of one of the ChR2 mice where the red color represents areas in which vessel diameters were modulated

during the stimulation. Panels (C) and (D) in the same figure compare the angiogram of the smaller FOV (which is marked by a square in panel (B)) before and after optical stimulation, respectively. To quantify observed changes, segments of the main vessels were selected (red boxes in Fig. 4.2(C) and (D)) and the fractional change in the vessel diameter was calculated by averaging the fractional change along the vessel inside the box.

While three-dimensional angiograms reveal changes in the diameter of the blood vessels over a large area during optogenetic photostimulation, they do not provide high temporal resolution images to be used for quantification of the blood flow variations. To study rapid transitional changes in blood flow, we made 2D cross-sectional Doppler measurements of the main arteries and veins inside the FOV up to 45 seconds; four seconds of pre stimulation followed by 10 seconds of stimulation and 16 to 31 seconds of post stimulation. For the main vessels in the cross section, the normalized blood flow was calculated using the 2D Doppler data where the average of blood flow in the first four seconds was used as the baseline. Blood flow in each vessel was estimated by summing the velocity of all the pixels inside a bounding box surrounding the vessel's cross section. To relate this value with the actual flow, the vessel's angle with respect to the laser beam and the cross-sectional plane, as well as the voxel overlap, need to be known. However, assuming these parameters are constant over time, they will not affect the normalized blood flow. In addition to the flow, the maximum velocity for each vessel was calculated and then normalized to the baseline velocity. Maximum velocity in the vessel cross section was calculated by averaging the three pixels with the highest velocity inside the bounding box, which helped to reduce the noise level. A moving-averaging filter was then applied to the flow and velocity signals to suppress fluctuations caused by the heartbeat. We conducted 8 to 10 trials per mouse and averaged the result to reduce the effect of non-synchronous fluctuations in the velocity and flow. Both blood flow and blood velocity in ChR2 mice showed a rapid increase shortly after optical stimulation while wildtype animals showed a relatively flat response to stimulation. Examples of normalized flow and velocity from ChR2 mouse recorded from the MCA branches A1 and A2 (labeled

in Fig. 4.2(B)) are shown in Fig. 4.3(A). Panel (A) in Fig. 4.4 presents velocity profiles of these vessels before(left), during(middle), and after(right) stimulation. Each of the velocity profiles were averaged over the last four seconds within their respective durations. The velocity profiles for the vessels A1 and A2 show noticeable increases in the vessel diameter and blood velocity confirming the results indicated in Fig. 4.2(B) and Fig. 4.3(A). Similar changes were observed in most of the vessels we investigated in our study and the results show repeatable patterns of change in the blood flow and velocity in the ChR2 animals following the optogenetic stimulation. We had few discrete observations where we noticed minimum reduction in blood flow after optical stimulation.

The hemodynamics of five ChR2 mice and three control animals are summarized in Fig. 4.4(B) and Fig. 4.4(C). Fig. 4.4(B) compares fractional change observed in blood flow and blood velocity inside main vessels after 10 seconds of stimulation. For ChR2 animals, an average of 100% increase in flow and 35% increase in velocity were recorded whereas in control experiments the maximum change in flow and velocity were less than 10%. In these measurements, vessels with velocity out of the dynamic range of our SD-OCT were excluded. Fig. 4.4(C) presents the diameter changes in wildtype vs. ChR2 mice. With this method it was possible to observe, on average, more than a 20% change in the diameter of main cerebral vasculature for ChR2 mice and less than 1% change for wildtype animals. Moreover, our observations demonstrate that the intensity of hemodynamic response in ChR2 mice varies from vessel to vessel; however, in general larger fractional changes occurred in smaller vessels. Table I summarizes the numerical data for both control and transgenic animals. In this table, ΔF and ΔV are fractional changes in the blood flow and velocity, with respect to the baselines, 10 seconds after stimulation. The baseline for blood flow and velocity were obtained by averaging these values during a four second period before stimulation. ΔD in the table represents fractional change in the vessel diameter after stimulation with respect to the baseline diameter which was calculated from the three-dimensional angiogram recorded before each stimulation. During three-dimensional data acquisition, the stimulating light

pulses were applied over the whole period of the scan.

There are a few subtle points which are crucial in the analysis of these observations. In these experiments skull is not removed and only shaved to be as thin as about $50\mu m$ roughly. As a result the optical power drops significantly before reaching the brain tissue. Nevertheless, the irradiance, $8mW/mm^2$, in these experiments is comparable or in most cases less than what is prescribed in previously published literature. For example: Kanh *et. al.* (10) have reported irradiance of $300mW/mm^2$ at the tip of an unjacketed fiber with diameter of $200\mu m$ which translates to $9.4mW$ of optical power. Desai *et. al.* (17) have used $5mW - 10mW$ of blue light power (irradiance of $150mW/mm^2 - 300mW/mm^2$). The irradiance in Lee's manuscript is in the range of $85mW/mm^2$ (9). A comprehensive model to estimate the optical power required for optogenetic stimulation and prediction of light distribution in the brain tissue is presented in (126). The other important fact is that Doppler based velocimetry technique is not able to detect the lateral component of the blood velocity and what is measured in the OCT data is the axial component of the velocity. Therefore, the velocity and flow measurements are not the actual blood velocity and flow but proportional to these values. If we assume that the angle of vessel with respect to the scanning beam has not changed during the measurements, the OCT Doppler velocimetry can be used to detect fractional changes in blood velocity and flow. Srinivasan *et. al.* (99) have proposed a method to measure blood flow regardless of the vessel angle, but it requires three-dimensional velocity measurements which is time consuming and does not allow to achieve the high temporal resolution velocity measurements which are required in this study.

By definition, flow is the blood volume passing through the vessel's cross section. Therefore, any change in the blood flow is caused by the change in the vessel cross-sectional area and/or change in the blood velocity. In our measurements, we observed up to 2.7 times increase in velocity and up to 50% increase in diameter. As a result, we have observed up to $2.7 \times 1.5^2 = 6$ times increase in the blood flow. It is important to clarify that the diameter increase reported here is the lateral diameter. The axial size can increase more or less com-

Table 4.1: Fractional changes of hemodynamic signals in control and transgenic animals, (Wilcoxon test double sided p-values: $p_{\Delta F}, p_{\Delta V}, p_{\Delta D} < 0.036$).

Control	animal#1	animal#2	animal#3		
ΔF	0.0368	0.0108	0.0421		
ΔV	0.0148	-0.0009	0.0256		
ΔD	0.0263	0.0078	-0.0051		
Transgenic	animal#1	animal#2	animal#3	animal#4	animal#5
ΔF	1.8765	3.6960	0.8271	0.8289	0.4979
ΔV	0.6026	0.9885	0.3104	0.3403	0.3508
ΔD	0.2486	0.2772	0.1462	0.1987	0.1039

pared with the lateral size of a vessel. The average vasodilation we are reporting (20%) is comparable to the average dilation reported by Drew et.al. (17%) (19) in response to sensory stimulation which is measured via multi-photon fluorescence microscopy. In another observation, Radhakrishnan and Srinivasan reported (127) OCT measurements of vessel dilation in rats following electrical forepaw stimulation and observed 34.6% – 55.2% increase in the diameter of arteries which is comparable to our observation. Drew et. al. (19) also reported 81.8% peak velocity change during 30s of sensory stimulation in the capillaries with average size of 3.2 micron which is again in the range of our observation for the velocity increase after 10 second of optogenetic neuro-stimulation measured in capillaries of diameter 10 micron or higher. Therefore, based on this comparison, the scale of hemodynamic signals generated by optogenetic and sensory stimulation are reasonably close.

Compared with some previous studies, the hemodynamic reaction to optogenetic stimulation is stronger in our observations which can be justified if we appreciate the fact that:

1. We are using low irradiance, but more intense optical power exposing a larger area. Therefore, we stimulated a larger population of neurons which has translated to stronger hemodynamic response compared with the small local photo-stimulation conducted by other researchers, (13), (15),
2. Another determining factor is the difference between the variables

that are measured to monitor hemodynamics in our experiments versus other published reports. Optical and Doppler Coherence Tomography that are used in our experiments provide high lateral/axial spatial resolution. OCT is able to provide depth resolved velocity measurements. Its resolution allows to measure velocity of even single red blood cells. However, to provide a three-dimensional map, tremendous amount of data should be recorded which slows down the process compared with techniques such as LSI, IOS (13) or laser Doppler flowmetry (LDF) (15). Nonetheless, in comparison, SD-OCT is still a more powerful method. LDF inherently has low lateral resolution compared with OCT and only provides a rough estimation of the overall velocity change within the field of view. LDF is a useful device in measuring the blood perfusion inside a tissue volume, while OCT measures blood velocity inside each individual vessel. Therefore, direct comparison of the data can be misleading. On the other hand, IOS measures only the blood volume in the tissue and not the blood velocity. The IOS data can be more helpful if combined with blood flow measurements to develop a clear picture of changes in hemodynamics.

4.5 Conclusion

In this chapter, we presented a procedure to directly control neural activity by optical neurostimulation of cortex and monitor its impact on the hemodynamic signals in transgenic mice. Results of these experiments confirm that an increase in neural activity leads to vasodilation as well as increased blood velocity in branches of the MCA. Using reinforced thinned-skull windows allowed the animals to recover after surgery and also suppressed the potential brain pulsations during data recording; improving the quality of the images and precision of the measurements. Our observation showed minimal, often imperceptible, blood flow and velocity responses to optical stimulation in wild-type mice. This suggests that the observed changes in hemodynamics are mostly due to the increase in neural activity induced by optical stimulation. Further studies combining the SD-OCT and optogenetics will enable

a cell type-specific analysis of neurovascular coupling with high spatial and temporal resolution. This approach, with the addition of blood oxygenation imaging, could be used to create rich data sets for studying the blood oxygen level dependent (BOLD) signal in great detail. The current methods could provide new insights into neurological diseases involving cerebral vasculature such as epilepsy and stroke.

Chapter 5

Spatio-temporal characteristics of cortical vasodynamics

5.1 Introduction

The ubiquitously distributed vascular network of the brain is primarily responsible for the delivery of vital metabolic and respiratory substances to the cells and the removal of deleterious metabolic by-products to keep the tissue alive and functional. The regulatory process that controls the flow of blood in the vascular network is mainly influenced by the level of activity in the local networks of neurons which are the most energy demanding cells in the brain (128), (129). Consequently, the dynamics of the vascular network and neural circuitry of the brain are intimately tied. Understanding the mechanisms that mediate this coupling provides insight into the brain's information processing pathways and pathophysiology of neurological diseases in which neurovascular coupling is perturbed.

Neurovascular coupling has been studied at the cellular level by investigating the role of intermediary cells and the signaling mechanisms that relate changes in the level of neural activity to the local fluctuations of hemodynamic signals (130), (131), (132). In recent years, optogenetics, as a reliable means for direct modulation of activity in cell-populations of interest in a versatile yet minimally invasive manner (4), (3), has been employed to investigate hemodynamic response in brain tissue (e.g., (13), (18), (12), (133)). Uhlirova et al. used optogenetics to demonstrate the role of inhibitory neurons in arteriolar dilation and constriction. Moreover, they observed decrease in dilation onset and time-to-peak as the

arteriolar depth increases. In our previous work, we quantified multiple attributes of vascular response to wide-field optogenetic stimulation, and the timing and magnitude of vasodynamic reactions were measured ((134) and Supplementary Note 1). In Channelrhodopsin (ChR2) positive animals, we observed 20%, 35%, and 100% increases in diameter, blood velocity, and blood flow following photostimulation pulses, respectively. The corresponding changes were smaller than 10% in wild-type animals which rule out the significance of thermal effect (135), (136), (137) on the vascular responses.

Nonetheless, neurovascular coupling at the vascular scale has not been extensively investigated from the system engineering point of view. Studying the causal relation between an exogenous perturbation and cortical vasodynamics will further our understanding of the correlation between neural activity and local or global blood flow changes under healthy and pathological conditions.

In the current study, we propose a cohesive approach to discern different temporal and spatial aspects of vasodynamics following a perturbation in the level of local neuronal activity. We employ the new advances in photostimulation and imaging techniques to implement open-loop and feedback controllers which manipulate the flow of blood in large-scaled vascular networks of the brain. We demonstrate the ability of the proposed methods to investigate the effect of length and amplitude of stimulation on the temporal pattern of response in the blood flow, blood velocity, and diameter of the pial vessels, simultaneously. To understand the long-term or time varying aspects of the vascular system, which may not be evoked by a stimulus of a predefined short duration, we present the design and development of a closed-loop controller. This controller uses locally and temporally engineered optogenetic stimulation pulses to maintain the flow of blood at various user defined levels in a set of selected arteries.

Moreover, we offer systemic approaches to investigate the spatial characteristics of the dynamics in a vascular network by generating arbitrary spatial patterns of optical neurostimulation in the cortex of transgenic mice and monitoring the blood flow attributes in

the surrounding vessels. We defined a receptive field of a vessel which was originally defined for neurons and expanded it to a single vascular unit. This receptive field allows us to comprehend important aspects of spatio-temporal correlation between the vasodynamics and the nearby neuronal activity.

5.2 Results

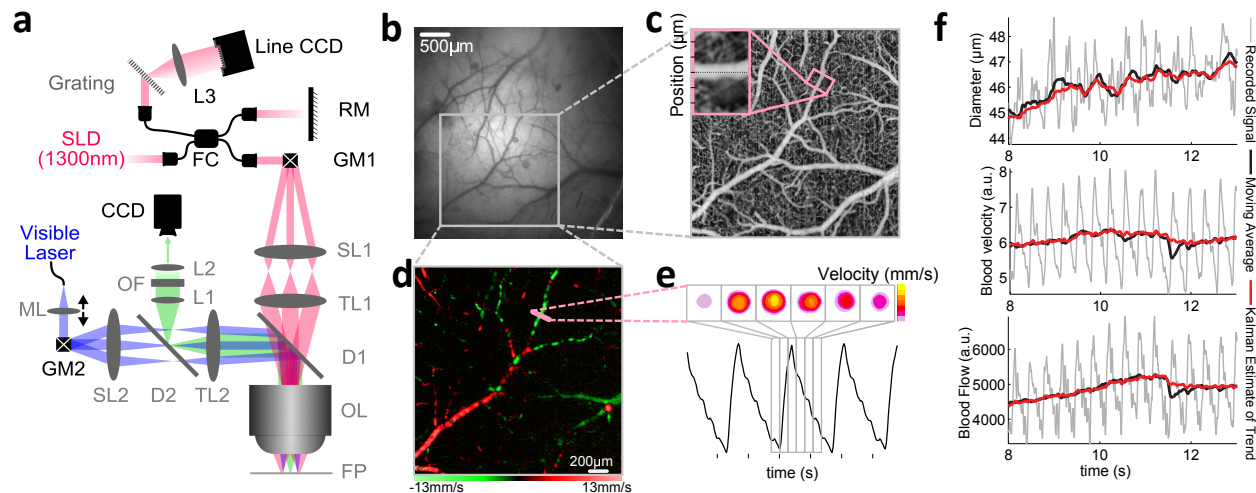


Figure 5.1: Simultaneous optogenetic stimulation and optical coherence angiography and velocimetry: (a) Schematic of the optical setup which integrates spectral-domain OCT, fluorescence imaging, and optogenetic stimulation. L: lens, ML: movable lens, SL: scan lens, TL: tube lens, OL: objective lens, FP: focal plane, GM: galvanometric mirror, FC: fiber coupler, SLD: superluminescent diodes, D: dichroic mirror, CCD: charge-coupled device, RM: reference mirror. (b) A typical fluorescence image captured from the cortical tissue of a Thy1-YFP+ transgenic mouse. (c) The maximum intensity projection of a 3D OCT angiogram obtained from a region of interest marked in the fluorescent image of panel (b). OCT angiograms are used to measure vessel diameters. (d) The maximum intensity projection of 3D Doppler-OCT measurement. (e) Snapshots of the Doppler velocity profile of a sample artery captured within a single heart cycle. By locating a bounding box which encapsulates the vessel cross-section and adding the value of all pixels inside the set, we obtain an axial blood flow index for the vessel at each time slot. (f) Examples of vessel diameter (top), blood velocity (middle), and blood flow (bottom) measurements from a typical cortical artery performed via OCT imaging. Diameter measurement time-traces are noisy since the lateral resolution of OCT angiography ($\sim 5\mu m$) is comparable to the percentage of the observed changes in vessel diameters. Heart pulsation directly affects all OCT angiography and Doppler measurements. The heart pulsation contamination was eliminated by the use of a moving average (MA) filter (black curve) or an extended Kalman filter (red curve).

All-optical interrogation of vascular response. For our experiments, we developed a spectral-domain optical coherence tomography (OCT) scanner (47), (48), (138) and extra components were integrated to simultaneously perform fluorescence imaging and patterned optogenetic stimulation (Figure 5.1.a, Online Methods). In the experiments, unless otherwise mentioned, the photostimulation was pulsed at $15Hz$ with 50% duty cycle (DC). The OCT scanner was programmed to capture three-dimensional angiograms (35), (37), (36), (100) or velocimetric images (40), (82) of any predefined region of interest (Figure 5.1.c, d) or to just periodically monitor cross-sections of a set of target vessels (Figure 5.1.e).

Periodic OCT scans are performed to generate two separate measurements. First, cross-sectional angiograms are obtained to compute temporal changes in diameters of vessels (Online Methods). In the second step, Doppler images are reconstructed to extract quantitative measures of blood flow and blood velocity indices. The velocity and flow indices are defined as the maximum and the integration of all velocity values across the vessel lumen, respectively (Online Methods).

Figure 5.1.e displays snapshots of such Doppler velocity measurements and the corresponding blood flow values which are sequentially acquired within one cardiac cycle in a typical cerebral artery (Online Methods). As illustrated, blood flow and velocity measurements are contaminated by the heart and respiration pulsations. Also, the diameter of arteries exhibit some spontaneous fluctuations in the spectral range from $0.1 - 1.0Hz$ (19). To discern any changes in the vasodynamics caused by neurostimulation, it is essential to at least remove the effect of cardiac (and even respiratory) pulsations from the recorded traces. Cardiac induced alternations are sometimes an order of magnitude larger than other physiological sources of fluctuations. It is possible to readily remove the contribution of smaller terms by repeating the experiments and performing ensemble averaging over a sufficient number of trials. On the other hand, cardiac and respiration components are usually attenuated by using a moving-average (MA) filter as displayed in Figure 5.1.f. The performance of the MA filter further improves when we use the length-locked moving-averaging in which the

filter window size is continuously adjusted according to the cardiac period (Supplementary Note 2). In more delicate experiments, it is better to use advanced mathematical algorithms such as the extended Kalman filter (EKF) ((139), Supplementary Note 3).

Spatial-temporal configuration of photostimulation. We employed a Monte Carlo simulation code (Online Method and references (126), (140) and (141)) to model light distribution inside the brain when the optical power is delivered to a spot on the surface of the tissue. We used the simulation code to estimate the volume of activation (VoA) when the irradiance threshold for effective activation of ChR2 molecules was adjusted at $1mW/mm^2$ (142). Based on this analysis, when the same light intensity is delivered to a larger area, the corresponding VoA is wider but shallower (Figure 5.2.a). Simulations show that the VoA is a semi-linear function of the light intensity (Figure 5.2.b and Supplementary Figure S5)); however, when the intensity is constant, changing the diameter of the illuminating spot, from $266\mu m$ to $800\mu m$, had no significant impact on the estimated VoA (Figure 5.2.c). To demonstrate this observation in practice, we studied the effect of light intensity and illumination spot size on the evoked vascular response *in-vivo*. We observed a strong correlation between the blood flow response (BFR) and the light intensity, or equivalently, the VoA. Meanwhile, increasing the diameter of the illuminating spot from $266\mu m$ to $800\mu m$ did not cause any significant change in the blood flow (Figure 5.2.e to g) or blood velocity responses (Supplementary Figure S6.e). The magnitude of the vascular response was quantified by averaging the percentile changes in the blood flow within the interval starting at the stimulation onset and extending for $20sec$. The traces of blood flow show a rapid response following the stimulation onset and a prolonged tail which extends to over $20sec$ after stimulation for intense stimulations of $4mW$ and $5.7mW$ ($n = 1$ vessel)(Figure 5.2.e and Supplementary Figure S6.b,c).

The length of stimulation had similar impact on the shape of the evoked BFR. To assess the effect of stimulation duration, we conducted a set of experiments in which we kept the

photostimulation pulses constant ($I = 5.7mW$, $W = 800\mu m$, $Freq. = 15Hz$ and $DC = 50\%$) but we changed the duration from $1sec$ to $12sec$ as we simultaneously monitored the cross-sections of three vessels marked in Figure 5.2.h. Out of these three monitoring sites, two cross-sections (sites 1 and 2) were selected to be on the main branches of the middle cerebral artery (MCA) while the third site was on a daughter branch of vessel 2 and this vessel is feeding the area farther away from the stimulation location.

For vessels 1 and 2, which are feeding the nearby regions, the amplitude and duration of the flow and velocity responses increased as a function of the stimulus duration (Figure 5.2.i). The duration of response was calculated as the period over which the flow response stays above 20% of its maximum (Figure 5.2.j). For stimulus durations of $1sec$ and $2sec$, the response lasted for about $26sec$ and above that the duration of response increased almost linearly with the duration of stimulation (Figure 5.2.k). For short durations (i.e., $1sec$ and $2sec$), the shape of the BFR at site 2, which is closer to the stimulation location, can be described as a strong fast peak followed by a second relatively weaker and slower peak. When the duration of stimulation was increased beyond $4sec$, the slower peak became stronger and at stimulation durations of $8sec$ and $12sec$, the second peak evidently merged with the first one (Figure 5.2.i and j).

The blood flow at the third monitoring site remained flat after stimulation; however, velocity dropped (the rightmost diagram in Figure 5.2.i) ($n = 1$ animal). The drop in the velocity is potentially a side effect of the vessel dilation which retro-propagated from the point of stimulation to this cross-section (143), (144), (145).

Vascular receptive field. Previous experiments proved that each individual vessel potentially responds differently to the same stimulation pulse depending on the relative position of the vessel and the site of photostimulation. To further study this dependency, we conducted experiments in which photostimulation pulses ($6sec$ duration, $Freq. = 15Hz$, $DC = 33\%$, $I = 5.7mW$, and $W = 461\mu m$) were delivered at multiple discrete locations (25 locations in

a 5 by 5 matrix) across the field of view. We analyzed the evoked vascular response in a set of four arteries which are the main branches of the MCA (Figure 5.3.a).

Generally, stimulations in the close proximity of a vessel evoked a biphasic BFR in the vessel. As the stimulus was moved away from the vessel, the response attenuated. The BFR data was used to produce a map which demonstrated the spatial tie between the flow dynamics in a vessel and the activity in the nearby tissue. The value of each pixel in this map represents the percentile change in the blood flow of the vessel in response to the optogenetic stimulation delivered to the position of that pixel (Online Methods, Figure 5.3.b). This map conceptually resembles the receptive field (RF) of a neuron. In this example, vessel 2 showed the largest flow response (54%) among the vessels. The peak in the response happened when photostimulation pulses were delivered right on top of the vessel and dropped quickly as the spot moved away from that position. The size of the RF for vessel 2 was estimated by fitting a two-dimensional Gaussian function to the image. The standard deviation of the fitted Gaussian along and perpendicular to the vessel were $\sigma_{along} = 734\mu m$ and $\sigma_{perp} = 539\mu m$, respectively (Supplementary Figure S10). As we expected, the most sensitive part of the RF is in the vicinity of each vessel's feeding territory.

The RFs of vessels provide a systemic approach to predict the behavior of each vessel and the correlation between different vessels when the network responds to some form of neurostimulation. For instance, vessel 1's blood flow drops in response to stimulation on the right side of the field of view. Figure 5.3.c shows the RF of all four vessels at the instant when the largest drop in the blood flow of vessel 1 was detected ($t = 5sec$). Based on this data, the area where photostimulation induces some negative flow response in vessel 1 overlaps with the area that causes dilation in the same vessel. Our previous observation in Figure 5.2.i have already showed that the traces of blood velocity and blood flow can be different when responding to the stimulation. The new observations re-establishes that blood velocity, blood flow, and vessel diameter (Figure 5.3.c, Supplementary Figure S2, and Supplementary Figure S8) are three different aspects of the vascular response. The RF maps

demonstrate that increase in blood velocity and flow in response to stimulation at the vicinity of a vessel is mostly local. Nevertheless, the same maps demonstrate that the stimulation location which induces maximum flow response might differ from the one causing maximum change in the velocity. In contrast to the velocity and flow maps, the RF for the diameter response (Supplementary Figure S2.b) reveals that a stimulus close to a branch may cause dilation in some other down- or up-stream branches which may be far from the stimulation location. For example, the stimulation which dilates vessel 2 also causes dilation in vessel 1. This can explain the difference between blood flow and blood velocity receptive fields since the flow and velocity in a vessel are coupled variables determined by the vessel diameter (Supplementary Note 4).

Simultaneous multi-site photostimulation. Characterizing the response of the vascular network to simultaneous multi-site stimulation based on the response of the same vessel to individual stimulus is an important step in developing network blood flow controllers. Previously, receptive fields of vessels were obtained by applying one stimulus at a time and scanning the position of stimulus across a desired area. However, the vascular response to multiple simultaneous stimulations was not investigated. Our strategy for this study was to conduct a sequence of experiments to individually measure the vascular response to two stimulations which are delivered at separate locations. Then, use this information to predict the vascular response when stimulation pulses of similar or different magnitudes are delivered simultaneously to the same sites and confirm the results experimentally. To conduct these experiments, we selected three branches of the MCA in a transgenic mouse where two selected vessels (branch 1 and 2) were daughter branches of the third parent vessel (Figure 5.4.a). Stimulation locations were selected such that applying stimulation at each site predominantly induces activity in one daughter branch while the other daughter branch responds minimally (Figure 5.4.a-d).

Following the designed strategy, we recorded three data sets corresponding to three dif-

ferent stimulation scenarios. In the scenarios 1 and 2 (Figure 5.4.a,c), stimulation pulses ($I = 4.7mW$, $D = 4sec$, $Freq. = 15Hz$, $DC = 32\%$, $W = 461\mu m$) were delivered to sites 1 and 2, respectively, while the BFRs in all the three vessels were recorded. In the third scenario (Figure 5.4.e) the photostimulation was time shared between sites 1 and 2 by using the fast galvanometric mirrors (stimulation at each site: $I = 4.7mW$, $D = 4sec$, $Freq. = 7.5Hz$, $DC = 16\%$, $W = 461\mu m$). Therefore, each site was receiving half the power delivered to the sites in the previous scenarios.

To compare BFRs in vessels under different stimulation configurations, we calculated the temporal average of the blood flow over a period of $60sec$ after the stimulation onset. In each stimulation scenario, the summation of blood flow increase in daughter vessels equaled the flow increase in the parent vessel. This result is graphically illustrated in Figure 5.4.g. Error bars in this diagram show the standard deviation of the data for different trials for each scenario (minimum of 4 trails). Stimulation sites 1 and 2 were chosen to be close to the feeding territory of vessels 1 and 2, respectively. As a result, we expected to detect larger response to photostimulation in vessel 1. Similarly, vessel 2 was expected to be more responsive to stimulation at site 2 which was confirmed in the experiment. After applying the photostimulation at site 1, the amount of blood flow increase in the parent vessel and daughter branches 1 and 2 were 672 ± 76 (arbitrary unit (au)), 483 ± 169 (au), and 216 ± 457 (au) (mean \pm Std), respectively. Stimulation at site 2, generated 605 ± 258 (au), 327 ± 171 (au), and 405 ± 184 (au) change in blood flow in the same vessels. The weighted average of the responses predicts a blood flow increase of ~ 639 , ~ 405 , and ~ 311 (au) for the parent vessel and the branches 1 and 2 during the third scenario, respectively. The actual measurements for blood flow increase were 637 ± 188 (au), 372 ± 109 (au), and 289 ± 100 (au). Our observations match the prediction based on the linear superposition of responses to individual stimulation. Based on this data, we hypothesize that the vascular network behavior is spatially linear to the extent that the response to a set of stimulations can be estimated fairly by the superposition of individual responses.

Closed-loop blood flow controller. To illustrate the power of optogenetics in manipulating the flow of blood in the brain tissue, we implemented a Proportional-Integral-Derivative (PID) closed-loop controller which strives to adjust and maintain blood flow in any target artery(ies) at a user defined set point by tuning the duty cycle of stimulating light pulses ($I = 5.7mW$, $Freq. = 15Hz$, $W = 800\mu m$) (Figure 5.5.a). In the designed tests, the closed-loop control process was engaged for $240sec$, preceded by $30sec$ of baseline and $60sec$ or $90sec$ of post-stimulus recordings (Figure 5.5.b and Supplementary Note 5). The average of flow during the baseline period was used as a reference to calculate relative changes in the blood flow. A length-locked MA or EKF filter (Supplementary Notes 2 and 3, Supplementary Figure S11) was used to attenuate the cardiac and respiratory components in the recorded data.

The error signal was defined as the difference between the desired and measured percentile increases in the blood flow. In this configuration, the proportional (KP), integrating (KI), and derivative (KD) gains are the variables that translate the error signal to the stimulation pulse duration. These variables were tuned ($KP = 3.1$, $KD = 25$, and $KI = 1.5 \times 10^{-3}$ or $KI = 7.5 \times 10^{-3}$) to produce a near to critically damped flow response in branches of MCA when the desired blood flow was set to 15% above the baseline (Supplementary Note 6). The experiment was repeated in three separate animals using the same values for the PID controller and similar closed-loop performances were achieved. Based on this observation, at least for the MCA and its main branches, the same values can be used without the need for readjustments. By repeating the experiment we noticed that the closed-loop mechanism can readily lock on blood flow increase percentages of 5%, 10% and 15%. In one animal, we even tested larger changes up to 25% and still desired response was achieved. As we increased the desired set point further, the time-averaged pulse width (actuator value) as well as the time-averaged error between the set point and the output also increased as displayed in Figure 5.5.d. The zoomed-in window in this figure captures the close relation between the flow and stimulation pulse width for a few selected trials. Whenever some drop in the blood flow is

detected, the controller increases the pulse width, which helps rise the blood flow back to the desired set point rapidly.

5.3 Online Methods

Animal Preparation All animal procedures were approved by the University of Wisconsin-Madison Institutional Animal Care and Use Committee (IACUC). We used 6 to 14 weeks old transgenic mice (Thy1::ChR2/H134R-YFP) for this study. Each animal received a thinned-skull cranial window and a glass coverslip (122) and the brain was imaged during a single terminal session. During preparation, the mice were anesthetized with isoflurane (1.5 – 2.0% *in oxygen*) and were administer 0.25mL of fluids (sterile Saline solution 0.9%) and Dexamethasone (2mg/kg). In each animal, the scalp was retracted and the skull on top of the somatosensory cortex was thinned over an area of 3mm diameter. A 3mm diameter coverslip was installed. The anesthetic was switched to Ketamine (25 – 100 mg/kgSC) and dexmedetomidine (0.05 – 0.5 mg/kgSC) prior to imaging.

System detail. The spectral-domain OCT scanner uses a low coherence light source (central wavelength 1300nm, bandwidth > 170nm, total power 10mW) which provides an axial resolution of $\sim 4.4\mu m$ in air. The objective lens is a telecentric lens system with the effective focal length of 18mm, a field of view of 5mm in diameter, and magnification of 10 \times (LSM02, Thorlabs, New Jersey, USA). In conjunction with an OCT collimated beam of diameter 3.4mm, it gives a spot with diameter of $\sim 5.1\mu m$ (134). The beam was transferred to the objective by using a scan/tube lens mechanism which opens up the space at the back focal plane of the objective (77). This space was used to install a dichroic beamsplitter to combine the OCT and visible light beam pathways. The visible path is used to deliver optogenetic stimulation pulses and/or fluorescence excitation light. The same path is also used to capture fluorescence or bright field images. The dichroic beamsplitter in the visible path (FF440.520, Semrock) passes the excitation/stimulation blue light toward the objective

lens and reflects the emitted green light toward a CCD camera (EXi Aqua, QImaging, BC, Canada). The camera is used to visualize the location of stimulation and to capture images of pial vessels in the cortex. When necessary, this imaging path can be used for calcium imaging, NADH recording, etc. Spatial distribution of photostimulation in this setup is independently controlled by exploiting a separate set of galvanometric mirrors to steer the beam of a fiber-coupled visible laser ($\lambda = 450nm$, $I \sim 20mW$, LP450-SF15, Thorlabs, NJ, USA). The spot size of the laser on the tissue was tuned by adjusting the position of the collimating lens to achieve illumination disks of diameters changing from $266\mu m$ to $800\mu m$. For multi-site stimulation, we used time intervals between consecutive stimulating pulses to reposition the galvanometer and steer the beam to a new location. The CCD camera in the optical path of fluorescence microscopy was also used for bright field imaging to visualize pial vessels during experiments, mark the main vessel cross-sections for OCT imaging, and to guide the laser beam for optogenetic stimulation (Figure 5.1.b).

The OCT scanner is capable of recording up to 80K A-scans per second. For Doppler measurements, we use a spatial sampling interval of $0.5\mu m$ between A-scans. The system was programmed to periodically target multiple vessel cross-sections with arbitrary directions. For vessels smaller than $100\mu m$ in diameter, it takes $200/80000s = 2.5ms$ to capture each cross-section. This speed allows monitoring the cross-sections of up to 10 vessels at a rate of 40 fps. The maximum heart rate that we have in our data is less than $240bpm$ (or $4Hz$). Therefore, 40 fps is sufficient to avoid aliasing that is potentially caused by up to the fifth harmonic of heart rate induced blood fluctuations in our data (Supplementary Figure S4). However, the typical heart rate of a healthy young mouse under Ketamine-Xylazine low dose of anesthetic is $< 375bpm$ ($6.25Hz$) (146) and (147). By considering this heart rate as a design parameter, the maximum number of vessels that we can monitor is 6. In a different study, the heart rate under a general anesthesia was reported to be less than $450bpm$ ($7.5Hz$) (148) which limits the number of vessels to be monitored to 5.

We use a bidirectional scanning mechanism, in which we record the OCT data in both

forward and return paths of the galvanometric mirrors when scanning a vessel cross-section.

Doppler OCT velocimetry and flowmetry. We use phase resolved Doppler OCT (40) to obtain velocity profile of the desired vessels. Structural heterogeneities in the tissue can cause artifacts in phase information and introduce a bias to the Doppler OCT velocimetry data. This distortion can be avoided by using a bidirectional scanning mechanism and averaging the velocity profiles of forward and return paths. The structural noise in the forward and return paths of the galvanometric mirrors are additive inverse of each other.

In this work, we were alternating the direction of scanning constantly. Therefore, by averaging every two frames, we could remove the structural artifacts in our Doppler measurements. We apply a moving average of size $3 \times 7 \times 2$ (zxt) to bidirectionally scan velocity profiles to reduce the structural artifacts and measurement noise prior to any further processing. By locating a bounding box which encapsulates the vessel cross-section (Figure 5.1.e), and summing the velocity values for all the pixels inside the bounding box, we obtain an axial blood flow index of the vessel at each point in time. The relation between the actual flow and the measured flow index is influenced by the OCT voxel size, the overlap between voxels, the angle of the vessel with respect to the OCT beam etc. When we have no change in the configuration of the system or the physical orientation of the vessel during the experiment, the relative fluctuations in the OCT flow index reflects relative changes in the actual blood flow in the vessel (134).

The BFR in this work is defined as a percentile change in the blood flow index with respect to the baseline flow index. The heart pulsation was removed by applying a MA or an EKF filter. Since we report the BFR as a relative value, it is insensitive to scanning parameters and the physical orientation of the vessel. To detect the stimulation evoked flow response, the Doppler OCT measurement was performed for a period of at least 40sec. The OCT recording started prior to an stimulation onset. This period is referred to as the baseline period which was changing between 4sec to 30sec in different experiments. The

baseline flow was calculated by averaging the flow signal during the baseline period. Then, the percentile blood flow response was calculated by: $BFR(t) = 100 \frac{F(t) - F_B}{F_B}$, where $F(t)$ is the flow signal at time t and F_B is the baseline. This measurement was repeated at least five times and the results were averaged to achieve a reliable measurement in each experiment. A short baseline period reduces the length of each trial, but at the expense of higher biological noise in the baseline value measurement; which prescribes more number of recordings to achieve a reliable response measurement.

The blood velocity response (BVR) was measured by a similar approach. First, we defined a velocity index which is maximum/minimum velocity inside the bonding box when blood flow value is positive/negative. The velocity signal represents the fluctuations in the axial blood velocity. Then, the percentile blood velocity was calculated by: $BVR(t) = 100 \frac{V(t) - V_B}{V_B}$, where $V(t)$ is the velocity signal after pulsation removal at time t and V_B is the baseline value for the velocity.

Vessel diameter response. In vessel diameter measurements, we used OCT angiography which relies on the motion contrast to visualize moving particles in the tissue. Details of OCT angiography is presented in (134), which is based on a phase-sensitive OCT angiography technique (100). Briefly, we used a memory buffer with the size of eight images. At each point in time, the buffer was storing the most recent cross-sectional OCT images that were captured from the vessel cross-section. We compensated the effect of motion as described in (134). For any couple of randomly selected images from the buffer, we obtained a normalized difference measured by: $\frac{|B^1(z,x) - B^2(z,x)|}{b + |B^1(z,x)| + |B^2(z,x)|}$, where B^1 and B^2 are the selected OCT images and $b = 2 \times \langle |B^1(z,x)| + |B^2(z,x)| \rangle_{(z,x)}$ is a positive number that suppresses the noise when OCT signal is weak. The depth and lateral location across the OCT image are shown by z and x . The operator $\langle \dots \rangle_{(z,x)}$ computes the mean value over z and x . By processing this normalized difference for every possible permutation of selecting two OCT images from the buffer, we obtain 28 motion contrast images among which four of them with the least

amount of noise were averaged to obtain the vessel angiogram at that moment (134). We apply a maximum intensity projection (MIP) and calculate the FWHM of the MIP signal to estimate the vessel diameter.

To obtain the MIP of an angiogram, we first apply a smoothing filter of size 3×3 pixels (depth and lateral) to the angiogram to reduce noise. Then, at each lateral location, the average of the largest 5 values across the depth is obtained and assigned to that location in the MIP image. The vessel diameter response (VDR), defined by the percentile change in the vessel diameter after the heart pulsation removal, was then calculated similar to BFR measurements.

Since OCT angiography is based on motion contrast, the measured value of vessel diameter might differ from the actual diameter of vessel lumen. With some other imaging modalities such as multi-photon microscopy it is possible to image vessel lumen and measure lumen diameter. Therefore OCT and multi-photon microscopy diameter measurements might report slightly different diameter responses. Such a comparison between measurements in different modalities can be valuable for interpretation of diameter responses that are observed via OCT angiography.

Light distribution. Light distribution in the brain of animals was estimated by a 3D voxel-based Monte Carlo simulation (126), (140), and (141). The bulk of the tissue in the simulation had the size of $5 \times 5 \times 5mm^3$ (xyz) with a voxel size of $20 \times 20 \times 20\mu m^3$ and a total number of 5×10^6 photon packets were used. The brain tissue was assumed to be homogeneous with the optical properties of whitematter at $450nm$. The optical properties were set to $1mm^{-1}$, $55mm^{-1}$, and 0.9 for absorption coefficient (μ_a), reduced scattering coefficient (μ_s), and anisotropic factor (g), respectively (141). The brain surface was illuminated by a beam which had the numerical aperture (NA) of 0.1. The simulated beam had a uniform light distribution across its waist, with three different waist diameters of $W = 266\mu m$, $461\mu m$, and $800\mu m$.

Grid Stimulation To measure the receptive field of a vessel, we applied optical neurostimulation at different locations across the desired area, and measured the blood flow responses in the vessel. We chose 25 stimulation locations (Figure 5.3.A) where the center of stimulation sites were placed on a 5×5 lattice. The separation between stimulation locations was $400\mu m$ (center-to-center). The stimulation consisted of $6sec$ of a $15Hz$ blue laser pulse train with a pulse width of $21.3ms$, which was applied to a surface spot of diameter $461\mu m$ at the desired location. The continuous wave (CW) light power on the tissue surface was $5.7mW$. For each stimulation, we recorded vasodynamics in the selected vessels for $71sec$, which consisted of $15sec$ of baseline, $6sec$ of intra-stimulation, and $50sec$ of post-stimulation recording. The recording was done simultaneously for four cross-sections which are marked in Figure 5.3.A. The software was customized to produce a $10sec$ silent time or longer after each recording. The automated software was designed to go through all stimulation locations in a randomized order. This randomization helps to minimize the effect of time and order of stimulation on the evoked response. After recording a set of data, there was 1 to 30 minutes gap before the start of the next recording cycle. We repeated the set of recordings five times and results were averaged for each vessel and each stimulation location. Recording of each set took approximately 40 minutes and to finish all five sets, including the break between the recording sessions, the process takes about 4 hours.

To monitor multiple vessels simultaneously, the OCT system was recording at the speed of 80K A-scans per second. The cross-section of each vessel was covered by 200 A-scans, and took $2.5ms$ to obtain one cross-section. Then, the system moved the galvanometric mirrors to the location of the next vessel gradually in about $1.5ms$. The system repeated the same procedure to scan all desired cross-sections sequentially. After scanning the last vessel, it moved the galvanometric mirrors to the first cross-section and periodically visited all four vessel cross-sections. Therefore, the cross-section of each vessel was sampled every $4 \times (2.5ms + 1.5ms) = 16ms$ ($62.5Hz$). The gradual movement of mirrors between the vessel locations was necessary to reduce mechanical vibrations in the OCT head compartment.

Small mechanical vibrations that are caused by sudden movement of the rotatory components can increase artifacts in Doppler measurements which affects the accuracy of velocity calculations.

Calculating a receptive field. To obtain the flow receptive field (RF) of a vessel, first we found the stimulation site that results in the highest increase in the blood flow among all 25 locations. The time at which the blood flow response peaks (t_{max}) for that location was recorded. Then, the amount of response in each of the 25 signals at time t_{max} was calculated and assigned to its corresponding stimulation location. These values are marked with the circles in the signals in Figure 5.3.b. This provided a 5×5 pixels image. We interpolated this image to a 255×255 pixel colorcoded image. The concept of RF of a vessel can be extended to a time varying field, in which the the dynamic field at time t is formed by using the blood flow response at time t .

The velocity or diameter receptive fields can be obtain in a similar fashion by using the velocity or diameter responses, respectively. Examples of Time-lapse images of the dynamic receptive fields are presented in Supplementary Figure S7.

5.4 Supplementary Materials

Supplementary Note 1: Wide field optogenetic stimulation.

In our early studies , we used a 473nm blue laser (pulsed at 15Hz, 50% duty cycle, duration of 10 seconds, stimulation area $2.7mm^2$, and delivered power 18mW) to induce neurostimulation in the cortex of Thy1 transgenic mice ((134)). A widespread increase in the vascular diameter, blood velocity, and blood flow of various degrees was observed across the field of

view (Figure S1.a-d). In Figure S1.a, the red color next to each vessel marks the observed changes in the OCT angiogram following an aforementioned stimulation. Figure S1.c, and d show the maximum intensity projection of blood velocity before and after stimulation. Elevation in blood velocity caused noticeable increase in the brightness of the vessels across the field of view. For the 6 vessels marked in Figure S1.a, we also measured the transient responses of blood flow and velocity which are displayed in Figure S1.e and f, respectively. Based on this data, changes in blood flow and velocity appear within a second following the simulation onset. Displayed traces are generated by averaging the measurements for a minimum of eight trials while shaded areas around each curve show the standard deviation of the recorded data. Since the blood flow in each vessel is proportional to both vessel cross-section and blood velocity, blood flow responses are numerically larger than blood velocity responses in the same vessel.

Increase in the blood velocity at the center of selected vessels, as well as the expansion in vessel profiles are illustrated in Figure S1.g. There are three diagrams for each vessel in this panel. The top diagram shows the evolution of the maximum velocity projection in each vessel. In this diagram, the horizontal axis represents time, the vertical axis is the lateral position across the vessel, and the intensity of each pixel is correlated to the maximum velocity along the depth at that location. The solid black line marks the duration of stimulation. Graphs in the middle show the cross-sectional velocity profiles of each vessel for pre-, intra-, and post-stimulus time periods. Each velocity profile was obtained by averaging Doppler measurements during a period of $4sec$ which are marked by the tiny horizontal lines in the top diagrams. Graphs at the bottom of Figure S1.g display the blood velocity profile within each vessel and the relative changes caused by the stimulation. Since the maximum velocity occurs at the center of a vessel, the relative change is also maximum around the center. On average, in about $26sec$ after stimulus offset, the velocity returns to the level close to the baseline.

Control experiments were conducted in three wild-type mice and results were compared

to the data acquired from five transgenic mice (Figure S1.h). For the MCA branches of transgenic animals, we observed 20%, 35%, and 100% increase in diameter, blood velocity, and blood flow following the delivery of photostimulation pulses, respectively ((134)). In contrast, corresponding changes were smaller than 10% in wild-type animals which rules out the significance of thermal effect or other light-cell interactions that can potentially contribute to the observed hemodynamic responses in the brain of live naive animals ((135), (136), (137)).

Supplementary Note 2: Length-locked moving-average (LL-MA)

We used a first-order averaging filter to smooth the flow signal and remove the periodic heart pulsation. The heart pulsation is the strongest periodic signal that is interfering with the flow measurements. For efficient rejection of cardiac component, we locked the length of the moving average window (N) to be equal to five cardiac cycles:

$$N = 5T_cF_s. \quad (S1)$$

The duration of cardiac cycle is represented by T_c , and F_s is the sampling rate which equals the OCT frame rate (82 fps). At each point in time, the value of T_c was calculated via frequency analysis of the most recent 5sec of blood flow recordings. The frequency of the strongest component in the frequency range of typical mice heartbeat (3Hz to 9Hz) was considered as the cardiac frequency. The filtered value at each time index n was defined as the weighted average of the previous finite samples:

$$f[n] = \frac{1}{N_n} \sum_{i=1}^{N_n} f_{raw}[n-i], \quad (S2)$$

where f and f_{raw} are the smoothed and raw blood flow values, respectively, and n is the current index. The subscript n for N is used to show the time varying nature of this variable.

Supplementary Note 3: Extended Kalman Filter (EKF) for removing heart and breathing artifacts

In this research, we strived to control the blood flow in a selected vessel(s), using a closed-loop system, by manipulating local neural activity. It is shown in the manuscript that direct brain stimulation leads to some increase in the flow of blood in vessels in the region, which is considered as an indirect way of manipulating the blood flow in the brain. However, arterial blood flow in cerebral cortex is modulated by several other factors, including heart pulsation and respiration pattern. The amplitude of cardiac and breathing blood flow modulation can be larger or comparable to the level of evoked hemodynamic response and can affect the accuracy of the closed-loop blood flow controller. Therefore, these sources of blood flow modulation, which are independent of neurostimulation, should be estimated and removed from the measured blood flow before implementing a closed-loop controller.

In this work, we employed two methods to remove heart pulsation and respiratory pattern from the blood flow. The first approach was based on a length-locked moving average filter. In the second approach we used an extended Kalman filter (EKF) which is known as a robust method of estimating and rapidly tracking changes in the state of a system. Compared to the MA filter, the EKF is computationally more demanding and the existence of a state-space model is essential for successful implementation of the algorithm. Nonetheless, it is proven that the EKF can simultaneously track multiple parameters and provide valuable predictions. By utilizing the EKF, it was possible to decompose the measured blood flow to its fundamental elements, including cardiac and respiratory harmonics and a slow varying trend which was mainly affected by the level of local neural activity. The design of the extended Kalman filter that we used in this research is discussed in the following.

The extended Kalman model requires the signal to be formulated by two equations: a state model and an observation model. The state model relates the state variables at the time step $n + 1$ to the state at the time step n plus the process noise:

$$x[n + 1] = f(x[n]) + u[n],$$

where f is a function of the state variables and u is the noise of the covariance Q . The observation model estimates the measurement, $y[n]$, based on temporal values of state variables:

$$y[n] = h(x[n]) + v[n].$$

Here, h is a function of state variables and v is the measurement noise of variance r .

To model blood flow in cerebrovascular system of rodents, we adopted a model from the original work of McNames and Aboy ((139)) in which they were studying hemodynamics in human. In their model, hemodynamic signal (y) is composed of four main components: a slow-varying trend (m), a quasi-periodic respiratory term (y_r), a quasi-periodic cardiac term (y_c), and a term that accounts for amplitude modulation of cardiac term with the respiration ($y_p \times y_c$). We ignore the latter term in our model since we are monitoring blood flow and in our measurements we did not find any evidence that the modulating term has a major role in the blood flow fluctuations. Therefore, our measurement model was simplified to: $y[n] = y_c[n] + y_r[n] + m[n] + v[n]$.

The cardiac signal is modeled by a summation of multiple harmonics:

$$y_c[n] = \sum_{k=1}^{N_c} a_c(k, n) \sin(k\theta_c[n] + \phi_c[k, n]), \quad (\text{S3})$$

where N_c is the number of harmonics that are used to model the heart pulsation pattern (4 in our case). θ_c is the instantaneous phase which depends on the cardiac angular frequency (ω_c) and the sampling period (T) that is calculated by: $\theta_c[n] = \theta_c[n - 1] + \omega_c[n]T$. The

parameter $\phi_c[k, n]$ is a slow varying phase for the k th harmonic ((139)). The respiratory term can be modeled by using a similar formulation:

$$y_r[n] = \sum_{k=1}^{N_r} a_r(k, n) \sin(\theta_r[n] + \phi_r[k, n]), \quad (\text{S4})$$

Therefore, h is a nonlinear function of the form:

$$h = m[n] + y_c[n] + y_r[n] = m[n] + \sum_{k=1}^{N_c} a_c(k, n) \sin(k\theta_c[n] + \phi_c[k, n]) \quad (\text{S5})$$

$$+ \sum_{k=1}^{N_r} a_r(k, n) \sin(k\theta_r[n] + \phi_r[k, n]), \quad (\text{S6})$$

In the state space model of the extended Kalman filter there are nine different state variable categories which are listed in table S1. The function f in the state model is:

$$f(x[n]) = \begin{bmatrix} m[n] \\ \bar{\omega}_c + \alpha_c (S_c(\omega_c[n]) - \bar{\omega}_c) \\ \theta_c + T_s S_c(\omega_c[n]) \\ \{a_c(k, n)\} \\ \{\phi_c(k, n)\} \\ \bar{\omega}_r + \alpha_r (S_r(\omega_r[n]) - \bar{\omega}_r) \\ \theta_r + T_s S_r(\omega_r[n]) \\ \{a_r(k, n)\} \\ \{\phi_r(k, n)\} \end{bmatrix}, \quad (\text{S7})$$

To obtain a robust mechanism for the detection of the heart and breathing rates, some constraints were applied to the heart and breathing rates:

$$18.8rad/sec < \omega_c[n] < 56.5rad/sec, \quad (S8)$$

$$4.4rad/sec < \omega_r[n] < 17.6rad/sec. \quad (S9)$$

These values were chosen to cover the range of the typical values for heart and respiratory pulsation rates in anesthetized mice under ketamine-xylazine injections ((147)). Since the respiration and cardiac frequencies may change slowly over time, to track these values more efficiently, the model uses a white noise process to update the calculated breathing and heart rates at each iteration of the state model ((139)). Variances of the process noise determine how fast the rates can change over time. The variances that we used are listed in table S1 ($\sigma_{\omega_c}^2 = 0.05$ and $\sigma_{\omega_r}^2 = 0.05$). The functions $S_r(\omega_r[n])$ and $S_c(\omega_c[n])$ are saturation functions to clip the estimated heart and breathing instantaneous frequencies when they drift outside the corresponding dynamic range. These functions help improve the stability of the EKF ((139)).

The extended Kalman filter requires an estimate of initial values for the variables, the covariance matrix of the process noise (u), and the initial value for the *a priori* covariance matrix ($P_{0|-1}$). In this model, the covariance matrix was a diagonal matrix, where the diagonal elements are listed in table S1. The variable B in this table is the baseline for the blood flow signal, which is calculated by averaging the baseline period of the blood flow before starting the closed-loop blood flow control tests. This part of the signal was also used to estimate some of the initial values including the heart rate (Ω_c), amplitudes of its first four harmonics (A_c), and also the respiration rate (Ω_r) and the amplitude of its first two harmonics (A_r) via Fourier analysis. The fundamental frequencies of breathing or cardiac pulsations were estimated by finding the frequency component which had the maximum spectral power within the corresponding frequency band. The larger harmonics were assumed to be integer multiples of the fundamental frequencies. As suggested by McNamara and Aboy, we used 1%

State Variable	Description	Variance	Initial value
$m[n]$	signal trend	$\sigma_m^2 = 10^{-8} \times B$	B
$\omega_c[n]$	cardiac angular frequency	$\sigma_{\omega_c}^2 = 0.05$	Ω_c
$\theta_c[n]$	instantaneous angle of cardiac signal	$\sigma_{\theta_c}^2 = 0$	0
$\{\phi_c(k, n)\}$	initial phase of the k th cardiac harmonic, ($k = 1, \dots, 4$)	$\sigma_{\phi_c}^2 = 0$	0
$\{a_c(k, n)\}$	amplitude of the k th cardiac harmonic, ($k = 1, \dots, 4$)	$\sigma_{a_c}^2 = 0$	A_c
$\omega_r[n]$	respiration angular frequency	$\sigma_{\omega_r}^2 = 0.05$	Ω_r
$\theta_r[n]$	instantaneous angle of respiration signal	$\sigma_{\theta_r}^2 = 0$	0
$\{\phi_r(k, n)\}$	initial phase of the k th respiration harmonic ($k = 1, 2$)	$\sigma_{\phi_r}^2 = 0$	0
$\{a_r(k, n)\}$	amplitude of the k th respiration harmonic ($k = 1, 2$)	$\sigma_{a_r}^2 = 0$	A_r

Table S1: Initial values and variances of the Kalman filter variables. Values for B , Ω_c , Ω_r , A_c , and A_r are obtained by analyzing the baseline period as explained in the text.

of the variance values as the initial value of the *a priori* estimate covariance ($P_{0|-1}$). Another parameter to be used in extended Kalman filter is the variance of the measurement noise (r) which is empirically set to: $\sigma_v^2 = 4 * 10^{-6} \times B$.

Supplementary Note 4: Vasodilation can be the cause of discrepancy between velocity and flow responses

The flow and velocity receptive fields of the vessels in Figure 5.3 show some subtle differences. Since the blood velocity and blood flow are two different measures which are related by the cross-sectional area of the vessel lumen, one postulation is that the vessel dilation/constriction, controlled by the smooth muscle cells, can cause the difference between two receptive fields (RFs). To verify whether the dilation can explain the dissimilarities

between the flow and velocity maps, we produced a spurious flow receptive field by combining the RFs generated by the velocity and diameter responses. The new RF matched the measured flow RF (Supplementary Figure S2.d), suggesting that the mismatch between flow and velocity maps can in part be caused by the vessel dilation. The discrepancy between the flow, velocity, and dilation implies that the analysis of the vascular response, through measuring only the vessel diameter, is insufficient and potentially misleading since dilations in some pial vessels coincide with a drop in the flow.

Blood flow in penetrating arterioles is directly controlled by adjusting the vessel diameter. Even though pial arteries possess smooth muscle cells, their resistances are usually so small that fractional changes in their diameter does not modulate the blood flow similar to the penetrating arterioles. In other words, blood flow in pial vessels is mainly a function of the flow in downstream. As a result, in pial vessels we can observe discrepancies between changes in blood flow, blood velocity, and vessel diameter in response to stimulation. If penetrating arterioles are the main compartments that control blood flow in the network, then changes in their blood flow and diameter should be coherent. On the other hand, there have been evidences which suggest that capillaries also contribute to blood flow regulation. If the contribution of capillaries is significant, we expect to once again see some discrepancy between the traces of blood flow and vessel diameter even in penetrating arterioles.

Supplementary Note 5: Closed-loop blood flow control algorithm

This algorithm was implemented in two parallel processing loops: the OCT scanning and image processing loop, and the controller loop. Within the OCT loop, the scanner periodically scans and calculates the blood flow for the selected vessel cross-section(s) at the rate of 82 fps and uses a Length-locked MA filter or an EKF to remove the pulsation from the

blood flow. The data is stored in a queue to be used by the controller loop.

The controller loop retrieves the latest blood flow value from the queue and calculates the percentile difference between the current blood flow and the baseline value. The PID controller reads these values at the rate of the stimulation frequency (15Hz) to calculate the error signal, $e[n] = f_{set}[n] - f[n]$, where f_{set} and f are the desired and measured percentile changes in the blood flow, respectively, and n is the current time index. The optogenetic stimulation pulse width is then calculated in a discrete form:

$$U[n + 1] = K_P \times e[n] + K_I \times \sum_{i=0}^n e[i] + K_D \times (e[n] - e_f[n - 1]), \quad (\text{S10})$$

where K_P , K_I , and K_D are adjusted empirically and the optimal values found to be 3.1, 7.5×10^{-3} and 25, respectively. U is the duty cycle of the laser pulse which changes within the interval between 0 and 1. To avoid excessive light exposure, especially during the first few seconds of the control process, the value of U is upper bounded to 0.5. Any value of U larger than this threshold is clipped to 0.5. The pulse width is calculated by $D[n+1] = \frac{U[n+1]}{15}$ where coefficient $\frac{1}{15}$ represents the pulse period.

Supplementary Note 6: Tuning compensator gain values

For large values of K_P , the steady-state error reduced at the expense of a large overshoot. For $K_P = 3.1$, we observed a fast rise time but no large oscillation in the blood flow. By increasing the derivative gain from $K_D = 0$ to $K_D = 25$, the stability improved slightly. Derivative gains above $K_D = 25$ (e.g., $K_D = 50$) resulted in slight oscillations in the blood flow. Introduction of a small integrating gain (e.g., $K_I = 1.5 \times 10^{-3}$) had pronounced impact on reducing the steady-state error. A larger integrating gain (e.g., $K_I = 7.5 \times 10^{-3}$) reduced the steady-state error further but caused a small overshoot at the beginning of the controller's response. An integrating gain between $K_I = 1.5 \times 10^{-3}$ and $K_I = 7.5 \times 10^{-3}$ helped strike a proper balance between the steady-state error versus fluctuations. A large

gain value (e.g., $KI = 35 \times 10^{-3}$) resulted in some noticeable oscillations in the blood flow which could potentially lead to the destabilization of the compensator. At least three trials were recorded for each parameter settings to confirm the repeatability of the results. Figure S3 summarizes the results for tuning process of the PID controller.

Supplementary Note 7: OCT angiography

Lateral resolution of typical OCT scanners is within the range of few micrometers. The relatively coarse resolution of OCT limits the amount of vasodilation/vasoconstriction that this imaging modality can detect. Therefore, measuring fractional changes in the diameter of small arterioles with OCT is quite challenging. Moreover, the OCT angiography uses motion contrast to visualize vessels in a tissue. Logically, when there is motion in the tissue that surrounds a vessel (including vessel wall, smooth muscle cells, and the brain tissue), this tissue can be imaged as part of the vessel. As a result, in such case, vessel diameters are usually overestimated in the OCT generated angiograms.

5.5 Discussion

In this study we proposed several new methods to discern different temporal and spatial characteristics of the vascular response to direct brain stimulation. The potential of the new approach for capturing such characteristics was demonstrated by simultaneous measurement of blood flow, blood velocity, and vessel diameter to obtain novel and comprehensive datasets to analyze the behavior of the vascular network. Since many of our observations were the first of this kind at the vascular level, it is valuable to compare our findings with the results of preceding reports.

Our investigation of temporal characteristics of the blood flow dynamics following optical neurostimulation revealed a biphasic BFR comprised of an early fast transient (peaks at

$\sim 5\text{sec}$) and a slow prolong (peaks around $10\text{sec} - 40\text{sec}$) increase in blood flow. Increasing the duration of photostimulation increased the length and amplitude of the measured BFR particularly at the slow phase of the response. Meanwhile, the response to short light exposures lasted for at least 25sec but exceeded 45sec for longer stimulus durations (e.g., 12sec). Typically, the slow phase of the response to longer light exposures was more persistent. Generally, BFRs were followed by a slight decrease in the blood flow which is consistent with previous observations of post-stimulation vasoconstriction (e.g., see (151), (21)) or reduction in the blood volume (e.g., (152)). Prior to our study, a biphasic change in total hemoglobin and oxyhemoglobin was reported by Kennerley et. al. (153); however, the true cause of such peak-plateau responses are remained to be investigated.

We expected the blood flow to respond to the collective level of activity in nearby neurons. We confirmed this by showing that the BFR is a quasi-linear function of the volume of activation. Other researchers have also reported similar relations. For instance, Iordanova *et al.* (12) measured an upward trend in the cerebral blood flow (CBF) response when the intensity of optogenetic stimulation was increased up to 10mW . However, for light intensities above 10mW , the CBF saturated. Similarly, in peripheral stimulations, a quasi-linear relation between cerebral blood volume (CBV) and the level of local neural activity was reported (e.g., (150), (149)). While our observations also show that changes in CBV are quasi-linearly proportional to the stimulation power, simultaneous measurements of the vascular flow, CBV, and neural activity are required to obtain a complete model which captures all main features of the correlation between neural activity and the corresponding hemodynamics.

To investigate the spatial extent of the correlation between neural activity and the response of pial vessels we proposed a novel method to measure vessels' receptive fields. For an artery of diameter $30\mu\text{m}$, the full width at half maximum (FWHM) extension of the

receptive field was $\sim 1.4mm$ wide. However, based on our simulations, the VoAs in our tests (Figure 5.2.a) spread about $1mm$ in the lateral direction. While the VoA is comparable to the measured FWHM, it still implies that the spatial extent of the receptive field was over estimated. Prior to this study, observations by Nishimura et al. on rat cortex demonstrated that the blockage of a penetrating artery affects the blood flow in a region of radius $\sim 350\mu m$ (154), which can cause a microinfarction in an area as large as $460\mu m$ in diameter (155). Also, findings of OHerron et. al. in cat visual cortex indicated a correlation between the dilation of parenchymal arterioles and the synaptic or spiking activity in neurons up to $200\mu m$ farther away from the vessels (156). Although, our findings for pial artery (diameter of $\sim 30\mu m$), cannot be directly compared to the previous reports; our results do not contradict with those observations either. The relatively large vessel under test in our study was feeding several penetrating arterioles which were widely distributed in the region. Evidently, a larger vessel diameter translates to a larger receptive field. Stimulating the territory of each penetrating arteriole affects the upstream flow and contributes to the shape and distribution of the receptive field for such a pial vessel. Practically, it is challenging to adapt the previous methods to measure the influential region of an arbitrary vessel, since they are very invasive or are confined to measurements in the visual cortex. While, the proposed method does not require vessel disruption and is not limited to a specific region of the brain cortex of transgenic animals. Although, the current measurements are presented for arteries of size $30\mu m$ or larger, in combination with high-resolution OCT or multi-photon microscopy the same approach might be applicable to obtain the receptive field of parenchymal arterioles of smaller diameter as well.

In our experiments, we mainly observed blood flow amplification at the vicinity of stimulation site; however, in the surrounding tissue, we occasionally detected some form of reduction in the flow. This decrease in the blood flow in the surrounding tissue is followed by some drop in blood oxygenation level in the region which was also observed by other research groups and considered as a center-surround hemodynamic response (157), (158).

Nonetheless, the signaling pathway and the mechanisms that mediate this form of response are not well-understood. We anticipate that measuring receptive fields of the main vessels over a large field of view and performing hemodynamic recording simultaneously together with other imaging modalities (e.g., multi-spectral and metabolic imaging) can help elucidate details of the mechanisms that cast such center-surround hemodynamic responses.

We learned from our multi-site stimulation experiments that the flow response is the superposition of the responses to each individual stimulation. On the other hand, extracting vascular receptive fields can help to describe the correlation between the spatial distribution of neural activity and the corresponding vasodynamics. We can combine these two principles to predict the blood flow response to any arbitrary illumination pattern by first decomposing the pattern to a group of confined stimulations and then estimating the overall response as the weighted superposition of responses to each individual element. Considering this approach, it would become a possibility to use this information to design the spatial and temporal extent of our stimulation patterns to engineer desired distributions of blood flow in the cortical tissue.

Examining, validating, or generating new hypotheses and models via a closed-loop mechanism has become a common practice in recent years (159), (160); however, no such method has been proposed for the cerebral blood flow. In this dissertation, we also demonstrated the ability of a closed-loop PID controller to manipulate the flow of blood in the cortex of transgenic animals. The gain variables of the compensator were tuned to obtain a near to critically-damped response in the blood flow of one animal. The same values were used later in other animals and yet near-critically damped responses were recorded which potentially implies that a similar circuit-model describes the relation between vascular flow and an exogenous input across different animals. Investigating the blood flow via a closed-loop mechanism opens an avenue to study long-term properties of the response of regional and global blood supply to long exogenous perturbation in neural activity.

Moreover, the closed-loop algorithm that we presented in this article can be expanded

to form a distributed controller which maintains a desired spatial-temporal pattern of blood flow in a large scale vascular network. For this purpose, the compensator should assimilate the spatial influence of a local perturbation on off-target vessels (Figures 5.2.i and 5.3, and reference (151)), which can be well estimated when the vascular receptive fields are measured. By upgrading to a model predictive controller (MPC), instead of the basic PID algorithm used in this work, the effect of long and biphasic vascular reaction to the stimulation can be incorporated in the control algorithm to improve the efficiency of photostimulation.

In multiple experiments, we showed that blood flow and blood velocity respond differently to photostimulation pulses (Figures 5.2.i and 5.3). Such discrepancy is the result of the way these variables are related to changes in the vessel diameter which is controlled by muscle cells. Our observations were mainly limited to small arteries but we did not study penetrating and parenchymal arterioles in this work (Supplementary Note 4). Investigation of small changes in a vessel diameter with OCT is challenging (Supplementary Note 7). Accompanying the OCT data with a second high resolution imaging modality, such as two-photon microscopy, can increase the accuracy of the vascular diameter detection and improve our insight into different aspects of vascular response. Nevertheless, studying mechanisms that regulate the flow of blood in the brain by using imaging techniques that solely measure vessel dilation/constriction can be misleading and interpretation of such data should be handled cautiously.

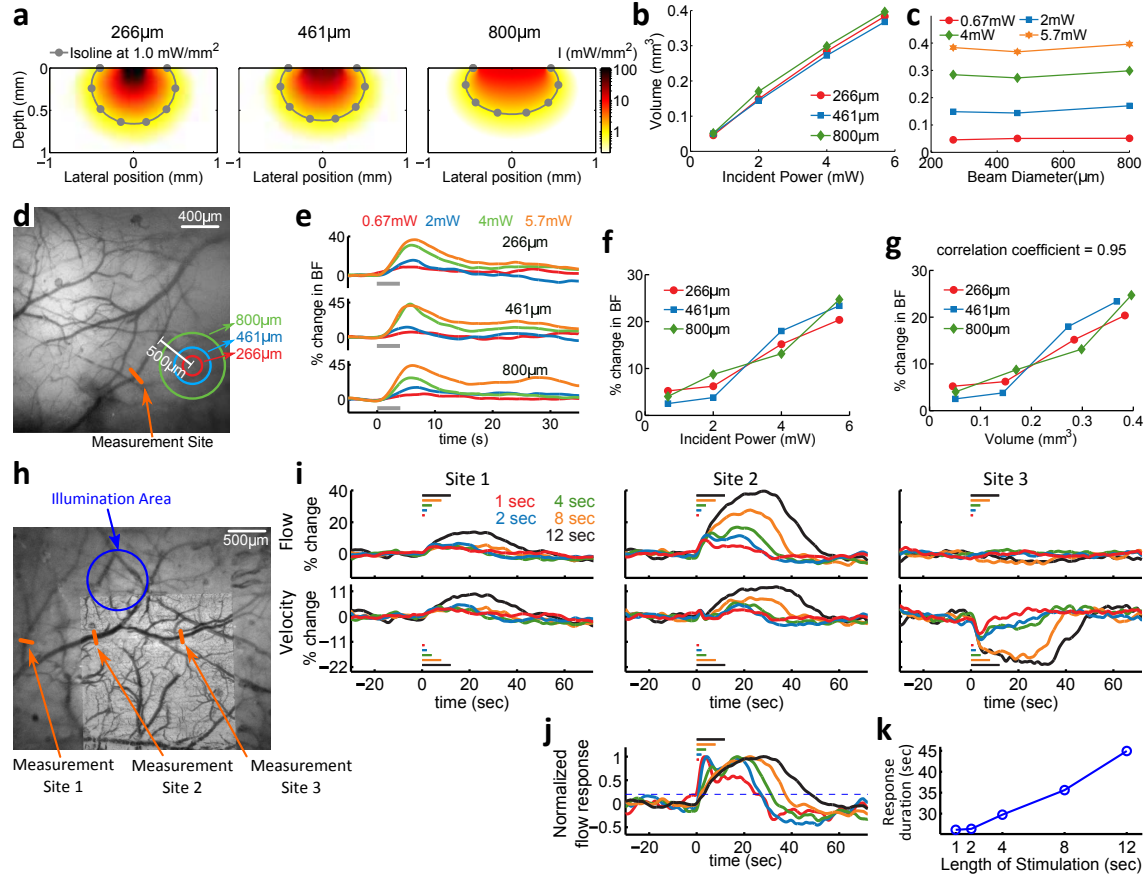


Figure 5.2: Stimulation configurations: (a) The light distribution profile ($\lambda = 450nm$, $I = 5.7mW$) estimated by using Monte Carlo simulations for three different beam diameters of $266\mu m$, $461\mu m$, and $800\mu m$. The colorcode represents the photon density and the dark line represents the isoline at $1mW/mm^2$. (b) Effect of light intensity on the volume of activation (VoA). (c) Effect of the beam diameter on the VoA. (d) The fluorescent image captured from the cortical tissue showing the vasculature network. Areas of stimulation with different spot sizes are marked by different colors. (e) Effect of stimulation intensity on the blood flow response (BFR), for illumination diameters of $266\mu m$, $461\mu m$, and $800\mu m$ (from top to bottom, respectively). The gray line indicates the duration of stimulation (4 seconds). (f) The relationship between the stimulation light intensity and the average percentile change in the blood flow from stimulation onset to 20sec afterward ($n = 1$ vessel). (g) The relationship between the simulated VoA and the in-vivo BFR measurements ($n = 1$ vessel). (h) The fusion of fluorescent image and the OCT angiogram shows the vasculature network. The blue circle marks the area under illumination ($I = 5.7mW$, duration varied from 1sec to 12sec). The arrows indicate the vessel cross-sections to be monitored by the OCT. (i) The blood flow (top) and blood velocity (bottom) responses in the target vessels. Blood flow at the measurement sites 1 and 2 increases after the stimulation onset, but not at site 3. Longer stimulus duration causes stronger and lasting responses at sites 1 and 2. (j) The normalized BFR at site 2. Longer stimulations translate to enduring responses which take more time before returning to the baseline. The dashed line marks 20% threshold. (k) BFR duration as a function of the stimulation duration ($n = 1$ vessel).

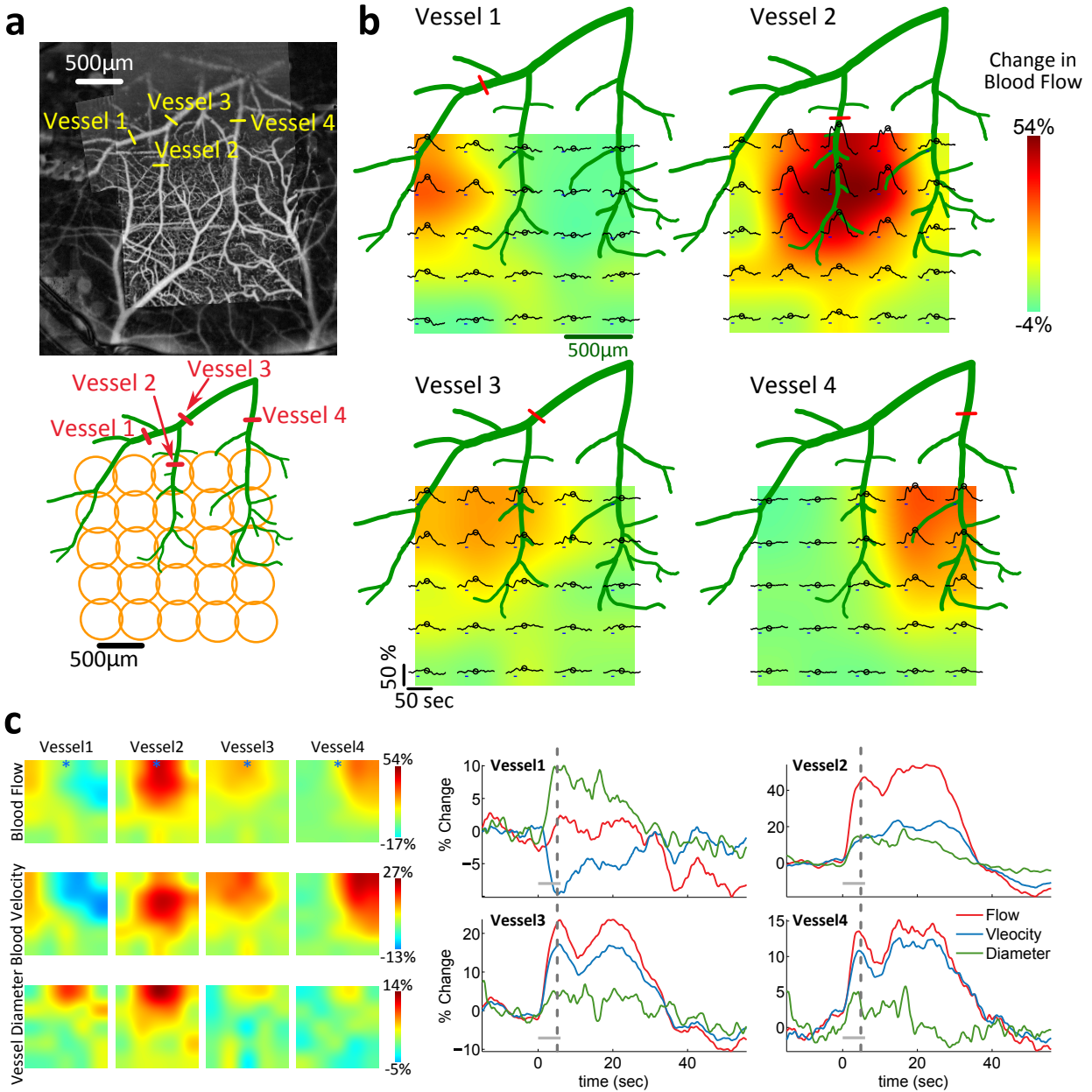


Figure 5.3: Vascular receptive fields. (a) The vascular network in the animal under test (top) and the 25 stimulation locations (bottom) in a form of a 5 by 5 matrix. Diameters of the circles are $461\mu\text{m}$ to represent the actual beam diameter on the tissue surface. The red lines mark the vessel cross-sections that are being imaged as monitoring sites. (b) The color coded receptive field (RF) of the arterial blood flow for the 4 selected vessel cross-sections. The dark red color shows strong increase, green color represents zero response, and blue color represents decrease in the blood flow in each vessel. The RF for the vessel 2 was $734\mu\text{m}$ long and $539\mu\text{m}$ wide. (c) The RFs for blood flow, blood velocity, and vessel diameter measured at $t = 5$ seconds. The curves show the time traces of blood flow, blood velocity, and vessel diameter percentile change for all the selected vessels when the stimulation was located on vessel 2 (marked by an asterisk). No significant blood flow increase in vessel 1 was observed; however, simultaneous dilation of the vessel caused some drop in its blood velocity.

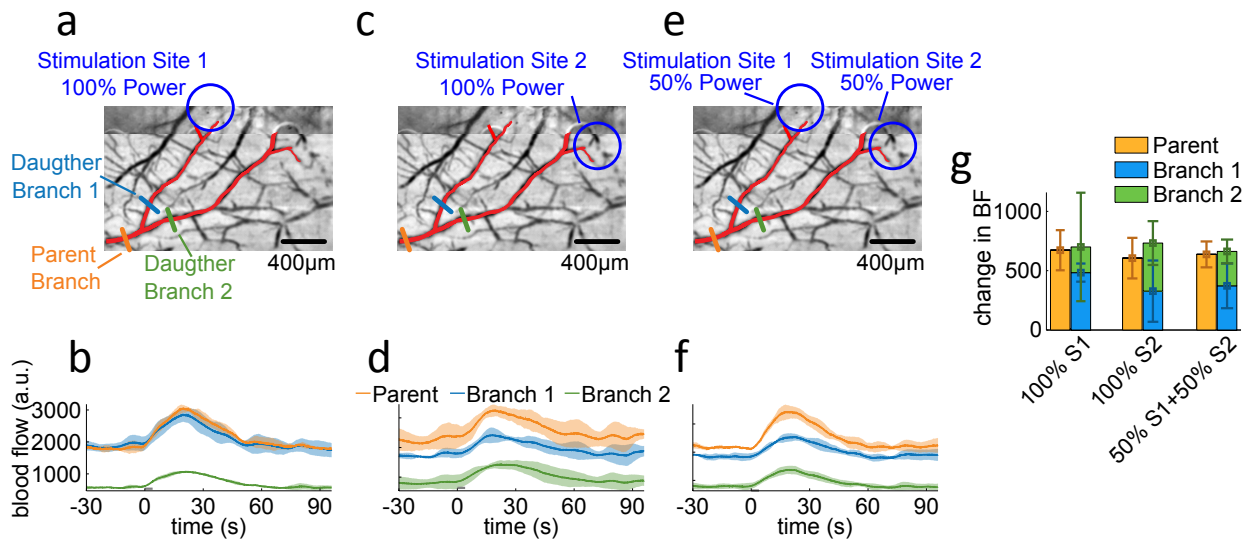


Figure 5.4: Simultaneous multi-site stimulation. Stimulation sites in each panel are marked by blue circles. (a) Fusion of the fluorescence and angiographic images of the vascular network in the animal under test. The vessels of interest (a parent and its daughter branches) are highlighted by the red color. In this experiment, the stimulation is applied only to site 1. (b) Time traces of blood flow in the selected vessels. BFRs in all three vessels were responsive at different levels to photostimulation of site 1. The gray line shows the period that the stimulation was applied. Each recording was repeated at least four times and the results were averaged. The solid line is the average across trials and the shaded area represents the standard deviation. (c) In this experiment, the stimulation was delivered only to site 2. (d) Time traces of blood flow in selected vessels following the stimulation of site 2. BFRs in all three vessels were responsive at different levels to photostimulation of site 2. (e) We simultaneously stimulated sites 1 and 2 at half of the power used in last two experiments of panels (a) and (c). (f) The time traces of blood flow in all selected vessels for simultaneous stimulation test. (g) A summary of the amount of BFR (blood flow averaged over 60 seconds) under different stimulation scenarios ($n = 3$ vessels). The error bars represent the standard deviation across trials.

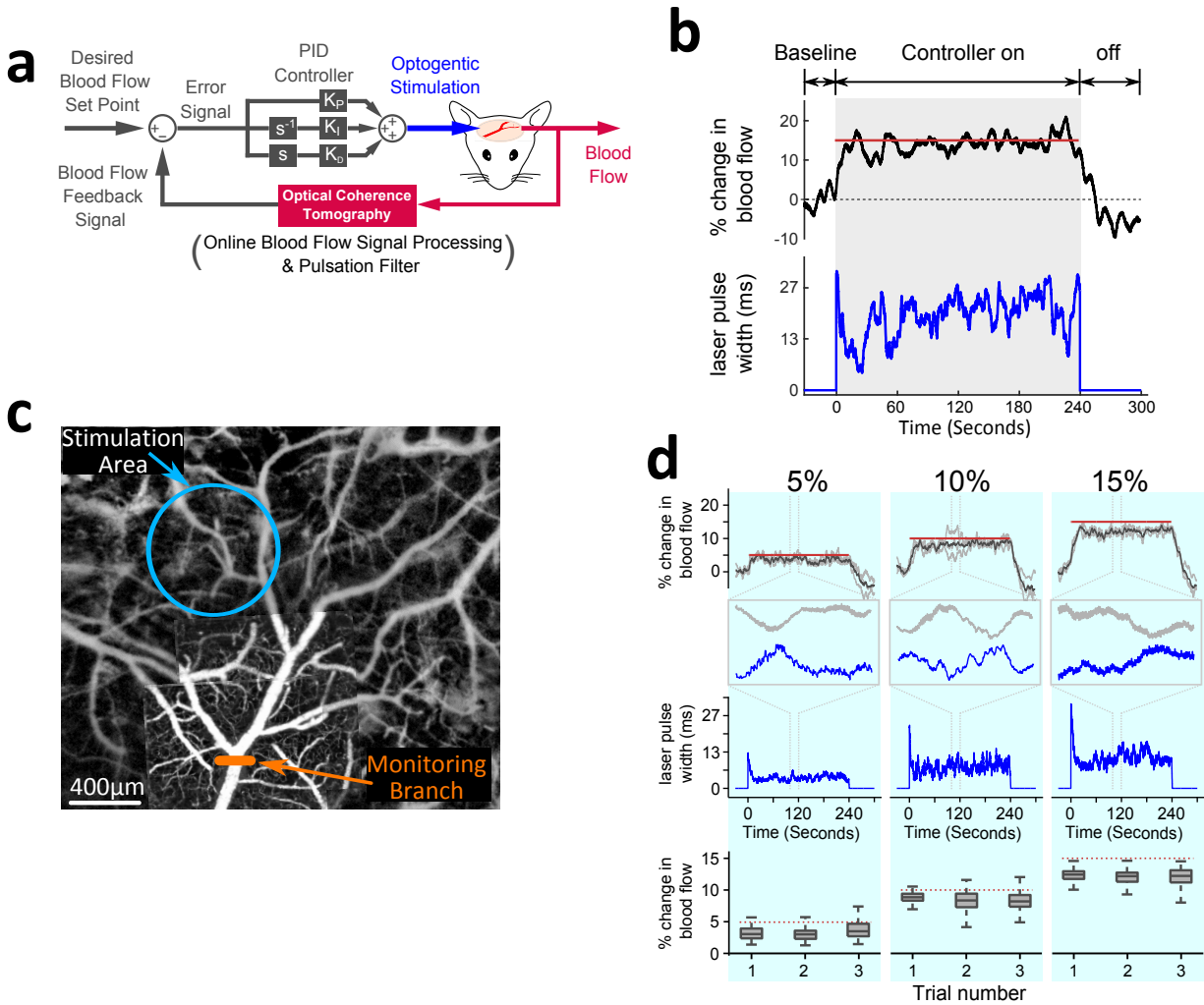


Figure 5.5: Optogenetic-based closed-loop control of blood flow. (a) Block-diagram of the closed-loop controller. The system uses OCT to measure the difference between the user defined target for blood flow and the actual value measured in the vessel(s) of interest. The difference is fed to a PID compensator to adjust the pulse width of photostimulation. (b) Smoothed blood flow (top) and optogenetic pulse width (bottom) during a control epoch (330sec). Data collection contains 30sec of baseline recording followed by 240sec of control period and 60sec (or 90sec) of post stimulation recording. The target blood flow level is shown by a red solid line in the top plot. (c) Vascular network in the animal under test. The area of illumination is marked by the blue circle. The arrow points to the vessel cross section under study. (d) Maintaining blood flow at different set points. Each experiment was repeated three times when the variables of the PID controller were adjusted at $K_P = 3.1$, $K_D = 25$, and $K_I = 1.5 \times 10^{-3}$. The first row shows the traces of BFR for three experiments each targeting a different set point on same artery. The solid line represents the average of trials. The inset magnifies 30sec duration of each test to substantiate the correlation between the flow (gray line) and the stimulation pulse width (blue line) for a typical trial. The second row displays the time trace of the pulse width in each test. The last row shows the distribution of blood flow during the last 120sec of control session. The center mark is the median, the whiskers are the maximum and minimum, and the box edges are the 25th and 75th percentiles of the data.

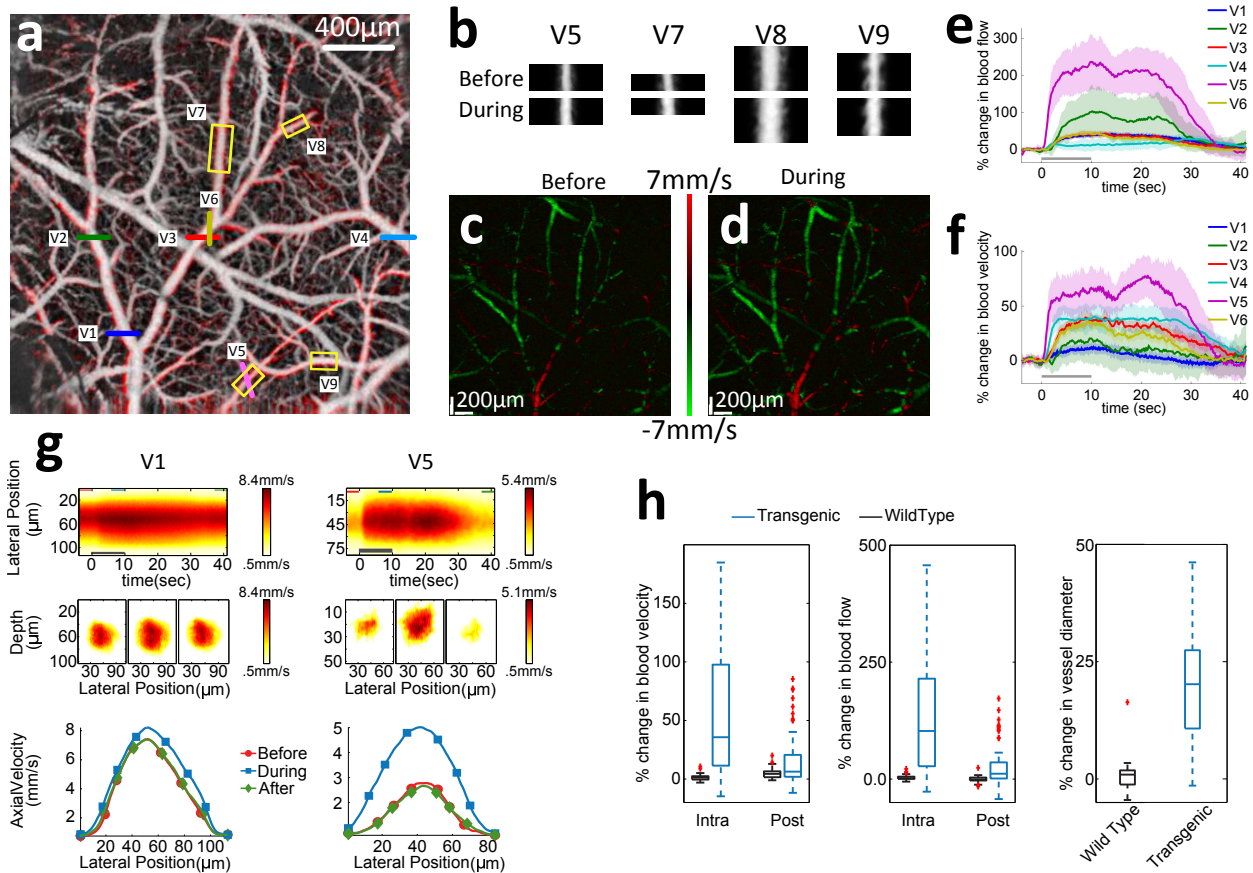


Figure S1: The effect of wide-field photostimulation on cortical vasculature. (a) OCT generated angiogram demonstrates a wide spread vessel dilation in response to optogenetic stimulation. The induced change in each vessel diameter is marked by the surrounding red color around that vessel. (b) Discrete angiograms of a few selected vessels before and after stimulation highlight observed changes. (c) Maximum intensity projection (MIP) of 3D Doppler OCT measurements before stimulation. (d) MIP of 3D Doppler OCT measurements after stimulation. (e) Percentile change in blood flow in response to 10sec of stimulation in vessels marked in panel (a). Each graph was obtained by averaging at least eight trials. The shaded areas show standard deviations. (f) Percentile change in blood velocity for vessels shown in panel (e). (g) Change in the velocity profile in response to optogenetic stimulation. Top: the maximum velocity projection of the vessel profile over time. The horizontal axis represents time while the vertical axis is the lateral position across the vessel. The pixel intensity is the maximum velocity along the depth in that location. The solid black line shows the duration of stimulation. Middle: three cross-sectional velocity profiles of the vessels 4sec before, 6sec after, and 36sec after the stimulus onset. Each curve is obtained by averaging the measured Doppler profiles for 4sec. Bottom: the maximum value projection curves of three cross-sections. Results show the velocity increase at the center of vessels as well as the change in velocity profiles. (h) Summary of the percentile changes in blood flow, blood velocity, and vessel diameter for five transgenic and three wild-type animals in response to optical neurostimulation.

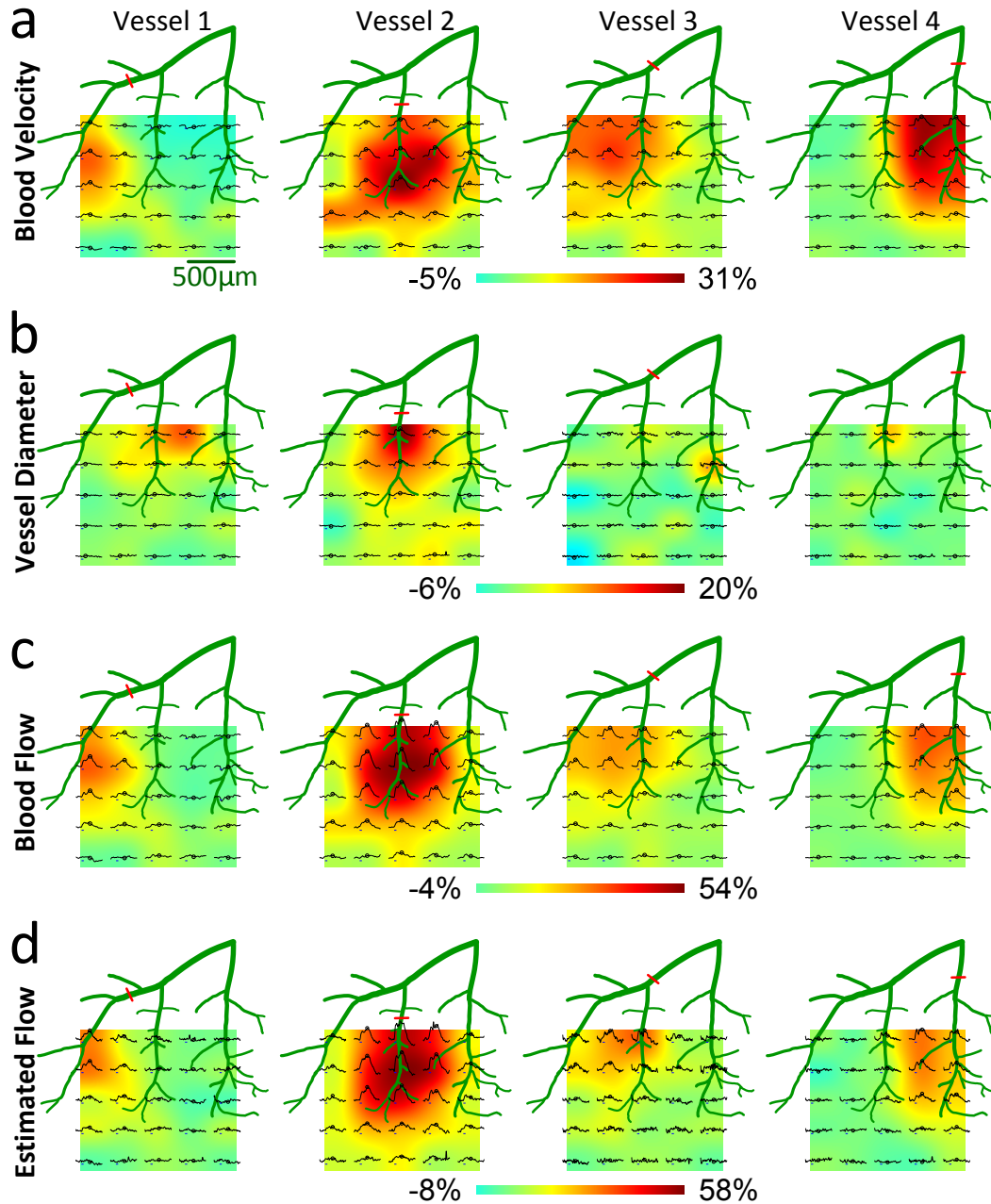


Figure S2: Velocity, diameter, and flow receptive fields. (a) velocity receptive fields of four vessels under study. The response in blood velocity is stronger when we stimulate the area closer to the territory of a vessel. The maximum velocity increase (31%) was observed was in vessel 4. (b) Diameter receptive fields. Unlike blood velocity, we observed that the map of vessel dilation does not necessarily collocate with the territory of the vessels. Basically, we observed that the maximum dilation for vessel 1 and 4 happens when we stimulate the territory of vessel 2. Stimulating the territory of these vessels did not evoke a noticeable dilation. This can be justified by the endothelial signaling hypothesis (144). (Since the lateral resolution of our OCT is $\sim 5\mu m$, accurate measurements of sub-micron changes in vessel diameters was quite challenging.) (c) Flow receptive fields. Vessel 2 shows the largest flow response (54% increase). Similar to velocity receptive fields The maximum response happens when the light illumination is on the vessel and the response drops quickly as we move away from the vessel. Despite this similarity, we observed some differences between the two receptive fields. For example, in vessel 1 and 2, we see that the shape of the receptive fields are different for blood flow and velocity. Another example, is the vessel 4. This vessel shows the largest increase in its blood velocity, while the largest increase in the blood flow is observed in vessel 2. The difference between the receptive fields of blood flow and velocity is potentially due to the dilation in these vessels. (d) Estimated flow receptive fields when we combined the diameter and the velocity fields to estimate the flow response. The estimated flow was calculated by $(\hat{F}_{RF} = (1 + D_{RF})^2(1 + V_{RF}) - 1$, where V_{RF} and D_{RF} are the velocity and diameter receptive fields, and \hat{F}_{RF} is the estimated flow receptive field. The estimated flow receptive field matches the flow measurements in panel (c).

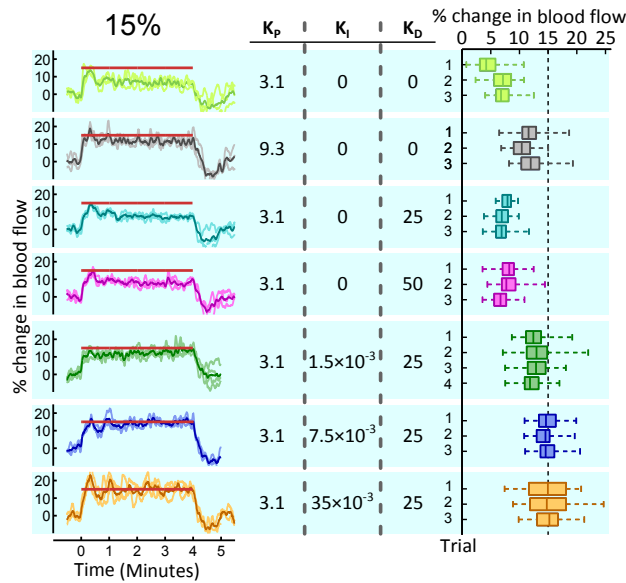


Figure S3: Tuning the PID gain values when the target value set at 15%. $KP = 3.1$ resulted in fast response and low oscillations in the blood flow. Larger values of KP led to large flow overshoots. Flow fluctuations decreased at $KD = 25$ and increased when KD was set to 50. The steady state error was significantly reduced for $KI = 1.5 \times 10^{-3}$. At $KI = 7.5 \times 10^{-3}$, the steady state error reduced further and no large fluctuation in the blood flow was observed. Larger KI values (35×10^{-3}) caused some oscillations in blood flow. The last column in this panel shows the distribution of the blood flow during the last 2 minutes of each control session. Longer whiskers oscillations correspond to stronger fluctuations in the blood flow.

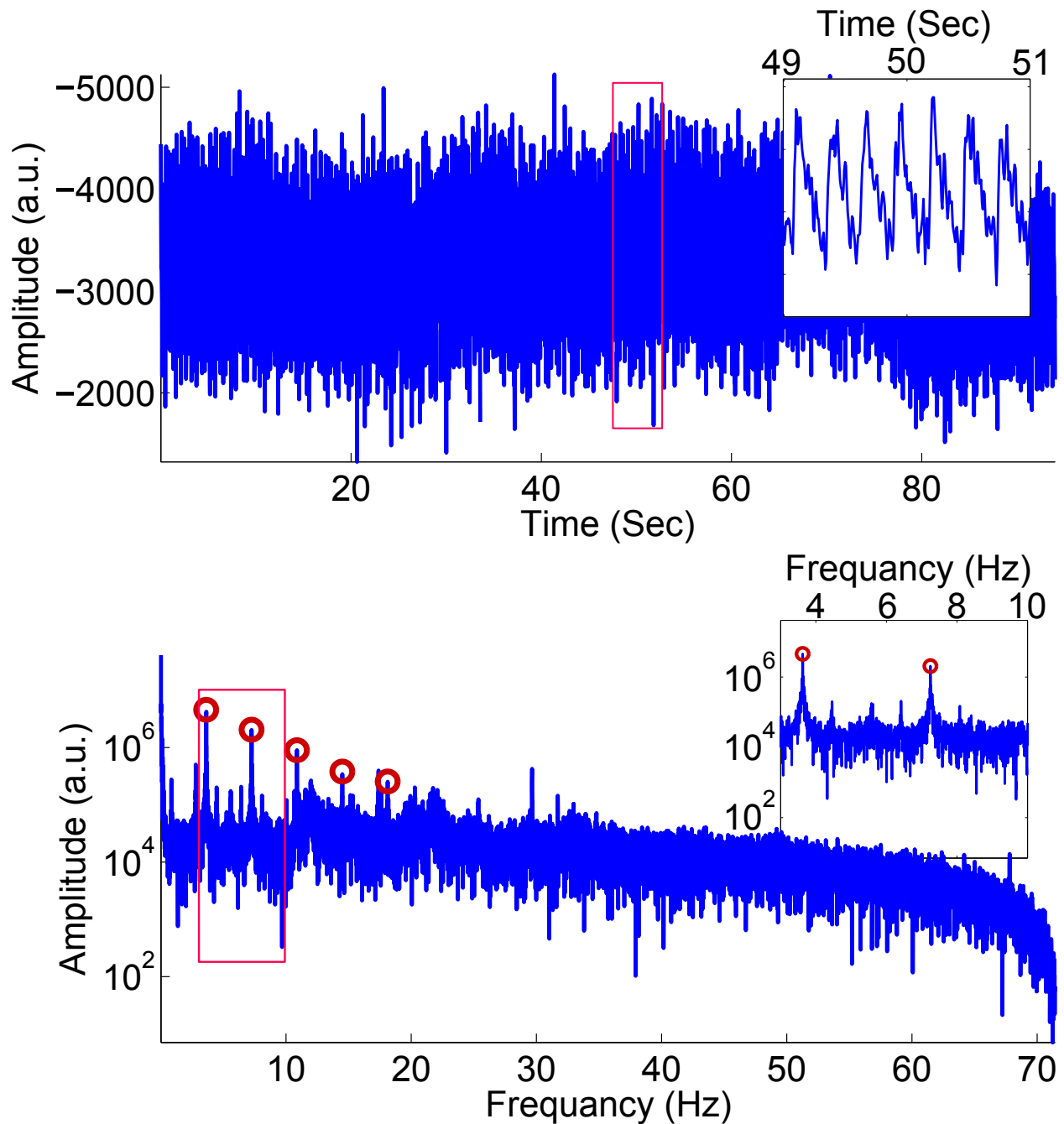


Figure S4: Blood flow and its spectrum. (top) A typical blood flow trace measured by the OCT scanner. The inset shows a magnified portion of the signal in which the heart pulsation and its harmonics are visible. (bottom) Spectrum of the blood flow signal. The red circles represent the main frequency and the first 4 harmonics of the signal. The frequency components beyond the 5th harmonic are weak and can be ignored.

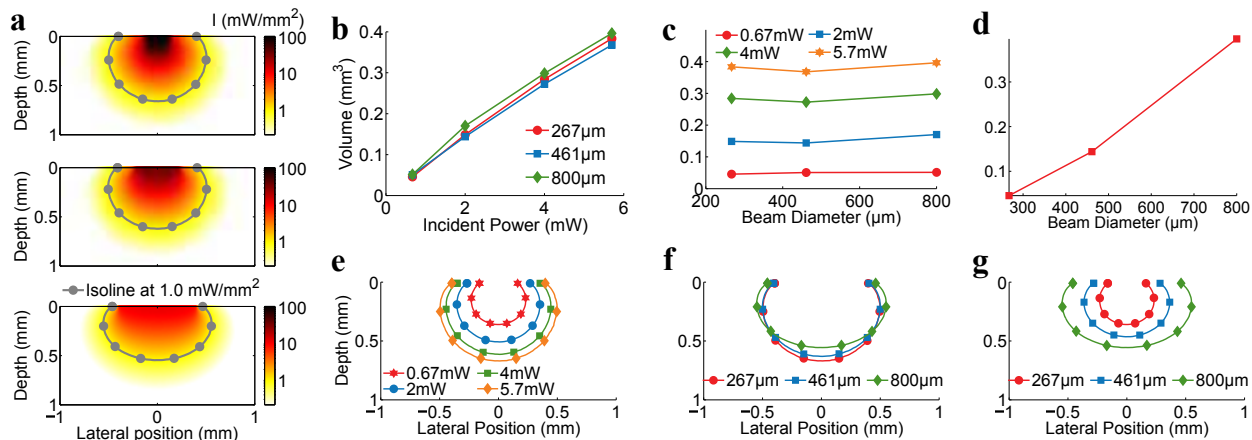


Figure S5: Light distribution in tissue. (a) Estimation of light distribution in tissue by the use of Monte Carlo simulations. We assumed uniform illumination on spot sizes of diameters $266\mu\text{m}$, $461\mu\text{m}$, and $800\mu\text{m}$ on the tissue surface. Results show noticeable differences between light distributions associated with different spot sizes. Changing the size of illumination spot from $266\mu\text{m}$ to $800\mu\text{m}$ (almost 3 times increase in diameter) does not cause a considerable change in the lateral extent of the volume of Activation (VoA). Therefore, using a small spot does not lead to localization of stimulation. However, using a small spot has the advantage of slightly deepening the volume of stimulation. (b) Effect of light power on the VoA. We estimated the VoA by measuring the tissue volume that is receiving irradiance of $1\text{mW}/\text{mm}^2$ or larger. Different spot sizes are represented by different colors. We observed linear relationship between the VoA and the light intensity. Under the assumptions of uniform distribution of ChR2 channels and constant density of neurons in the volume of stimulation in the cortex, this result suggests that the evoked blood flow response is mostly depends on the light intensity. (c) Effect of the beam diameter on VoA. We see a negligibly small difference between the volumes of stimulation under different illumination sizes when light intensity is kept constant. (d) Effect of irradiance on VoA. This curve shows the VoA with respect to the beam diameter when the irradiance was set to $\approx 12\text{mW}/\text{mm}^2$. We observe a non-linear relationship between the increase in the beam diameter and VoA. (e) Isolines of irradiance $1\text{mW}/\text{mm}^2$ for different illumination intensities when the illumination diameter is set to $266\mu\text{m}$. The axial and lateral extent of VoA grows as intensity increases. (f) Isolines of irradiance $1\text{mW}/\text{mm}^2$ for different illumination spot sizes at illumination power 5.7mW . The isolines show that the smaller spot size can result in slightly deeper stimulation profile compared to large spot sizes at the expense of large irradiance on the surface. (g) Isolines of irradiance $1\text{mW}/\text{mm}^2$ when the irradiance was fixed at $\approx 12\text{mW}/\text{mm}^2$. When the irradiance is constant, at a safe level to avoid causing any damage to the tissue, a large spot size results in deeper stimulation profile.

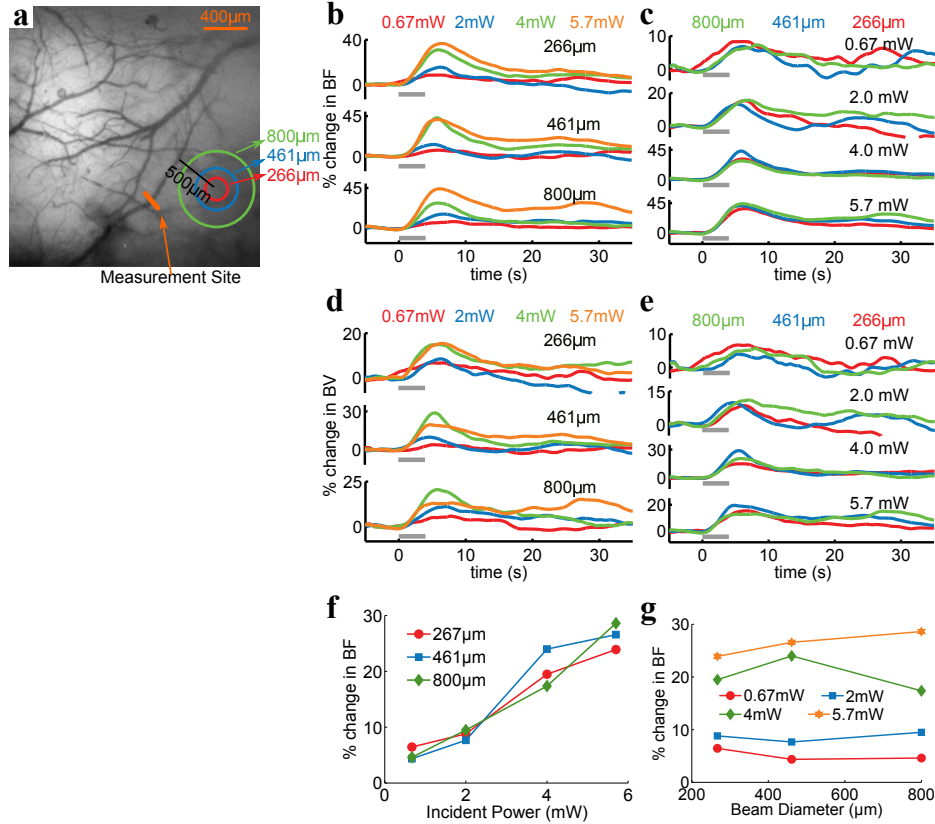


Figure S6: (a) A fluorescence image captured with the optical setup shows the spread of the vasculature network. The area of photostimulation using different spot sizes ($266\mu m$, $461\mu m$, and $800\mu m$) is demonstrated by different colors. The center of stimulation was located about $0.5mm$ away from the target arteriole. (b) The effect of stimulation intensity on the blood flow response for the illumination diameters: $266\mu m$ (top), $461\mu m$ (middle), and $800\mu m$ (bottom). For all spot sizes, increasing the power of photostimulation led to increase in the amplitude of the blood flow response. (c) Effect of the area of illumination on the blood flow response. Each subfigure shows traces of blood flow response to stimulation of different spot sizes ($266\mu m$, $461\mu m$, and $800\mu m$ in diameter). For each subfigure, the stimulation power was kept constant. The subfigures from top to bottom show the response traces for the illumination power of $0.67mW$, $2mW$, $4mW$, and $5.7mW$, respectively. We observed no noticeable differences between the shape and the maximum amplitude of the BFR with the exception for the $4mW$ power and $461\mu m$ spot size. (d) Effect of stimulation intensity on blood velocity response. In general, increasing the intensity leads to some increase in the amplitude of the blood velocity response. However, this is not the case in all traces. For example, for the illumination diameter $800\mu m$, we see that increasing the power from $4mW$ to $5.7mW$ resulted in some decrease in the amplitude of the evoked blood velocity. When comparing the velocity response to the corresponding flow response, we notice that the blood flow and blood velocity do not follow the same pattern. For $5.7mW$ power, the amplitude of evoked blood flow response is noticeably larger than the one in $4mW$, suggesting that the vessel dilation causes the difference between flow and velocity responses. (e) Effect of the size of the illumination area on blood velocity. We observed no consistent difference between the shape and maximum amplitude of the blood velocity responses as we changed the spot size. (f) Relationship between the intensity of stimulation and the evoked response. We can see the amount of blood flow response as a function of the incident power. Results for different illumination sizes are shown with different colors. We observe a quasi-linear relationship between the illumination power and the evoked response. The amount of response here is calculated by averaging the percentile change in the blood flow from the stimulation onset to 10 seconds afterward. (g) The relationship between the beam diameter and the evoked response at constant illumination intensity. We can see the amount of evoked response remains almost constant as we change the spot size. This suggests that the area of illumination is not the determining factor in flow response as long as the power is kept constant. The quasi-linear relation between the stimulation power and hemodynamics response is comparable to the observations of (149) ¹³⁵macaques, and (150) in rats.

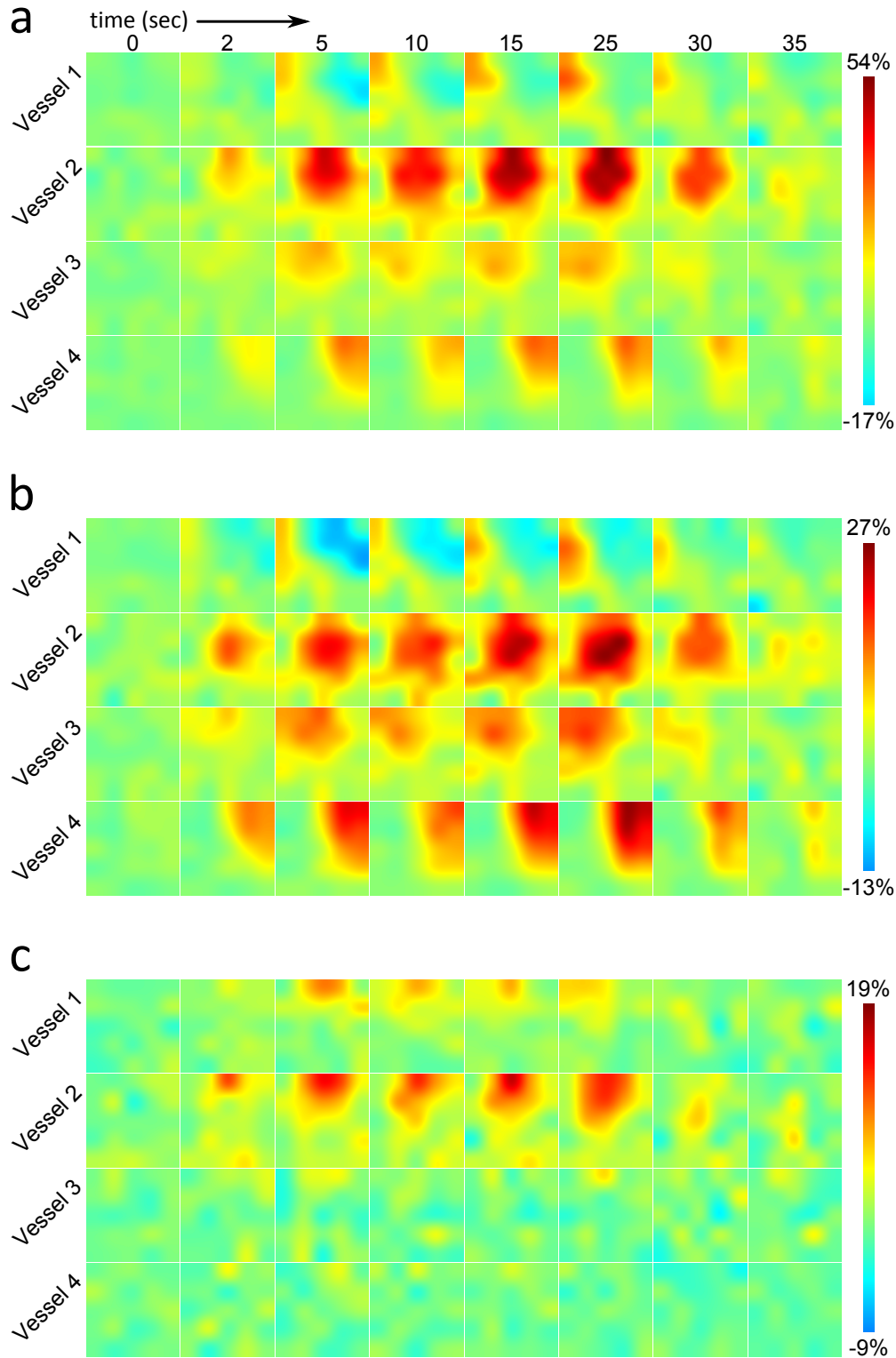


Figure S7: Time-lapse images of the receptive fields. (a) Time-lapse images of flow receptive fields demonstrate the bi-phasic flow response. The fast and slow peaks occur at $t \sim 5s$ and $t \sim 18s$. Stimulation at the top-right portion of field of view (FOV) results some reduction in the blood flow of vessel 1 around $t \sim 5s$ which gradually returns to the baseline at $t > 15s$. (b) Time-lapse images of velocity receptive fields. A noticeable reduction in the velocity of vessel 1 occurs in synchrony with the drop in its blood flow when stimulating the top-right region of the FOV. (c) Time-lapse images of diameter receptive fields shows dilation in vessels 1 and 2 that are linked both in time and space.

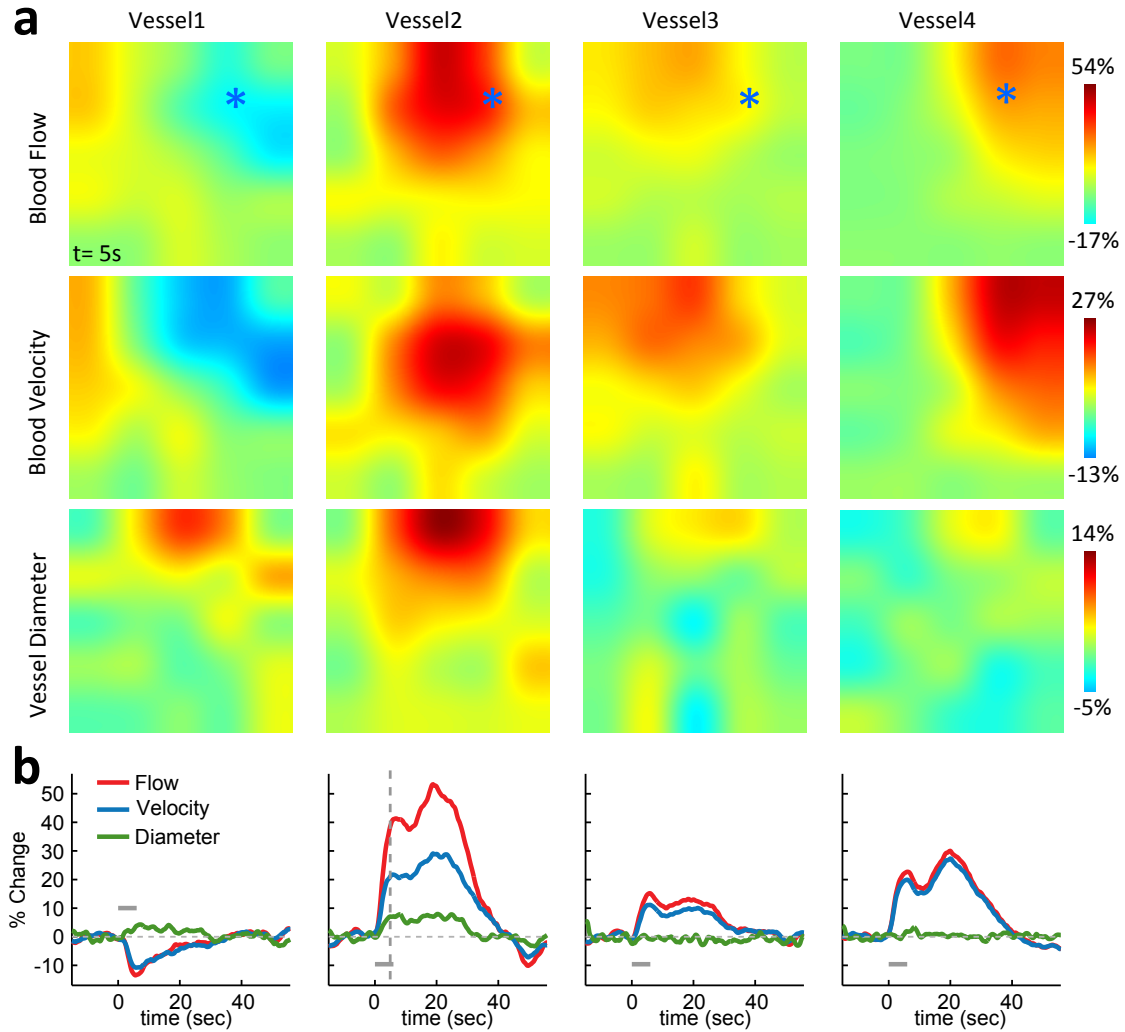


Figure S8: Flow may drop without noticeable change in the vessel diameter. (a) Flow, velocity and diameter receptive fields at $t = 5$ seconds. (b) Flow, velocity, and diameter time traces for vessels 1 to 4 (left to right) when stimulating the location marked by the asterisk in panel (a). Optical coherence angiography detected no reduction in the diameter of vessel 1 but there was some drop ($\sim 10\%$) in its flow and velocity.

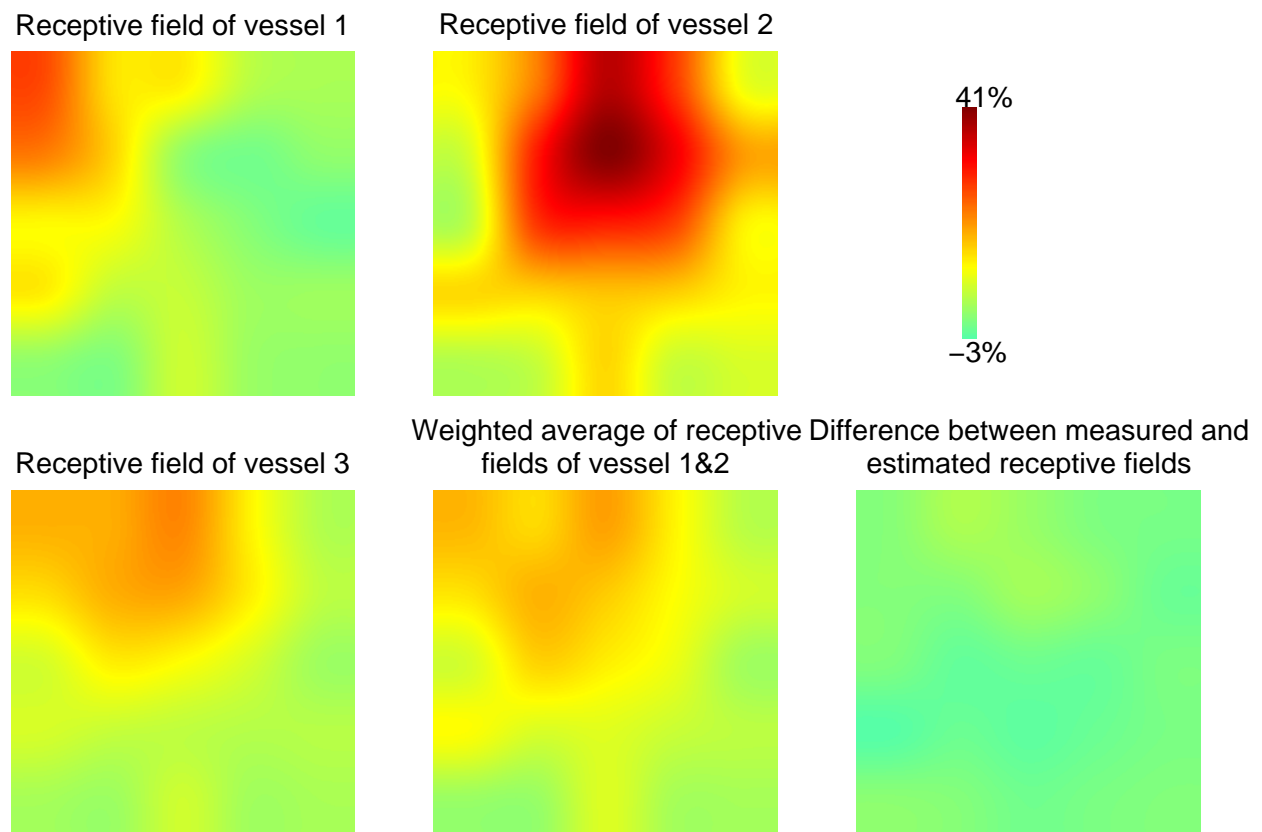


Figure S9: Superposition of receptive fields of daughter vessels 1 and 2 provide an estimate of the receptive field of their parent vessel (vessel 3). The mean square error between the measured and the estimated receptive fields for the parent vessel was 2.7%.

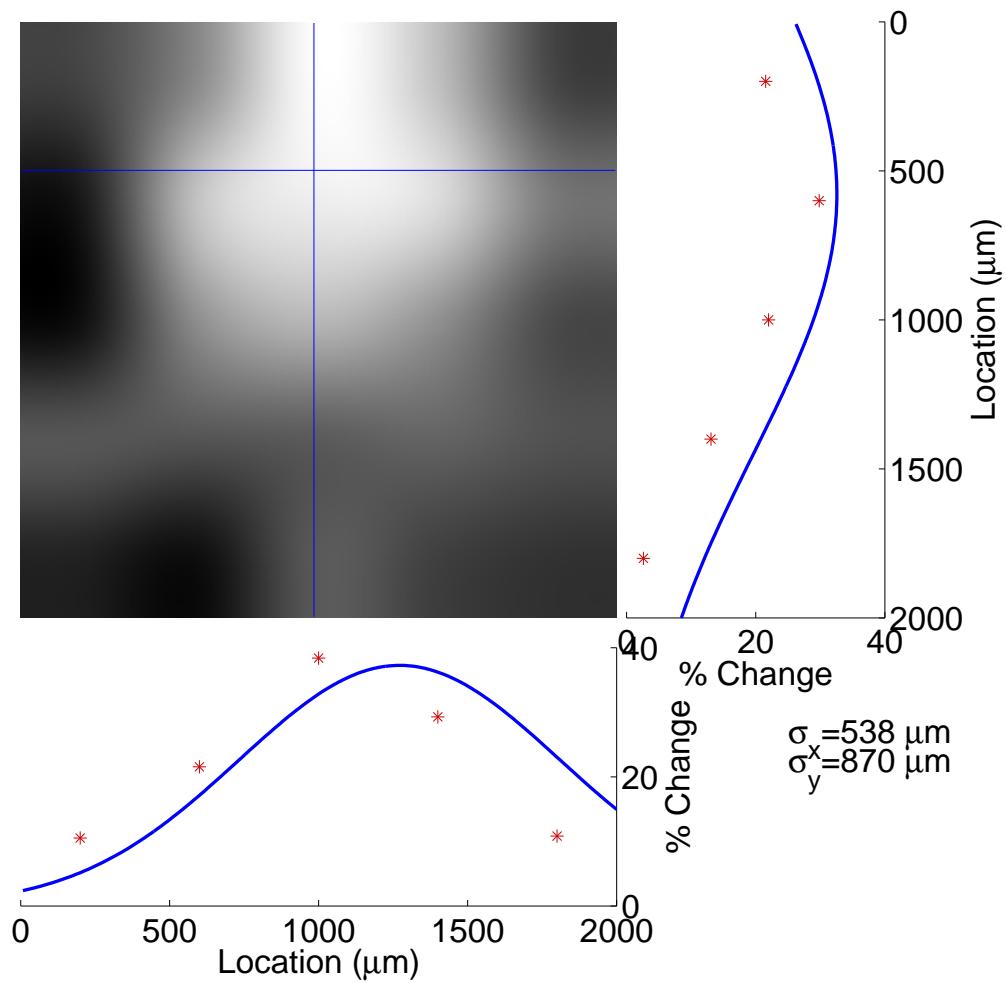


Figure S10: By fitting a Gaussian curve to the receptive field of vessel 2, we estimated the lateral extend of the receptive field to measure the standard deviation of $\sigma_x = 538\mu\text{m}$.

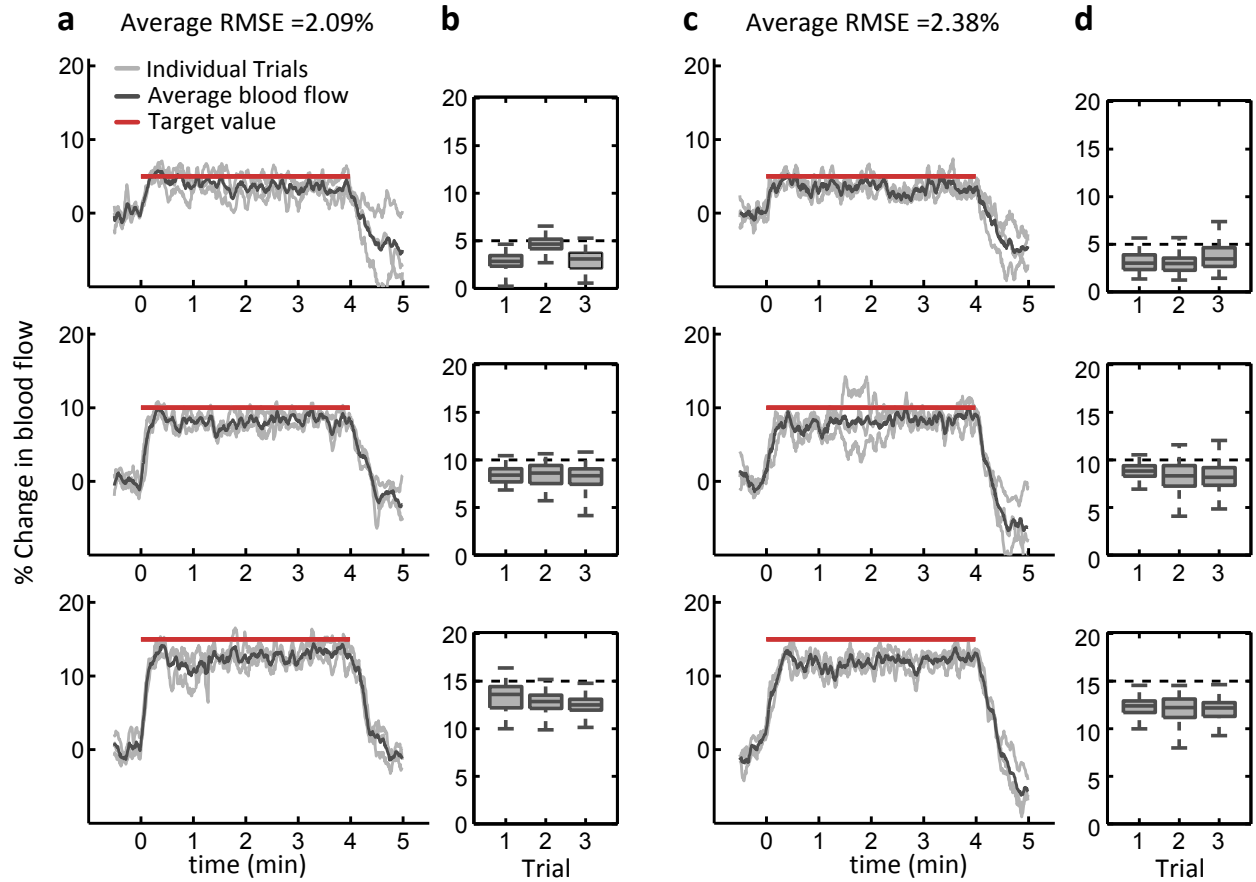


Figure S11: Comparison between the Kalman and moving average pulsation removal filters used in the closed-loop brain control tests. (a) Maintaining blood flow at three different levels when removing pulsations of cardiac cycle by a Kalman filter. Each experiment was repeated three times to ensure repeatability. (b) The box plot of the percentile blood flow change for the last two minutes of each control trial. The center line shows the median, the whiskers are the maximum and minimum, and the box edges are the 25th and 75th percentiles of the data. (c) The same figures as (a) but for the case when we used length-locked moving average algorithm to remove the heart pulsation. (d) The box plots of the data for the last two minutes of control sessions.

Chapter 6

Discussion & Future Directions

6.1 Introduction

Understanding the response of cerebrovascular system to changes in brain activity under healthy and pathological conditions is essential for the basic understanding of blood flow regulatory mechanism in brain and interpretation of functional data that are collected by different advanced functional imaging techniques such as fMRI. This importance motivated me to pursue my PhD in developing proper mechanisms for study of brain vasodynamics.

Design and implementation of an all optical system to interrogate vasodynamics in brain of small rodents was the research scope of the previous chapters in my dissertation. The primary goal of such system is to induce brain stimulation and record hemodynamics by solely using light. Moreover, the device is designed to offer a mechanism for optical recording of neuronal activity. Therefore, all optical interrogation of vasodynamics can be considered as a versatile and minimally invasive approach for study of cerebral vasodynamics.

In order to achieve these goals three different technologies were combined in a single unit. Optical coherence tomography, which has proven to be an effective method of cerebrovascular imaging through a thin layer of bone, was selected as a tool for recording cerebral vasodynamics. The OCT scanner was designed to operate at shortwave infrared spectrum to be used along with optogenetics technology which uses visible light to stimulate/inhibit activity of certain cell populations. To optically record neuronal activity we utilized fluorescence imaging technique in combination with genetically embedded calcium indicators.

6.2 System design

To combine these three technologies, at first a custom-made OCT and a scan/tube lens mechanism (Figures 3.6 and 3.7) were developed. Software and hardware design of this system was presented in the first few chapters of this dissertation. The custom-made OCT offers an imaging resolution of $\sim 5\mu m$ (Figures 3.12 and 3.23). It is capable of imaging cortical vascular network as well as measuring blood velocity across the lumen of pial vessels (Figures 3.20 and 4.4). The OCT system is able to monitor cross section of up to 5 vessels at a rate of 40 frames per second. This speed is sufficient to avoid aliasing that can be introduced by heart pulsations during arterial flow measurements.

The scan/tube lens mechanism provided sufficient space between galvanometric mirrors and the objective lens to incorporate a dichroic mirror and combine a visible path with our OCT. The visible path (Figure 3.7) in the system allows for optogenetic stimulation or fluorescence imaging. By incorporating a set of galvanometric mirrors in the visible path of the device we had precise control on the timing and spatial pattern of the stimulation light. The flexibility in the photostimulation pattern allowed us to design new procedures to measure the effect of distance to vessel on the evoked vasodynamics.

The fluorescence imaging path in the system is capable of detecting and quantifying changes in the fluorescence signal of calcium indicator (GCaMP6) during brain stimulation. This capacity is particularly important to study the correlation between timing and spatial distribution of vasodynamics and neuronal activity. Another application of this path in the system is to guide the OCT system to target the vessels of interest. Since OCT uses infrared beam, this feature proved to be very important in practice.

6.3 Analysis of results

By using the proposed system we investigated different spatio-temporal properties in vascular blood flow, blood velocity, and diameter following brain stimulation. Our findings were in good agreement with previous reports that used fMRI, OISI and LSCI to image response of cerebral hemodynamics to optogenetic or electrical brain stimulation. For a photostimulation with a duration between 1sec and 12sec we observed a bi-phasic response in the arterial blood flow. The length and amplitude of second phase of the response was mainly modulated by the length of the stimulations. The strength of blood flow response, which was defined as the average increase in blood flow up to 20 seconds after stimulation onset, exhibited a linear relationship with the volume of activation.

We also studied the effect of stimulation spatial configuration on the evoked response. By applying multiple stimulation we demonstrated that the arterial blood flow response is a superposition of the response to individual stimulations. As expected, increasing the distance between stimulation site and the vessel of interest, caused a decrease in the amplitude of arterial blood flow, blood velocity and diameter response. Noticeably, stimulating an area far from a vessel could result in a drop in the velocity and flow of the vessel. This drop can be the drive behind drop in the blood oxygenation level in the surrounding tissue that has been reported by other groups. Importantly, we observed that flow changes in a vessel are not necessarily coherent with its diameter changes. We had several observations in which an stimulation induced flow and velocity decrease in a vessel, while causing a dilation in the same vessel. This can be explained by endothelial signaling or other possible signaling mechanisms in the vessel. However, more studies are essential to discern the reason for reduction in arterial blood flow that is feeding the off-target regions of brain tissue, or to get more insight toward the cause of in-coherency in flow and diameter responses in a vessel.

Our findings in this research allowed us to offer a PID mechanism to control blood flow in desired arteries. The stimulation mechanism was able to maintain the blood flow at various user defined levels by adjusting stimulation pulse width. The PID parameters (proportional,

integrator, and derivative gains), were tuned until a close to critically damped response in the blood flow was observed. Then the same parameters were used for the rest of the animals and similar close to critically damped response was observed in these animals. This observation may hint that the relation between vascular flow and an exogenous input can be expressed by similar dynamics across different animals. This hypothesis needs to be further investigated by developing a mathematical model that describes the relationship between brain stimulation and evoked arterial flow response.

6.4 Future directions

Currently our observations are limited to pial arteries and we did not study response of parenchymal arterioles or capillary networks. The latter vascular compartments are smaller than pial vessels in diameter and are believed to be the main source of flow resistance in the blood circulatory mechanism. Generally, the imaging resolution of OCT angiography techniques is limited to a few microns which is not proper for diameter measurement of small arterioles or capillaries. Integrating OCT with multi-photon microscopy can surpass the resolution barrier and provide information about dilation level at capillaries and penetrating arterioles in addition to larger pial vessels. Studying amplitude and timing of response at different vascular compartments can provide a more comprehensive insight into the vasodynamics during brain activation.

Optogenetics technology allows for stimulation and/or inhibition of different cell-types. In this dissertation we stimulated excitatory neurons; however, study of vasodynamics under inhibition of excitatory or excitation of inhibitory neurons can be very informative in understanding the role of different cell population in the cerebral blood flow regulatory mechanism. Some research groups have started similar studies and they have already reported that inhibition of inhibitory neurons causes vasodilation which is usually an effect of excitatory neuron stimulus. These studies can be further expanded by investigating the vascular blood

flow or blood velocity responses while stimulating/inhibiting different cell populations. Concurrent recording of cerebral blood flow (e.g. by using LSCI) and blood oxygenation (e.g. by using OISI or fMRI) along with OCT vascular measurements and GCaMP activity recording can form an information rich dataset. Analysis of the correlation between such a variety of hemodynamic and neuronal activity signals can reveal part of the complex interrelationship between different hemodynamic measures. There are wide variety of different hemodynamic studies where each uses a particular imaging mechanism. Due to the difference between their recording mechanisms, a direct comparison of different studies is not a straightforward task. Understanding this relationship may open a path to compare results that are obtained via different hemodynamic imaging techniques. Moreover, a rich and multi-modal dataset can shed light on the source of the post stimulus drop in blood oxygenation level that has been observed by several research groups.

Developing a mathematical model that describes arterial blood flow or diameter dynamics as a function of stimulation configuration has a profound influence on our basic understanding of the vasodynamics in brain. A proper and accurate model can be also used to create new hypotheses and design in-vivo experiments to verify them. Potential benefit of this model spans from discerning different characteristics of functional imaging results such as fMRI BOLD signal, to investigating the disruption in the regulatory mechanisms under different pathological conditions. We anticipate by developing a proper model to capture the dependency between stimulation configuration and arterial response it is possible to design optical stimulation pattern to create an arbitrary blood flow distribution in the brain in an open-loop manner. The same modeling can also help to improve the accuracy and efficiency of future closed-loop controllers.

BIBLIOGRAPHY

- [1] K. Deisseroth, “Optogenetics,” *Nat Meth* **8**, 26–29 (2011). Commentary.
- [2] G. Nagel, T. Szellas, W. Huhn, S. Kateriya, N. Adeishvili, P. Berthold, D. Ollig, P. Hegemann, and E. Bamberg, “Channelrhodopsin-2, a directly light-gated cation-selective membrane channel,” *Proceedings of the National Academy of Sciences* **100**, 13940–13945 (2003).
- [3] F. Zhang, L.-P. Wang, M. Brauner, J. F. Liewald, K. Kay, N. Watzke, P. G. Wood, E. Bamberg, G. Nagel, A. Gottschalk, and K. Deisseroth, “Multimodal fast optical interrogation of neural circuitry,” *Nature* **446**, 633–639 (2007).
- [4] E. S. Boyden, F. Zhang, E. Bamberg, G. Nagel, and K. Deisseroth, “Millisecond-timescale, genetically targeted optical control of neural activity,” *Nat Neurosci* **8**, 1263–1268 (2005).
- [5] F. Zhang, A. M. Aravanis, A. Adamantidis, L. de Lecea, and K. Deisseroth, “Circuit-breakers: optical technologies for probing neural signals and systems,” *Nat Rev Neurosci* **8**, 577–581 (2007).
- [6] V. Gradinaru, M. Mogri, K. R. Thompson, J. M. Henderson, and K. Deisseroth, “Optical deconstruction of parkinsonian neural circuitry,” *Science* **324**, 354–359 (2009).
- [7] V. Gradinaru, K. R. Thompson, and K. Deisseroth, “enphr: a natronomonas halorhodopsin enhanced for optogenetic applications,” *Brain Cell Biology* **36**, 129–139 (2008).
- [8] O. G. S. Ayling, T. C. Harrison, J. D. Boyd, A. Goroshkov, and T. H. Murphy, “Automated light-based mapping of motor cortex by photoactivation of channelrhodopsin-2 transgenic mice,” *Nat Meth* **6**, 219–224 (2009).

- [9] J. H. Lee, R. Durand, V. Gradinaru, F. Zhang, I. Goshen, D.-S. Kim, L. E. Fenno, C. Ramakrishnan, and K. Deisseroth, “Global and local fmri signals driven by neurons defined optogenetically by type and wiring,” *Nature* **465**, 788–792 (2010).
- [10] I. Kahn, M. Desai, U. Knoblich, J. Bernstein, M. Henninger, A. M. Graybiel, E. S. Boyden, R. L. Buckner, and C. I. Moore, “Characterization of the functional mri response temporal linearity via optical control of neocortical pyramidal neurons,” *Journal of Neuroscience* **31**, 15086–15091 (2011).
- [11] I. Kahn, U. Knoblich, M. Desai, J. Bernstein, A. Graybiel, E. Boyden, R. Buckner, and C. Moore, “Optogenetic drive of neocortical pyramidal neurons generates fmri signals that are correlated with spiking activity,” *Brain Research* **1511**, 33 – 45 (2013).
Optogenetics and Pharmacogenetics in Neuronal Function and Dysfunction.
- [12] B. Iordanova, A. L. Vazquez, A. J. Poplawsky, M. Fukuda, and S.-G. Kim, “Neural and hemodynamic responses to optogenetic and sensory stimulation in the rat somatosensory cortex,” *Journal of Cerebral Blood Flow & Metabolism* **35**, 922–932 (2015). PMID: 25669905.
- [13] N. A. Scott and T. H. Murphy, “Hemodynamic responses evoked by neuronal stimulation via channelrhodopsin-2 can be independent of intracortical glutamatergic synaptic transmission,” *PLOS ONE* **7**, 1–10 (2012).
- [14] R. D. Frostig, E. E. Lieke, D. Y. Ts’o, and A. Grinvald, “Cortical functional architecture and local coupling between neuronal activity and the microcirculation revealed by in vivo high-resolution optical imaging of intrinsic signals.” *Proceedings of the National Academy of Sciences* **87**, 6082–6086 (1990).
- [15] A. L. Vazquez, M. Fukuda, J. C. Crowley, and S.-G. Kim, “Neural and hemodynamic responses elicited by forelimb- and photo-stimulation in channelrhodopsin-2 mice: In-

- sights into the hemodynamic point spread function,” *Cerebral Cortex* **24**, 2908–2919 (2014).
- [16] G. C. Petzold and V. N. Murthy, “Role of astrocytes in neurovascular coupling,” *Neuron* **71**, 782 – 797 (2011).
- [17] M. Desai, I. Kahn, U. Knoblich, J. Bernstein, H. Atallah, A. Yang, N. Kopell, R. L. Buckner, A. M. Graybiel, C. I. Moore, and E. S. Boyden, “Mapping brain networks in awake mice using combined optical neural control and fmri,” *Journal of Neurophysiology* **105**, 1393–1405 (2011).
- [18] L. Ji, J. Zhou, R. Zafar, S. Kantorovich, R. Jiang, P. R. Carney, and H. Jiang, “Cortical neurovascular coupling driven by stimulation of channelrhodopsin-2,” *PLOS ONE* **7**, 1–10 (2012).
- [19] P. J. Drew, A. Y. Shih, and D. Kleinfeld, “Fluctuating and sensory-induced vasodynamics in rodent cortex extend arteriole capacity,” *Proceedings of the National Academy of Sciences* **108**, 8473–8478 (2011).
- [20] A. Y. Shih, J. D. Driscoll, P. J. Drew, N. Nishimura, C. B. Schaffer, and D. Kleinfeld, “Two-photon microscopy as a tool to study blood flow and neurovascular coupling in the rodent brain,” *Journal of Cerebral Blood Flow & Metabolism* **32**, 1277–1309 (2012). PMID: 22293983.
- [21] H. Uhlirova, K. Kl, P. Tian, M. Thunemann, M. Desjardins, P. A. Saisan, S. Sakadi, T. V. Ness, C. Mateo, Q. Cheng, K. L. Weldy, F. Razoux, M. Vandenberghe, J. A. Cremonesi, C. G. Ferri, K. Nizar, V. B. Sridhar, T. C. Steed, M. Abashin, Y. Fainman, E. Masliah, S. Djurovic, O. A. Andreassen, G. A. Silva, D. A. Boas, D. Kleinfeld, R. B. Buxton, G. T. Einevoll, A. M. Dale, and A. Devor, “Cell type specificity of neurovascular coupling in cerebral cortex,” *eLife* **5**, e14315 (2016).

- [22] K. Masamoto, M. Unekawa, T. Watanabe, H. Toriumi, H. Takuwa, H. Kawaguchi, I. Kanno, K. Matsui, K. F. Tanaka, Y. Tomita, and N. Suzuki, “Unveiling astrocytic control of cerebral blood flow with optogenetics,” **5**, 11455 EP – (2015). Article.
- [23] A. Nimmerjahn, E. A. Mukamel, and M. J. Schnitzer, “Motor behavior activates bergmann glial networks,” *Neuron* **62**, 400 – 412 (2009).
- [24] J. Schummers, H. Yu, and M. Sur, “Tuned responses of astrocytes and their influence on hemodynamic signals in the visual cortex,” *Science* **320**, 1638–1643 (2008).
- [25] D. Huang, E. Swanson, C. Lin, J. Schuman, W. Stinson, W. Chang, M. Hee, T. Flotte, K. Gregory, C. Puliafito, and a. et, “Optical coherence tomography,” *Science* **254**, 1178–1181 (1991).
- [26] F. I. Feldchtein, G. V. Gelikonov, V. M. Gelikonov, R. R. Iksanov, R. V. Kuranov, A. M. Sergeev, N. D. Gladkova, M. N. Ourutina, J. A. Warren, and D. H. Reitze, “In vivo oct imaging of hard and soft tissue of the oral cavity,” *Opt. Express* **3**, 239–250 (1998).
- [27] S. H. Yun, G. J. Tearney, J. F. de Boer, N. Iftimia, and B. E. Bouma, “High-speed optical frequency-domain imaging,” *Opt. Express* **11**, 2953–2963 (2003).
- [28] Z. Yaqoob, J. Wu, E. J. McDowell, X. Heng, and C. Yang, “Methods and application areas of endoscopic optical coherence tomography,” *Journal of Biomedical Optics* **11**, 063001–063001–19 (2006).
- [29] S. Meissner, L. Knels, A. Krueger, T. Koch, and E. Koch, “Simultaneous three-dimensional optical coherence tomography and intravital microscopy for imaging subpleural pulmonary alveoli in isolated rabbit lungs,” *Journal of Biomedical Optics* **14**, 054020–054020–6 (2009).

- [30] H. G. Bezerra, M. A. Costa, G. Guagliumi, A. M. Rollins, and D. I. Simon, “Intracoronary optical coherence tomography: A comprehensive review,” *JACC: Cardiovascular Interventions* **2**, 1035 – 1046 (2009).
- [31] T. Gambichler, V. Jaedicke, and S. Terras, “Optical coherence tomography in dermatology: technical and clinical aspects,” *Archives of Dermatological Research* **303**, 457–473 (2011).
- [32] L. An, J. Chao, M. Johnstone, and R. K. Wang, “Noninvasive imaging of pulsatile movements of the optic nerve head in normal human subjects using phase-sensitive spectral domain optical coherence tomography,” *Opt. Lett.* **38**, 1512–1514 (2013).
- [33] Y. Zhao, Z. Chen, C. Saxer, Q. Shen, S. Xiang, J. F. de Boer, and J. S. Nelson, “Doppler standard deviation imaging for clinical monitoring of in vivo human skin blood flow,” *Opt. Lett.* **25**, 1358–1360 (2000).
- [34] L. Wang, Y. Wang, S. Guo, J. Zhang, M. Bachman, G. Li, and Z. Chen, “Frequency domain phase-resolved optical doppler and doppler variance tomography,” *Optics Communications* **242**, 345 – 350 (2004).
- [35] S. Makita, Y. Hong, M. Yamanari, T. Yatagai, and Y. Yasuno, “Optical coherence angiography,” *Opt. Express* **14**, 7821–7840 (2006).
- [36] B. J. Vakoc, R. M. Lanning, J. A. Tyrrell, T. P. Padera, L. A. Bartlett, T. Stylianopoulos, L. L. Munn, G. J. Tearney, D. Fukumura, R. K. Jain, and B. E. Bouma, “Three-dimensional microscopy of the tumor microenvironment in vivo using optical frequency domain imaging,” *Nat Med* **15**, 1219–1223 (2009).
- [37] R. K. Wang, S. L. Jacques, Z. Ma, S. Hurst, S. R. Hanson, and A. Gruber, “Three dimensional optical angiography,” *Opt. Express* **15**, 4083–4097 (2007).

- [38] V. J. Srinivasan, E. T. Mandeville, A. Can, F. Blasi, M. Climov, A. Daneshmand, J. H. Lee, E. Yu, H. Radhakrishnan, E. H. Lo, S. Sakadi, K. Eikermann-Haerter, and C. Ayata, “Multiparametric, longitudinal optical coherence tomography imaging reveals acute injury and chronic recovery in experimental ischemic stroke,” *PLOS ONE* **8**, 1–14 (2013).
- [39] J. A. Izatt, M. D. Kulkarni, S. Yazdanfar, J. K. Barton, and A. J. Welch, “In vivo bidirectional color doppler flow imaging of picoliter blood volumes using optical coherence tomography,” *Opt. Lett.* **22**, 1439–1441 (1997).
- [40] Y. Zhao, Z. Chen, C. Saxer, S. Xiang, J. F. de Boer, and J. S. Nelson, “Phase-resolved optical coherence tomography and optical doppler tomography for imaging blood flow in human skin with fast scanning speed and high velocity sensitivity,” *Opt. Lett.* **25**, 114–116 (2000).
- [41] R. Leitgeb, C. K. Hitzenberger, and A. F. Fercher, “Performance of fourier domain vs. time domain optical coherence tomography,” *Opt. Express* **11**, 889–894 (2003).
- [42] B. J. Vakoc, S. H. Yun, J. F. de Boer, G. J. Tearney, and B. E. Bouma, “Phase-resolved optical frequency domain imaging,” *Opt. Express* **13**, 5483–5493 (2005).
- [43] A. M. Davis, F. G. Rothenberg, N. Shepherd, and J. A. Izatt, “In vivo spectral domain optical coherence tomography volumetric imaging and spectral doppler velocimetry of early stage embryonic chicken heart development,” *J. Opt. Soc. Am. A* **25**, 3134–3143 (2008).
- [44] M. Szkulmowski, A. Szkulmowska, T. Bajraszewski, A. Kowalczyk, and M. Wojtkowski, “Flow velocity estimation using joint spectral and time domain optical coherence tomography,” *Opt. Express* **16**, 6008–6025 (2008).
- [45] R. K. Wang and L. An, “Doppler optical micro-angiography for volumetric imaging of vascular perfusion in vivo,” *Opt. Express* **17**, 8926–8940 (2009).

- [46] J. A. Izatt, M. D. Kulkarni, H.-W. Wang, K. Kobayashi, and M. V. Sivak, "Optical coherence tomography and microscopy in gastrointestinal tissues," *IEEE Journal of Selected Topics in Quantum Electronics* **2**, 1017–1028 (1996).
- [47] A. Fercher, C. Hitzenberger, G. Kamp, and S. El-Zaiat, "Measurement of intraocular distances by backscattering spectral interferometry," *Optics Communications* **117**, 43–48 (1995).
- [48] G. Hausler and M. W. Lindner, "coherence radar and spectral radarnew tools for dermatological diagnosis," *Journal of Biomedical Optics* **3**, 21–31 (1998).
- [49] J. M. Schmitt, "Optical coherence tomography (oct): a review," *IEEE Journal of Selected Topics in Quantum Electronics* **5**, 1205–1215 (1999).
- [50] C. Dorrer, N. Belabas, J.-P. Likforman, and M. Joffre, "Spectral resolution and sampling issues in fourier-transform spectral interferometry," *J. Opt. Soc. Am. B* **17**, 1795–1802 (2000).
- [51] M. Wojtkowski, R. Leitgeb, A. Kowalczyk, T. Bajraszewski, and A. F. Fercher, "In vivo human retinal imaging by fourier domain optical coherence tomography," *Journal of Biomedical Optics* **7**, 457–463 (2002).
- [52] M. A. Choma, M. V. Sarunic, C. Yang, and J. A. Izatt, "Sensitivity advantage of swept source and fourier domain optical coherence tomography," *Opt. Express* **11**, 2183–2189 (2003).
- [53] A. F. Fercher, W. Drexler, C. K. Hitzenberger, and T. Lasser, "Optical coherence tomography - principles and applications," *Reports on Progress in Physics* **66**, 239 (2003).
- [54] J. F. de Boer, B. Cense, B. H. Park, M. C. Pierce, G. J. Tearney, and B. E. Bouma,

- “Improved signal-to-noise ratio in spectral-domain compared with time-domain optical coherence tomography,” *Opt. Lett.* **28**, 2067–2069 (2003).
- [55] B. Cense, N. A. Nassif, T. C. Chen, M. C. Pierce, S.-H. Yun, B. H. Park, B. E. Bouma, G. J. Tearney, and J. F. de Boer, “Ultrahigh-resolution high-speed retinal imaging using spectral-domain optical coherence tomography,” *Opt. Express* **12**, 2435–2447 (2004).
- [56] M. Wojtkowski, V. J. Srinivasan, T. H. Ko, J. G. Fujimoto, A. Kowalczyk, and J. S. Duker, “Ultrahigh-resolution, high-speed, fourier domain optical coherence tomography and methods for dispersion compensation,” *Opt. Express* **12**, 2404–2422 (2004).
- [57] P. H. Tomlins and R. K. Wang, “Theory, developments and applications of optical coherence tomography,” *Journal of Physics D: Applied Physics* **38**, 2519 (2005).
- [58] W. Drexler and J. G. Fujimoto, *Optical Coherence Tomography* (Springer International Publishing, 2008), 1st ed.
- [59] F. E. Robles, S. Chowdhury, and A. Wax, “Assessing hemoglobin concentration using spectroscopic optical coherence tomography for feasibility of tissue diagnostics,” *Biomed. Opt. Express* **1**, 310–317 (2010).
- [60] J. Yi and X. Li, “Estimation of oxygen saturation from erythrocytes by high-resolution spectroscopic optical coherence tomography,” *Opt. Lett.* **35**, 2094–2096 (2010).
- [61] F. E. Robles, C. Wilson, G. Grant, and A. Wax, “Molecular imaging true-colour spectroscopic optical coherence tomography,” *Nat Photon* **5**, 744–747 (2011).
- [62] J. Yi, Q. Wei, W. Liu, V. Backman, and H. F. Zhang, “Visible-light optical coherence tomography for retinal oximetry,” *Opt. Lett.* **38**, 1796–1798 (2013).
- [63] S. Ishida, N. Nishizawa, T. Ohta, and K. Itoh, “Ultrahigh-resolution optical coherence

- tomography in 1.7 m region with fiber laser supercontinuum in low-water-absorption samples,” *Applied Physics Express* **4**, 052501 (2011).
- [64] S. Ishida and N. Nishizawa, “Quantitative comparison of contrast and imaging depth of ultrahigh-resolution optical coherence tomography images in 800–1700 nm wavelength region,” *Biomed. Opt. Express* **3**, 282–294 (2012).
- [65] Y. Hattori, H. Kawagoe, Y. Ando, M. Yamanaka, and N. Nishizawa, “High-speed ultrahigh-resolution spectral domain optical coherence tomography using high-power supercontinuum at 0.8 m wavelength,” *Applied Physics Express* **8**, 082501 (2015).
- [66] Z. Hu and A. M. Rollins, “Theory of two beam interference with arbitrary spectra,” *Opt. Express* **14**, 12751–12759 (2006).
- [67] Z. Hu, Y. Pan, and A. M. Rollins, “Analytical model of spectrometer-based two-beam spectral interferometry,” *Appl. Opt.* **46**, 8499–8505 (2007).
- [68] Z. Hu and A. M. Rollins, “Quasi-telecentric optical design of a microscope-compatible oct scanner,” *Opt. Express* **13**, 6407–6415 (2005).
- [69] E. H. K. Stelzer, *The Intermediate Optical System of Laser-Scanning Confocal Microscopes* (Springer US, Boston, MA, 2006), pp. 207–220.
- [70] A. Negrean and H. D. Mansvelder, “Optimal lens design and use in laser-scanning microscopy,” *Biomed. Opt. Express* **5**, 1588–1609 (2014).
- [71] M. Hafez, T. Sidler, and R.-P. Salathe, “Study of the beam path distortion profiles generated by a two-axis tilt single-mirror laser scanner,” *Optical Engineering* **42**, 1048–1057 (2003).
- [72] J. Y. Kim, C. Lee, K. Park, G. Lim, and C. Kim, “Fast optical-resolution photoacoustic microscopy using a 2-axis water-proofing mems scanner,” *Scientific Reports* **5**, 7932 EP – (2015). Article.

- [73] B. E. A. Saleh and M. C. Teich, *Fundamentals of photonics* (Wiley, 2007).
- [74] R. A. Leitgeb, M. Villiger, A. H. Bachmann, L. Steinmann, and T. Lasser, “Extended focus depth for fourier domain optical coherence microscopy,” *Opt. Lett.* **31**, 2450–2452 (2006).
- [75] K.-S. Lee and J. P. Rolland, “Bessel beam spectral-domain high-resolution optical coherence tomography with micro-optic axicon providing extended focusing range,” *Opt. Lett.* **33**, 1696–1698 (2008).
- [76] S. Tamborski, H. C. Lyu, H. Dolezyczek, M. Malinowska, G. Wilczynski, D. Szlag, T. Lasser, M. Wojtkowski, and M. Szkulmowski, “Extended-focus optical coherence microscopy for high-resolution imaging of the murine brain,” *Biomed. Opt. Express* **7**, 4400–4414 (2016).
- [77] F. Atry and R. Pashaie, “Analysis of intermediary scan-lens and tube-lens mechanisms for optical coherence tomography,” *Appl. Opt.* **55**, 646–653 (2016).
- [78] T. Bajraszewski, M. Wojtkowski, M. Szkulmowski, A. Szkulmowska, R. Huber, and A. Kowalczyk, “Improved spectral optical coherence tomography using optical frequency comb,” *Opt. Express* **16**, 4163–4176 (2008).
- [79] V. Fathipour, A. Bonakdar, and H. Mohseni, “Advances on sensitive electron-injection based cameras for low-flux, short-wave infrared applications,” *Frontiers in Materials* **3**, 33 (2016).
- [80] V. M. Gelikonov, G. V. Gelikonov, and P. A. Shilyagin, “Linear-wavenumber spectrometer for high-speed spectral-domain optical coherence tomography,” *Optics and Spectroscopy* **106**, 459–465 (2009).
- [81] B. R. White, M. C. Pierce, N. Nassif, B. Cense, B. H. Park, G. J. Tearney, B. E. Bouma, T. C. Chen, and J. F. de Boer, “In vivo dynamic human retinal blood flow

- imaging using ultra-high-speed spectral domain optical doppler tomography,” *Opt. Express* **11**, 3490–3497 (2003).
- [82] R. Leitgeb, L. F. Schmetterer, M. Wojtkowski, C. K. Hitzenberger, M. Sticker, and A. F. Fercher, “Flow velocity measurements by frequency domain short coherence interferometry,” (2002).
- [83] R. A. Leitgeb, L. Schmetterer, W. Drexler, A. F. Fercher, R. J. Zawadzki, and T. Bajraszewski, “Real-time assessment of retinal blood flow with ultrafast acquisition by color doppler fourier domain optical coherence tomography,” *Opt. Express* **11**, 3116–3121 (2003).
- [84] A. Szkulmowska, M. Szkulmowski, A. Kowalczyk, and M. Wojtkowski, “Phase-resolved doppler optical coherence tomography—limitations and improvements,” *Opt. Lett.* **33**, 1425–1427 (2008).
- [85] H. Ren, T. Sun, D. J. MacDonald, M. J. Cobb, and X. Li, “Real-time in vivo blood-flow imaging by moving-scatterer-sensitive spectral-domain optical doppler tomography,” *Opt. Lett.* **31**, 927–929 (2006).
- [86] A. C. Chan, E. Y. Lam, and V. J. Srinivasan, “Comparison of kasai autocorrelation and maximum likelihood estimators for doppler optical coherence tomography,” *IEEE Transactions on Medical Imaging* **32**, 1033–1042 (2013).
- [87] Y. Wang and R. Wang, “Autocorrelation optical coherence tomography for mapping transverse particle-flow velocity,” *Opt. Lett.* **35**, 3538–3540 (2010).
- [88] J. Lee, W. Wu, J. Y. Jiang, B. Zhu, and D. A. Boas, “Dynamic light scattering optical coherence tomography,” *Opt. Express* **20**, 22262–22277 (2012).
- [89] J. Lee, H. Radhakrishnan, W. Wu, A. Daneshmand, M. Climov, C. Ayata, and D. A. Boas, “Quantitative imaging of cerebral blood flow velocity and intracellular motil-

- ity using dynamic light scattering optical coherence tomography,” *Journal of Cerebral Blood Flow & Metabolism* **33**, 819–825 (2013). PMID: 23403378.
- [90] V. J. Srinivasan, H. Radhakrishnan, E. H. Lo, E. T. Mandeville, J. Y. Jiang, S. Barry, and A. E. Cable, “Oct methods for capillary velocimetry,” *Biomed. Opt. Express* **3**, 612–629 (2012).
- [91] J. Lee, W. Wu, F. Lesage, and D. A. Boas, “Multiple-capillary measurement of rbc speed, flux, and density with optical coherence tomography,” *Journal of Cerebral Blood Flow & Metabolism* **33**, 1707–1710 (2013). PMID: 24022621.
- [92] B. H. Park, M. C. Pierce, B. Cense, S.-H. Yun, M. Mujat, G. J. Tearney, B. E. Bouma, and J. F. de Boer, “Real-time fiber-based multi-functional spectral-domain optical coherence tomography at 1.3 μm ,” *Opt. Express* **13**, 3931–3944 (2005).
- [93] J. Fingler, D. Schwartz, C. Yang, and S. E. Fraser, “Mobility and transverse flow visualization using phase variance contrast with spectral domain optical coherence tomography,” *Opt. Express* **15**, 12636–12653 (2007).
- [94] L. Yu and Z. Chen, “Doppler variance imaging for three-dimensional retina and choroid angiography,” *Journal of Biomedical Optics* **15**, 016029–016029–4 (2010).
- [95] A. Mariampillai, B. A. Standish, E. H. Moriyama, M. Khurana, N. R. Munce, M. K. K. Leung, J. Jiang, A. Cable, B. C. Wilson, I. A. Vitkin, and V. X. D. Yang, “Speckle variance detection of microvasculature using swept-source optical coherence tomography,” *Opt. Lett.* **33**, 1530–1532 (2008).
- [96] X. Liu, M. Balicki, R. H. Taylor, and J. U. Kang, “Automatic online spectral calibration of fourier-domain oct for robotic surgery,” (2011).
- [97] W. Choi, K. J. Mohler, B. Potsaid, C. D. Lu, J. J. Liu, V. Jayaraman, A. E. Cable, J. S.

- Duker, R. Huber, and J. G. Fujimoto, "Choriocapillaris and choroidal microvasculature imaging with ultrahigh speed oct angiography," *PLOS ONE* **8**, 1–8 (2013).
- [98] R. K. Wang and S. Hurst, "Mapping of cerebro-vascular blood perfusion in mice with skin and skull intact by optical micro-angiography at $1.3\mu\text{m}$ wavelength," *Opt. Express* **15**, 11402–11412 (2007).
- [99] V. J. Srinivasan, S. Sakadžić, I. Gorczynska, S. Ruvinskaya, W. Wu, J. G. Fujimoto, and D. A. Boas, "Quantitative cerebral blood flow with optical coherence tomography," *Opt. Express* **18**, 2477–2494 (2010).
- [100] V. J. Srinivasan, J. Y. Jiang, M. A. Yaseen, H. Radhakrishnan, W. Wu, S. Barry, A. E. Cable, and D. A. Boas, "Rapid volumetric angiography of cortical microvasculature with optical coherence tomography," *Opt. Lett.* **35**, 43–45 (2010).
- [101] J. Enfield, E. Jonathan, and M. Leahy, "In vivo imaging of the microcirculation of the volar forearm using correlation mapping optical coherence tomography (cmoct)," *Biomed. Opt. Express* **2**, 1184–1193 (2011).
- [102] E. Jonathan, J. Enfield, and M. J. Leahy, "Correlation mapping method for generating microcirculation morphology from optical coherence tomography (oct) intensity images," *Journal of Biophotonics* **4**, 583–587 (2011).
- [103] P. D. Woolliams and P. H. Tomlins, "Estimating the resolution of a commercial optical coherence tomography system with limited spatial sampling," *Measurement Science and Technology* **22**, 065502 (2011).
- [104] A. Fouad, T. J. Pfefer, C.-W. Chen, W. Gong, A. Agrawal, P. H. Tomlins, P. D. Woolliams, R. A. Drezek, and Y. Chen, "Variations in optical coherence tomography resolution and uniformity: a multi-system performance comparison," *Biomed. Opt. Express* **5**, 2066–2081 (2014).

- [105] M. R. N. Avanaki, A. G. Podoleanu, M. C. Price, S. A. Corr, and S. A. Hojjatoleslami, “Two applications of solid phantoms in performance assessment of optical coherence tomography systems,” *Appl. Opt.* **52**, 7054–7061 (2013).
- [106] A. Agrawal, T. J. Pfefer, N. Gilani, and R. Drezek, “Three-dimensional characterization of optical coherence tomography point spread functions with a nanoparticle-embedded phantom,” *Opt. Lett.* **35**, 2269–2271 (2010).
- [107] G. Nootz, “Fit 2d gaussian function to data, (matlab central file exchange, 2012),” (2012).
- [108] D.-W. Park, A. A. Schendel, S. Mikael, S. K. Brodnick, T. J. Richner, J. P. Ness, M. R. Hayat, F. Atry, S. T. Frye, R. Pashaie, S. Thongpang, Z. Ma, and J. C. Williams, “Graphene-based carbon-layered electrode array technology for neural imaging and optogenetic applications,” **5**, 5258 EP – (2014). Article.
- [109] D.-W. Park, S. K. Brodnick, J. P. Ness, F. Atry, L. Krugner-Higby, A. Sandberg, S. Mikael, T. J. Richner, J. Novello, H. Kim, D.-H. Baek, J. Bong, S. T. Frye, S. Thongpang, K. I. Swanson, W. Lake, R. Pashaie, J. C. Williams, and Z. Ma, “Fabrication and utility of a transparent graphene neural electrode array for electrophysiology, in vivo imaging, and optogenetics,” *Nat. Protocols* **11**, 2201–2222 (2016). Protocol.
- [110] T.-W. Chen, T. J. Wardill, Y. Sun, S. R. Pulver, S. L. Renninger, A. Baohan, E. R. Schreiter, R. A. Kerr, M. B. Orger, V. Jayaraman, L. L. Looger, K. Svoboda, and D. S. Kim, “Ultrasensitive fluorescent proteins for imaging neuronal activity,” *Nature* **499**, 295–300 (2013). Article.
- [111] S. Moon, S.-W. Lee, and Z. Chen, “Reference spectrum extraction and fixed-pattern noise removal in optical coherence tomography,” *Opt. Express* **18**, 24395–24404 (2010).
- [112] V. J. Srinivasan, H. Radhakrishnan, J. Y. Jiang, S. Barry, and A. E. Cable, “Optical

- coherence microscopy for deep tissue imaging of the cerebral cortex with intrinsic contrast,” *Opt. Express* **20**, 2220–2239 (2012).
- [113] J. Lee, V. Srinivasan, H. Radhakrishnan, and D. A. Boas, “Motion correction for phase-resolved dynamic optical coherence tomography imaging of rodent cerebral cortex,” *Opt. Express* **19**, 21258–21270 (2011).
- [114] N. K. Logothetis and B. A. Wandell, “Interpreting the bold signal,” *Annual Review of Physiology* **66**, 735–769 (2004). PMID: 14977420.
- [115] B. V. Zemelman, G. A. Lee, M. Ng, and G. Miesenbck, “Selective photostimulation of genetically charged neurons,” *Neuron* **33**, 15 – 22 (2002).
- [116] L. Fenno, O. Yizhar, and K. Deisseroth, “The development and application of optogenetics,” *Annual Review of Neuroscience* **34**, 389–412 (2011). PMID: 21692661.
- [117] R. Pashaie, P. Anikeeva, J. H. Lee, R. Prakash, O. Yizhar, M. Prigge, D. Chander, T. J. Richner, and J. Williams, “Optogenetic brain interfaces,” *IEEE Reviews in Biomedical Engineering* **7**, 3–30 (2014).
- [118] N. A. Nassif, B. Cense, B. H. Park, M. C. Pierce, S. H. Yun, B. E. Bouma, G. J. Tearney, T. C. Chen, and J. F. de Boer, “In vivo high-resolution video-rate spectral-domain optical coherence tomography of the human retina and optic nerve,” *Opt. Express* **12**, 367–376 (2004).
- [119] Z. Zhi, W. Cepurna, E. Johnson, T. Shen, J. Morrison, and R. K. Wang, “Volumetric and quantitative imaging of retinal blood flow in rats with optical microangiography,” *Biomed. Opt. Express* **2**, 579–591 (2011).
- [120] C. Kasai, K. Namekawa, A. Koyano, and R. Omoto, “Real-time two-dimensional blood flow imaging using an autocorrelation technique,” *IEEE Transactions on Sonics and Ultrasonics* **32**, 458–464 (1985).

- [121] V. X. Yang, M. L. Gordon, B. Qi, J. Pekar, S. Lo, E. Seng-Yue, A. Mok, B. C. Wilson, and I. A. Vitkin, “High speed, wide velocity dynamic range doppler optical coherence tomography (part i): System design, signal processing, and performance,” *Opt. Express* **11**, 794–809 (2003).
- [122] P. J. Drew, A. Y. Shih, J. D. Driscoll, P. M. Knutsen, P. Blinder, D. Davalos, K. Akasoglou, P. S. Tsai, and D. Kleinfeld, “Chronic optical access through a polished and reinforced thinned skull,” *Nat Meth* **7**, 981–984 (2010).
- [123] E. M. M. R. C. L. H. M. S. W. Y. O. C. M. I. M. S. P. B. H. B. D. K. Szu, J. I., “Thinned-skull cortical window technique for in vivo optical coherence tomography imaging.” *J. Vis. Exp.* **69** (2012).
- [124] H.-T. Xu, F. Pan, G. Yang, and W.-B. Gan, “Choice of cranial window type for in vivo imaging affects dendritic spine turnover in the cortex,” *Nat Neurosci* **10**, 549–551 (2007).
- [125] J. Y. Lin, M. Z. Lin, P. Steinbach, and R. Y. Tsien, “Characterization of engineered channelrhodopsin variants with improved properties and kinetics,” *Biophysical Journal* **96**, 1803 – 1814 (2009).
- [126] M. Azimipour, R. Baumgartner, Y. Liu, S. L. Jacques, K. Eliceiri, and R. Pashaie, “Extraction of optical properties and prediction of light distribution in rat brain tissue,” *Journal of Biomedical Optics* **19**, 075001 (2014).
- [127] H. Radhakrishnan and V. J. Srinivasan, “Compartment-resolved imaging of cortical functional hyperemia with oct angiography,” *Biomed. Opt. Express* **4**, 1255–1268 (2013).
- [128] D. Attwell and S. B. Laughlin, “An energy budget for signaling in the grey matter of the brain,” *Journal of Cerebral Blood Flow & Metabolism* **21**, 1133–1145 (2001). PMID: 11598490.

- [129] P. J. Magistretti and I. Allaman, “A cellular perspective on brain energy metabolism and functional imaging,” *Neuron* **86**, 883–901 (2015).
- [130] P. G. Haydon and G. Carmignoto, “Astrocyte control of synaptic transmission and neurovascular coupling,” *Physiological Reviews* **86**, 1009–1031 (2006).
- [131] D. Attwell, A. M. Buchan, S. Charpak, M. Lauritzen, B. A. MacVicar, and E. A. Newman, “Glial and neuronal control of brain blood flow,” *Nature* **468**, 232–243 (2010). 21068832[pmid].
- [132] M. D. Sweeney, S. Ayyadurai, and B. V. Zlokovic, “Pericytes of the neurovascular unit: key functions and signaling pathways,” *Nat Neurosci* **19**, 771–783 (2016). Review.
- [133] F. Schmid, L. Wachsmuth, M. Schwalm, P.-H. Prouvot, E. R. Jubal, C. Fois, G. Pramanik, C. Zimmer, C. Faber, and A. Stroh, “Assessing sensory versus optogenetic network activation by combining (o)fmri with optical ca²⁺ recordings,” *Journal of Cerebral Blood Flow & Metabolism* **36**, 1885–1900 (2016). PMID: 26661247.
- [134] F. Atry, S. Frye, T. J. Richner, S. K. Brodnick, A. Soehartono, J. Williams, and R. Pashaie, “Monitoring cerebral hemodynamics following optogenetic stimulation via optical coherence tomography,” *IEEE Transactions on Biomedical Engineering* **62**, 766–773 (2015).
- [135] I. N. Christie, J. A. Wells, P. Southern, N. Marina, S. Kasparov, A. V. Gourine, and M. F. Lythgoe, “fmri response to blue light delivery in the nave brain: Implications for combined optogenetic fmri studies,” *NeuroImage* **66**, 634 – 641 (2013).
- [136] T. J. Richner, R. Baumgartner, S. K. Brodnick, M. Azimipour, L. A. Krugner-Higby, K. W. Eliceiri, J. C. Williams, and R. Pashaie, “Patterned optogenetic modulation of neurovascular and metabolic signals,” *Journal of Cerebral Blood Flow & Metabolism* **35**, 140–147 (2015). PMID: 25388678.

- [137] R. L. Rungta, B.-F. Osmanski, D. Boido, M. Tanter, and S. Charpak, “Light controls cerebral blood flow in naive animals,” *Nature Communications* **8**, 14191 EP – (2017). Article.
- [138] R. Leitgeb, M. Wojtkowski, A. Kowalczyk, C. K. Hitzenberger, M. Sticker, and A. F. Fercher, “Spectral measurement of absorption by spectroscopic frequency-domain optical coherence tomography,” *Opt. Lett.* **25**, 820–822 (2000).
- [139] J. McNames and M. Aboy, “Statistical modeling of cardiovascular signals and parameter estimation based on the extended kalman filter,” *IEEE Transactions on Biomedical Engineering* **55**, 119–129 (2008).
- [140] M. Azimipour, F. Atry, and R. Pashaie, “Effect of blood vessels on light distribution in optogenetic stimulation of cortex,” *Opt. Lett.* **40**, 2173–2176 (2015).
- [141] Y. Liu, S. L. Jacques, M. Azimipour, J. D. Rogers, R. Pashaie, and K. W. Eliceiri, “Optogensim: a 3d monte carlo simulation platform for light delivery design in optogenetics,” *Biomed. Opt. Express* **6**, 4859–4870 (2015).
- [142] N. Grossman, V. Poher, M. S. Grubb, G. T. Kennedy, K. Nikolic, B. McGovern, R. B. Palmieri, Z. Gong, E. M. Drakakis, M. A. A. Neil, M. D. Dawson, J. Burrone, and P. Degenaar, “Multi-site optical excitation using chr2 and micro-led array,” *Journal of Neural Engineering* **7**, 016004 (2010).
- [143] I. Vanzetta, R. Hildesheim, and A. Grinvald, “Compartment-resolved imaging of activity-dependent dynamics of cortical blood volume and oximetry,” *Journal of Neuroscience* **25**, 2233–2244 (2005).
- [144] B. R. Chen, M. G. Kozberg, M. B. Bouchard, M. A. Shaik, and E. M. C. Hillman, “A critical role for the vascular endothelium in functional neurovascular coupling in the brain,” *Journal of the American Heart Association* **3** (2014).

- [145] T. A. Longden, F. Dabertrand, M. Koide, A. L. Gonzales, N. R. Tykocki, J. E. Brayden, D. Hill-Eubanks, and M. T. Nelson, “Capillary k⁺-sensing initiates retrograde hyperpolarization to increase local cerebral blood flow,” *Nat Neurosci* **advance online publication** (2017). Article.
- [146] D. Ho, X. Zhao, S. Gao, C. Hong, D. E. Vatner, and S. F. Vatner (John Wiley & Sons, Inc., 2011), chap. Heart Rate and Electrocardiography Monitoring in Mice.
- [147] S. M. Jaber, F. C. Hankenson, K. Heng, A. McKinstry-Wu, M. B. Kelz, and J. O. Marx, “Dose regimens, variability, and complications associated with using repeat-bolus dosing to extend a surgical plane of anesthesia in laboratory mice,” *Journal of the American Association for Laboratory Animal Science* **53** (2014).
- [148] A. J. Ewald, Z. Werb, and M. Egeblad, “Monitoring of vital signs for long-term survival of mice under anesthesia,” *Cold Spring Harb Protoc* **2011**, pdb.prot5563–pdb.prot5563 (2011). 21285263[pmid].
- [149] M. M. B. Cardoso, Y. B. Sirotin, B. Lima, E. Glushenkova, and A. Das, “The neuroimaging signal is a linear sum of neurally distinct stimulus- and task-related components,” *Nat Neurosci* **15**, 1298–1306 (2012).
- [150] M. Nemoto, S. Sheth, M. Guiou, N. Pouratian, J. W. Y. Chen, and A. W. Toga, “Functional signal- and paradigm-dependent linear relationships between synaptic activity and hemodynamic responses in rat somatosensory cortex,” *Journal of Neuroscience* **24**, 3850–3861 (2004).
- [151] B. R. Chen, M. B. Bouchard, A. F. McCaslin, S. A. Burgess, and E. M. Hillman, “High-speed vascular dynamics of the hemodynamic response,” *NeuroImage* **54**, 1021–1030 (2011).
- [152] L. Boorman, A. J. Kennerley, D. Johnston, M. Jones, Y. Zheng, P. Redgrave, and J. Berwick, “Negative blood oxygen level dependence in the rat: a model for investi-

- gating the role of suppression in neurovascular coupling,” *Journal of Neuroscience* **30**, 4285–4294 (2010).
- [153] A. J. Kennerley, S. Harris, M. Bruyns-Haylett, L. Boorman, Y. Zheng, M. Jones, and J. Berwick, “Early and late stimulus-evoked cortical hemodynamic responses provide insight into the neurogenic nature of neurovascular coupling,” *Journal of Cerebral Blood Flow & Metabolism* **32**, 468–480 (2012). PMID: 22126914.
- [154] N. Nishimura, C. B. Schaffer, B. Friedman, P. D. Lyden, and D. Kleinfeld, “Penetrating arterioles are a bottleneck in the perfusion of neocortex,” *Proceedings of the National Academy of Sciences* **104**, 365–370 (2007).
- [155] A. Y. Shih, P. Blinder, P. S. Tsai, B. Friedman, G. Stanley, P. D. Lyden, and D. Kleinfeld, “The smallest stroke: occlusion of one penetrating vessel leads to infarction and a cognitive deficit,” *Nat Neurosci* **16**, 55–63 (2013).
- [156] P. O’Herron, P. Y. Chhatbar, M. Levy, Z. Shen, A. E. Schramm, Z. Lu, and P. Kara, “Neural correlates of single-vessel haemodynamic responses in vivo,” *Nature* **534**, 378–382 (2016). Letter.
- [157] A. Devor, P. Tian, N. Nishimura, I. C. Teng, E. M. C. Hillman, S. N. Narayanan, I. Ulbert, D. A. Boas, D. Kleinfeld, and A. M. Dale, “Suppressed neuronal activity and concurrent arteriolar vasoconstriction may explain negative blood oxygenation level-dependent signal,” *Journal of Neuroscience* **27**, 4452–4459 (2007).
- [158] N. Harel, S.-P. Lee, T. Nagaoka, D.-S. Kim, and S.-G. Kim, “Origin of negative blood oxygenation level-dependent fmri signals,” *Journal of Cerebral Blood Flow & Metabolism* **22**, 908–917 (2002). PMID: 12172376.
- [159] J. P. Newman, M.-f. Fong, D. C. Millard, C. J. Whitmire, G. B. Stanley, and S. M. Potter, “Optogenetic feedback control of neural activity,” *Elife* **4**, e07192 (2015).

- [160] L. Grosenick, J. H. Marshel, and K. Deisseroth, “Closed-loop and activity-guided optogenetic control,” *Neuron* **86**, 106 – 139 (2015).

Curriculum Vitae

Education

- University of Wisconsin-Milwaukee**, Milwaukee, WI,
Doctor of Philosophy, Electrical Engineering Summer 2017
- University of Minnesota**, Minneapolis, MN,
Doctor of Philosophy, Electrical Engineering September 2011-Jun 2012 (transferred)
(Transferred to University of Wisconsin-Milwaukee)
- University of Tehran**, Tehran, Iran,
Master of Science, Electrical Engineering Summer 2005
- Amirkabir university of technology**, Tehran, Iran,
Bachelor of Science, Biomedical Engineering Summer 2002

Research Assistant

- University of Wisconsin-Milwaukee, ECE Department Fall 2012 - Fall 2016

Industrial Experience

- Researcher** Summer 2008 - Fall 2011
Scientific Green Company, Tehran, Iran.
- Researcher** Spring 2007 - Spring 2008
Research Center of Intelligent Signal Processing, Tehran, Iran.
- Researcher** Fall 2005 - Fall 2006

Sepanta Robotic Research & Artificial Intelligence Foundation, Tehran, Iran.

Instrumentation Engineer

Fall 2003 - Summer 2004

Iran Telecommunication Research Center, Tehran, Iran.

Teaching Experience

Introduction to Electrical Engineering

Spring 2015

Electrical Engineering, University of Wisconsin-Milwaukee

Internship

Instrumentation Engineer

Summer 2001

Iranian Research Organization for Science and Technology (IROST), Tehran, Iran.

Achievements

- Distinguished Dissertation Fellowship (DDF) award, university of Wisconsin-Milwaukee, 2016-2017.
- Chancellor's Graduate Student Award, university of Wisconsin-Milwaukee, Spring 2015.
- Chancellor's Graduate Student Award, university of Wisconsin-Milwaukee, Spring 2013.
- Chancellor's Graduate Student Award, university of Wisconsin-Milwaukee, Fall 2012.
- Bronze medalist at the National Physics Olympiad.

Journal Publications

- Park, D.W., Brodnick, S.K., Ness, J.P., **Atry, F.**, Krugner-Higby, L., Sandberg, A., Mikael, S., Richner, T.J., Novello, J., Kim, H. and Baek, D.H., 2016. Fabrication and utility of a transparent graphene neural electrode array for electrophysiology, in vivo imaging, and optogenetics. *Nature Protocols*, 11(11), pp.2201-2222.
- Azimipour, M., **Atry, F.** and Pashaie, R., 2016. Calibration of digital optical phase conjugation setups based on orthonormal rectangular polynomials. *Applied optics*, 55(11), pp.2873-2880.
- **Atry, F.** and Pashaie, R., 2016. Analysis of intermediary scan-lens and tube-lens mechanisms for optical coherence tomography. *Applied optics*, 55(4), pp.646-653.
- **Atry, F.**, Frye, S., Richner, T.J., Brodnick, S.K., Soehartono, A., Williams, J. and Pashaie, R., 2015. Monitoring cerebral hemodynamics following optogenetic stimulation via optical coherence tomography. *IEEE Transactions on Biomedical Engineering*, 62(2), pp.766-773.
- Azimipour, M., **Atry, F.** and Pashaie, R., 2015. Effect of blood vessels on light distribution in optogenetic stimulation of cortex. *Optics letters*, 40(10), pp.2173-2176.
- Park, D.W., Schendel, A.A., Mikael, S., Brodnick, S.K., Richner, T.J., Ness, J.P., Hayat, M.R., **Atry, F.**, Frye, S.T., Pashaie, R. and Thongpang, S., 2014. Graphene-based carbon-layered electrode array technology for neural imaging and optogenetic applications. *Nature communications*, 5.
- Schendel, A.A., Nonte, M.W., Vokoun, C., Richner, T.J., Brodnick, S.K., **Atry, F.**, Frye, S., Bostrom, P., Pashaie, R., Thongpang, S. and Eliceiri, K.W., 2014. The effect of micro-ECoG substrate footprint on the meningeal tissue response. *Journal of neural engineering*, 11(4), p.046011.
- Andalib, A. and **Atry, F.**, 2009. Multi-step ahead forecasts for electricity prices

using NARX: A new approach, a critical analysis of one-step ahead forecasts. Energy Conversion and Management, 50(3), pp.739-747.

Conference Publications

- M Azimipour, **F Atry**, R Pashaie, "Light pattern preservation in rodent's cortical tissue during optogenetic neuro-stimulation" SPIE BiOS, 970610-970610-1, 2016.
- **Atry, Farid**, Amir H. Omidvarnia, and S. Kamaledin Setarehdan. "Model Based EEG signal purification to improve the accuracy of the BCI systems." In Proceedings of the 13th European Signal Processing Conference EUSIPCO, 2005.
- **Atry, Farid**, A. H. Omidvarnia, and S. K. Setarehdan, Comparison of the ability of the Box-Jenkins family in EEG signal purification, 12th Iranian Conference on Biomedical Engineering, Sahand University of Technology, Tabriz, Iran, Nov. 16-18, 2005 (IN PERSIAN).
- Omidvarnia, Amir H., **Farid Atry**, S. Kamaledin Setarehdan, and Babak N. Arabi. "Kalman filter parameters as a new EEG feature vector for BCI applications." In Proceedings of the 13th European Signal Processing Conference EUSIPCO. 2005.
- Omidvarnia A. H., **Farid Atry**, and S. K. Setarehdan, B. N. Araabi, "Kalman Filter as a tool to reduce EEG channels in BCI application," 13th Iranian Conference on Electrical Engineering (ICEE 2005), Zanjan, Iran, May 10-13, 2005 (IN PERSIAN).
- Omidvarnia, A. H. , **Farid Atry**, and S. K. Setarehdan, B. N. Araabi, Classification of special mental tasks using Fractal features of EEG signals in frequency domain, 6th conference on Intelligent systems (CIS2004), Kerman, Iran, Nov. 25-26, 2004 (IN PERSIAN).
- Andalib, Arash , Mehdi Zare, and **Farid Atry**, A fuzzy expert system for earthquake

prediction, case study: The Zagros range, The Third International Conference on Modeling, Simulation, and Applied Optimization, 2009.

Poster Presentations

- **Farid Atry** and Ramin Pashaie, "Design of a scan-lens and tube-lens for OCT applications," Accepted for presentation at SPIE Photonic West Feb. 2016.
- **Farid Atry**, Seth Frye, Alana M Soehartono, Thomas J Richner, Sarah K Brodnick, Justin Williams, and Ramin Pashaie, "Optical Coherence Tomography: evaluation of vasodynamics induced by optical neurostimulation in rodent cerebral cortex," Neurotech 2015.
- Seth Frye, Alana Soehartono, **Farid Atry**, Amy L. Kaczmarowski, Ramin Pashaie, "Monitoring of hemodynamic signals post optogenetic stimulation via optical coherence tomography," SPIE Photonic West Feb. 2014.
- Seth Frye, Alana M. Soehartono, **Farid Atry**, Ramin Pashaie, "Real-Time Multimodal-Microvasculature Imaging by Spectral Domain Optical Coherence Tomography" 35th Great Lakes Biomedical Conference, GE Healthcare Institute, Waukesha, Wisconsin, April, 2013.